

secondary minerals: chalcocite

Galena and tetrahedrite are paragenetic and replace pyrite. Chalcopyrite exists on the boundary of galena and tetrahedrite. A part of galena, tetrahedrite, and pyrite are replaced with chalcocite.

### 2-3-5 Chemical Analysis of the Host Rock

The host rocks of the Rocha mine consist of carbonate rocks of limestone and dolomite. It is difficult to divide these rocks with the naked eye, but by using a 10% HCl solution it be able to divided the limestone and dolomite into four rock types based on the amount of effervesence products. It also has been carried out tests on the rock constituent minerals, using X-ray diffraction analysis (Table A-4) and analysis of lithochemical components (Ca O, Si O<sub>2</sub>, Al<sub>2</sub> O<sub>3</sub>, Fe<sub>2</sub> O<sub>3</sub>, Mg O) Table (A-6), on 32 samples obtained from these rock types. For a part of these samples, it has been carried out measurement of the base metal content (Au, Ag, Cr, Pb, Zn) in the host rock by atomic absorption analysis (Table I-4).

The results of X-ray diffraction show that calcite, dolomite, quartz, and sericite were present in the sample. Small amounts of plagioclase and very small amounts of chlorite were also found in some samples. The classification of the limestone and dolomite rock types was made according to the amounts of calcite and dolomite. Thus, the amount of the main constituent minerals were calculated theoretically\* based on the results of those analyses. A comparison with the rock facies and the hydrochloric acid test are shown as following:

①	limestone	dolomite/(calcite + dolomite)	less than 15%
②	dolomitic limestone	" " " "	15 - 50%
③	calcareous dolomite	" " " "	50 - 85%
④	dolomite (dolostone)	" " " "	more than 85%

The quartz content ranges from 2 to 32%, showing a large variation in both limestone and dolomite. In the past, it is seemed to be a large amount of quartz in the dolomite, but here the difference of the amount of quartz can not be seen in the each rock type.

Fig. I-19 shows the results of measurement of the base metal content of the host rock

---

\* 1) Calculation of dolomite (Mg CO<sub>3</sub>) and calcite (CaCO<sub>3</sub>),  
2) Calculation sericite [2K<sub>2</sub>O·6SiO<sub>2</sub>·2Al<sub>2</sub>O<sub>3</sub>·(OH)<sub>4</sub>] as a representative of Al<sub>2</sub>O<sub>3</sub>.  
3) Quartz is SiO<sub>2</sub>, which is remains after sericite calculation.



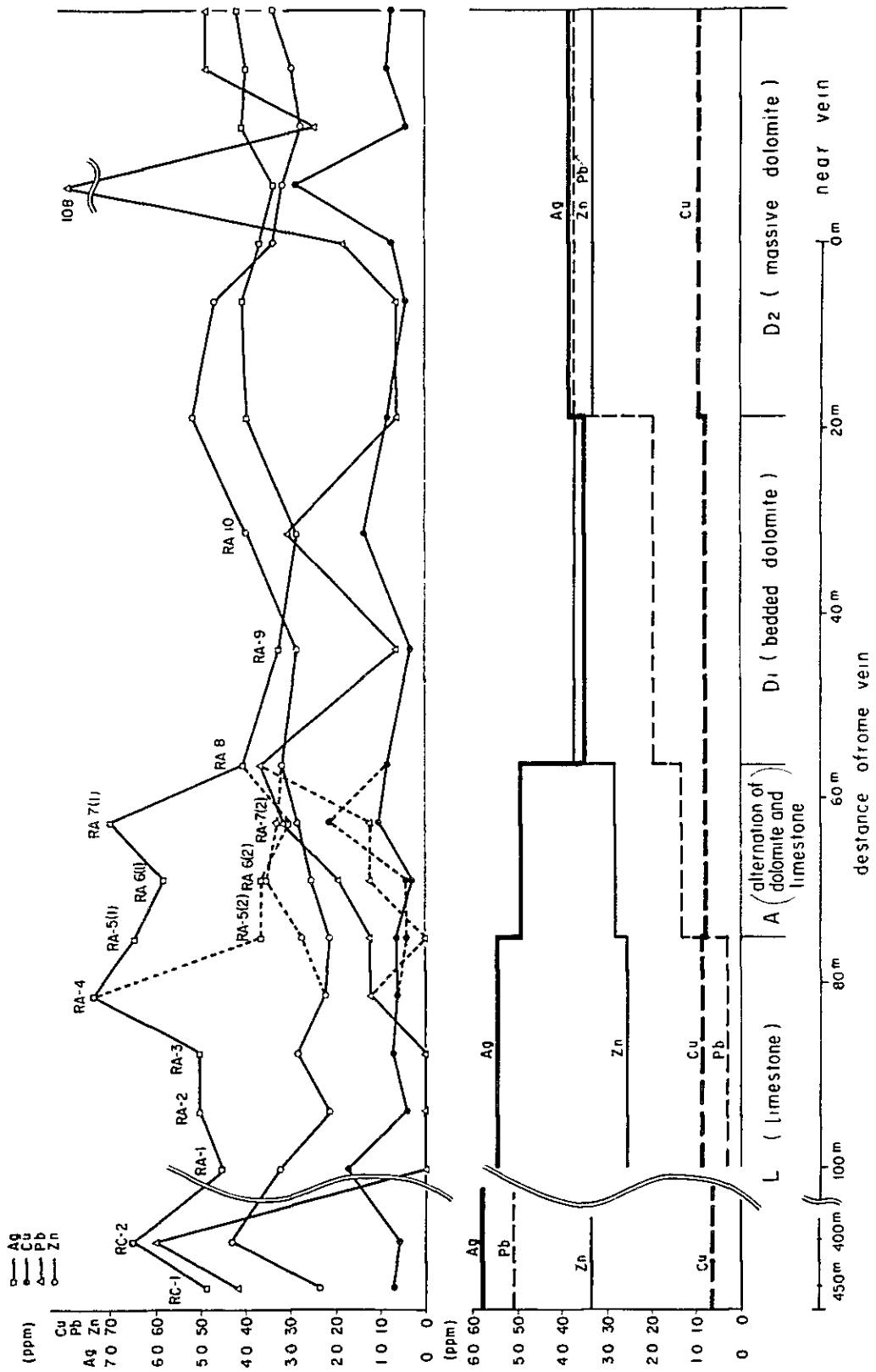


Fig. I - 19 Variation Diagram of Base Metal Content in Carbonate Rocks



Table I-3 Calculated Constituent Minerals of Carbonate Rocks

Sample No	w% dolomite	w% calcite	w% quartz	w% sericite	w% other	dal +cal	rank of Hcl test	rock facies
RA-1	44	29	14	12	1	60	③	L
2	26	46	21	3	4	35	②	L
3	26	44	22	5	5	37	②	L
4	6	89	2	0	3	6	①	L
5(1)	7	77	8	2	6	11	①	A
5(2)	46	16	23	5	10	74	③	A
6(1)	7	71	16	3	3	9	①	A
6(2)	66	4	11	6	13	94	④	A
7(1)	7	81	6	1	5	8	①	A
7(2)	59	2	23	6	10	97	④	A
8	72	4	12	6	6	95	④	D <sub>1</sub>
10	61	1	22	11	5	98	④	D <sub>1</sub>
12	50	2	32	6	10	96	④	D <sub>1</sub>
14	76	1	4	8	11	99	④	D <sub>1</sub>
16	81	0	4	8	7	100	④	D <sub>2</sub>
17	65	5	10	13	7	93	④	D <sub>2</sub>
18	65	2	13	13	7	97	④	D <sub>2</sub>
19	72	4	18	2	4	95	④	D <sub>2</sub>
20	65	2	20	9	4	97	④	D <sub>2</sub>
21	74	6	16	1	3	92	④	D <sub>2</sub>
RB-1	42	37	10	7	4	53	②	A
2	7	87	2	1	3	8	①	L
3	61	0	25	9	5	100	④	A <sub>1</sub>
4	59	0	23	16	2	100	④	D <sub>1</sub>
5	91	0	4	1	4	100	④	D <sub>1</sub>
6	81	4	7	4	8	95	④	D <sub>1</sub>
7	65	25	8	1	1	72	③	A <sub>1</sub>
8	72	2	19	4	3	97	④	D <sub>2</sub>
9	52	8	22	12	6	87	③	D <sub>2</sub>
10	74	0	14	9	3	100	④	D <sub>2</sub>
RC-1	13	74	2	13	-	15	①	L
2	39	35	16	4	6	53	②	L

- ① limestone
- ② dolomitic limestone
- ③ calcic limestone
- ④ dolomite

- D<sub>2</sub> massive dolomite facies
- D<sub>1</sub> bedded dolomite facies
- A alternation of limestone & dolomite facies
- L limestone facies

Table I-4 Base Metal Content in Carbonate Rocks

(a) in Rocha Mine

Sample No.	AuPpm	Agppm	CuPpm	PbPpm	Znppm	
RA-1	0.0	4.5	17	0	32	o limestone o 80m from vein
2	0.0	4.9	4	0	21	o limestone o 75m from vein
3	0.0	4.8	7	0	28	o limestone o 70m from vein
4	0.0	7.3	6	12	22	o limestone o 65m from vein
5(1)	0.0	6.4	6	12	21	o limestone o 60m from vein
5(2)	0.0	3.6	4	0	27	o dolomite o 60m from vein
6(1)	0.0	5.8	3	19	25	o limestone o 55m from vein
6(2)	0.0	3.6	4	12	35	o dolomite o 55m from vein
7(1)	0.0	6.9	10	31	28	o limestone o 50m from vein
7(2)	0.0	3.0	21	12	32	o dolomite o 50m from vein
8	0.0	4.0	8	36	31	o dolomite o 45m from vein
10	0.0	3.2	3	6	28	o dolomite o 35m from vein
12	0.0	2.8	13	30	39	o dolomite o 25m from vein
14	0.0	3.9	8	6	51	o dolomite o 75m from vein
16	0.0	4.0	4	6	46	o dolomite o 5m from vein
17	0.0	3.6	7	18	33	o dolomite near vein
18	0.0	3.3	28	108	31	o dolomite near vein
19	0.0	4.0	4	24	27	o dolomite near vein
20	0.0	3.9	8	48	29	o dolomite near vein
21	0.0	4.1	7	48	33	o dolomite near vein
RC-1	0.0	6.5	7	42	24	o limestone
2	0.0	4.9	6	60	43	o limestone
mean	0.0	4.5	84	23.8	29.9	

(b) in Survey Area

	Sample No.	Ag (ppm)	Cu (ppm)	Pb (ppm)	Zn (ppm)	Location	
Açungui Formation I	AIs	A083	0.1	12	22	79	Perau
		A089	0.1	10	7	9	Perau
		D089	0.2	7	22	29	Agua Clare
Açungui Formation I	AIs	B080	0.6	42	41	27	Olho D'agua
		D081	0.5	10	30	21	do
		B096	0.4	8	22	11	do
		B070	0.0	34	19	59	Serra do Vinte e sete
		B091	0.6	17	7	48	Olho D'agua
Açungui Formation III	AIII L <sub>1</sub>	B038	0.2	13	19	59	Carumbé
		A036	0.6	8	59	40	Mato Preto
	AIII L <sub>2</sub>	A006	0.3	77	33	26	panelas
		A005	0.6	88	37	12	panelas
	AIII S <sub>2</sub> & AIII L <sub>2</sub>	B010	0.5	13	37	19	Rio Ribeira
		B014	0.4	3	30	29	Rio Ribeira
	AIII L <sub>3</sub>	A015	0.6	19	37	16	Rio Ribeira
	B025	0.7	17	44	8	Rio Ribeira	
	0001	0.2	34	20	86	Ribeira	

(c) general

element	Au (ppm)	Ag (ppm)	Cu (ppm)	Pb (ppm)	Zn (ppm)
GRAF (1960)	0.005 ~0.009	0.7 ±0.4	14±9	8±4	26±5
TUREKIAN & WEDEPOHL (1961)	0.00X	0.0X	4	9	20



in the Nova Esperanza cross cut of the Rocha mine.

- (a) In the part of limestone and dolomite alternation (A), there is a tendency of that silver content high in limestone, and lead content high in dolomite.
- (b) The silver content is much higher in limestone, and decreasing into the into the dolomite ( $D_1$ ,  $D_2$ ). The lead content show the opposit characteristic to the silver and zinc is the same way as lead. The copper content does not seem to change at all though. As result of comparison the base meta content of the host rock of the Rocha ore deposits with the carbonate rock of other horizons (A1cs, A1Ics, AIII L, AIII  $L_2$ , AIII  $S_2$  ls, AIII  $L_3$ ), and with the general carbonate rock according to Graf (1960), Turekin and Wedepohl (1961), the contents of Cu, Pb, Zn are about average in the host rock but an extremely high silver content can be seen. Though a reason for the relation of mineralization of the ore deposits is unclear, for it can be thought of as a major characteristic that indicate the host rock for prospecting.

#### 2-3-6 Scope of Future Exploration

The vein fissure pattern of the Rocha ore deposit was formed at the end of a folding movement in the Rocha area. It has a tendency that is indicating a regular trend and developing in the dolomite and is formed in a dynamically competent situation.

Up to present, most of the veins were prospected in the Rocha mines in the dolomite horizons.

According to the results of the present survey, the scope of future prospecting are as follows:

- (1) The cross cut of the western section of the Bassetti neighborhood at the 403 meter level was went toward the bassitti fault vein. It is seperating from the massive dolomite ( $D_2$ ) and aproaching to the limestone (L). The prospect towards the center of  $D_2$  (the mine coordinates in neighborhood of 1900-400) can be expected in future.
- (2) At the 308 meter level, prospect towards the unprospected area in the center of  $D_2$  area (coordinates 1800-300) can be expected.
- (3) At the 227 meter level, the prospect for the lower section of present known Egara vein group and the Bassetti vein group is expected.





### CHAPTER 3 MEASUREMENT OF LEAD ISOTOPES

The lead ore deposits of the survey area are divided into the Perau type, strata bound ore deposit in calc-silicate rock of the Açungui formation I, and the Rocha type, vein type ore deposit in the limestone of Açungui formation III.

Many theories have been proposed in the past concerning the origin of these ore deposits. Though there is still no widespread concensus, in recent years it has been thought that the Perau type ore deposit had formed at the same time as the Açungui formation I had formed. Also, it is thought that the Rocha ore deposit was formed as concentration of base metals from the Açungui formation III into the fissures by the tectonic movement in the end of Pre-Cambrian.

In the present study, the lead isotopes of galena taken from the Perau mines and the Rocha mines were measured two samples each.

The results of plotting the measurements of lead isotope value of the each mines and data of E, C, Damasceno (1966) on an ore lead growth curve of Cumming and Richards (1976) is shown in Fig. I-20. The groups which clearly differentiated the measured values of the Perau mine and the Rocha mine are formed, and indicating that the former is plotted in the neighborhood of 1400 m.y., while the latter is plotted in the neighborhood of 1200 m.y.. According to Pb/Sr geochronology is known as good agreement with the age of the Perau ore deposits (CPRM, 1981; F. Batolla, Jr., 1977)

Regarding the 12,000 m.y. age of the Rocha type, it is thought that it stratigraphically approximates the age of the Açungui formation III. Consequently, the obtained age of these lead isotopes is older than the age of granite in this area (550 m.y.), as stated by Melcher (1968), and the argument that the mineralization of the lead ore deposit is related to the intrusion of granite is denied. Conversely, the fact that the age of host rock show good agreement with the Perau ore deposits, suggest that the Perau ore deposits sedimented syngenetically in the host rock in the same time. Also, the fact that age of the Rocha mine and other mine show older than the period of granite, suggest that ore deposits were formed as that base metals had accumulated in the host rock were remobilized and concentrated in the fissures of the host rock.



Table I-5 Result of Pb Isotopic Analysis

Sample No.	Locationl	Isotopical Relation		Isotopic Age (m.y)
		Pb207/Pb204	Pb206/Pb204	Cumming and Richards (1975)
P - 1	Perau Mine	15.51	16.24	1,400
P - 2	do	15.56	16.31	1,430
R - 1	Rocha Mine	15.54	16.91	1,070
R - 2	do	15.51	16.84	1,120
1 *	Rocha Mine	15.65	17.01	1,050
2 *	Rocha Mine	15.59	16.92	1,070
3 *	Paquero Mine	15.51	16.82	1,130
4 *	do	15.59	16.90	1,080
5 *	do	15.59	16.78	1,150
6 *	do	15.65	16.83	1,120
7 *	Panelas Mine	15.54	16.66	1,210

\* after Damasceno E.C (1966)

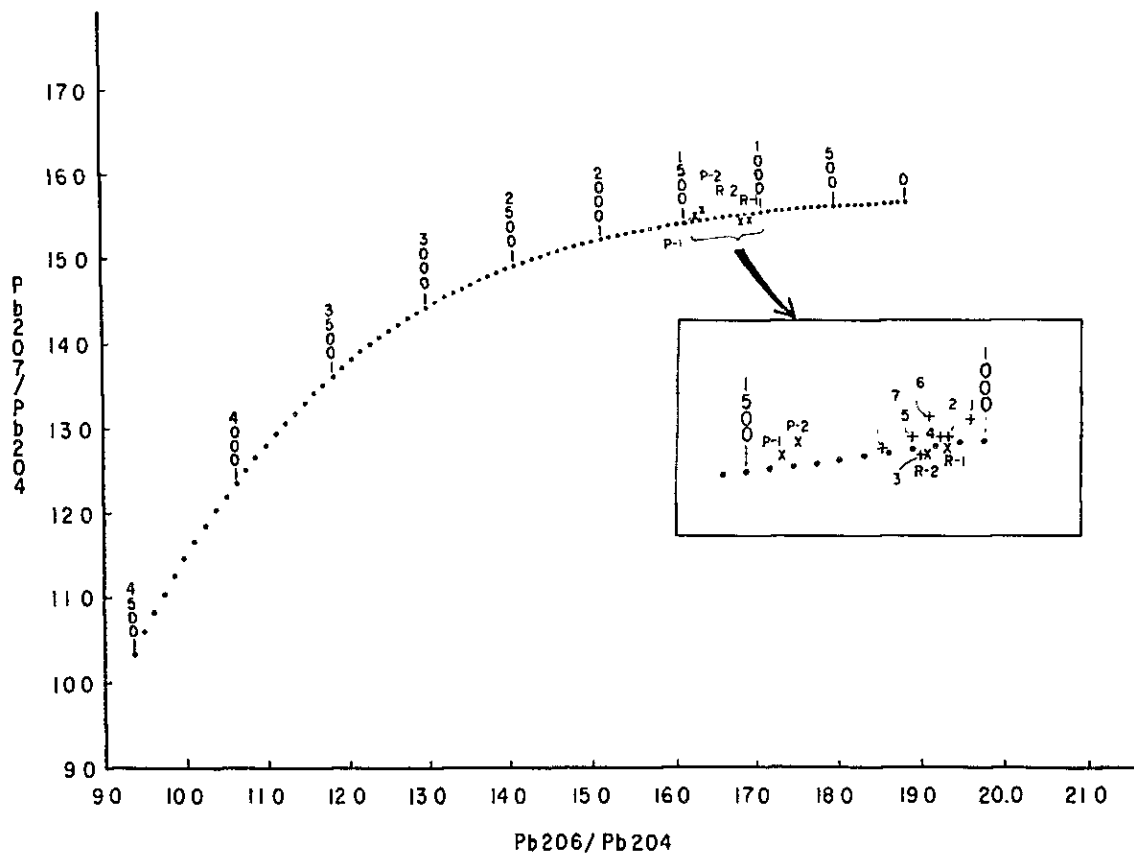


Fig. I - 20 Pb Isotopic Ages by Ore Lead Growth Curve of Cumming and Richards



## CHAPTER 4. GEOCHEMICAL SURVEY

In order to clarify the mineralization in the Perau horizon, a geochemical soil survey covering the Perau horizon was carried out.

### 4-1 Methodology and Component Analysis

The samples were collected along the IP survey lines with a 50 meter interval (100 meters in some samples), covering the Perau Horizon. There were 113 samples obtained, and as a rule, from the B horizon using a hand auger. The basic data included the analysis of six components such as Cu, Pb, Zn, Ni, Co, and Mn. These were analyzed by atomic absorption methods.

### 4-2 Analytic Procedures

Histograms of unitary components and anomaly zone distribution maps were compiled, and further, in order to extract the components which closely relating to the mineralization, the factor analysis and mapping of the factor map have been done (Table A-7).

#### 4-2-1 Analysis of Unitary Components

From all of the analytic variables a histogram of each of the components was compiled (Fig. I-21), and the mean values ( $10^{\bar{x}}$ ) and the standard deviation ( $\sigma$ ) were calculated (Table I-6).

The each Cu, Pb, Zn histograms are clearly divided into two groups of population. The lower value of population than  $10^{\bar{x}+2\sigma}$  are interpreted as reflecting the host rock, and the higher value of population than  $10^{\bar{x}+2\sigma}$  are interpreted as reflecting the mineralization. The value of the population, which is thought to be related to mineralization, is higher than  $10^{\bar{x}+2\sigma}$ .

The Ni, Co, Mn histogram does not show a normal distribution, and some population can be thought of as overlapping one another. By this histogram alone, it is difficult to discriminate whether it is related to mineralization or related to the components of the host rock. According to the factor analysis, however, factor 1 (Ni - Co - Mn - Zn) is interpreted as reflecting amphibolite and the host rock of ore deposit.

It is illustrated that the values over the  $10^{\bar{x}+2}$  as a high anomaly zone, and over  $10^{\bar{x}+\sigma}$  as a low anomaly zone. The Cu anomaly zone is distributed along the Perau horizon towards the south from the G-line of the neighboring known ore deposits area. The Pb is distributed in the center of the G-line to the E-H line, and Zn is distributed discontinuously

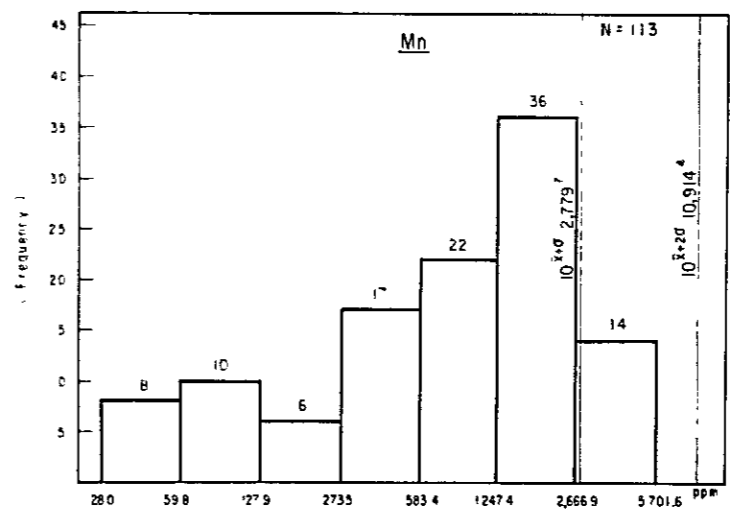
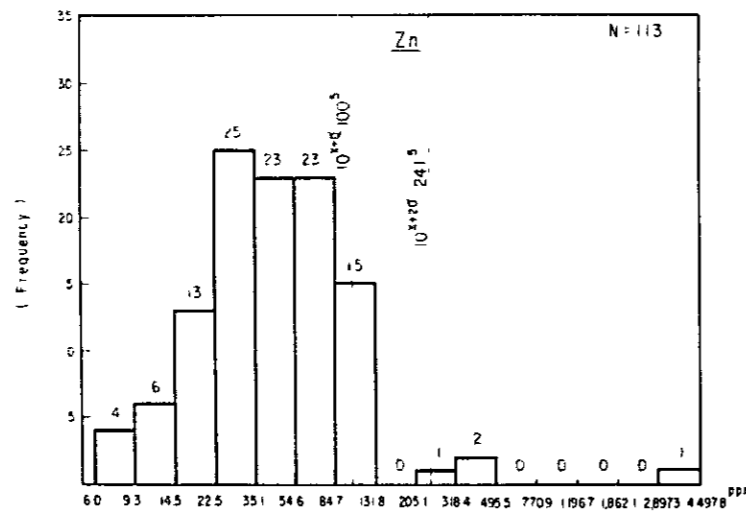
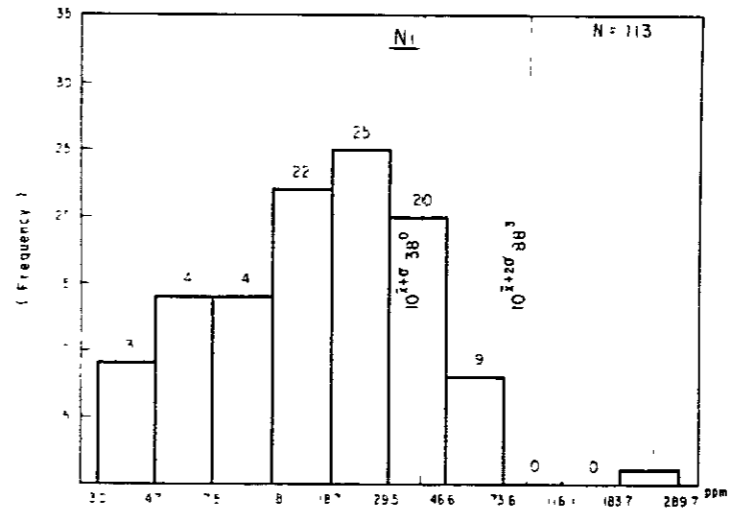
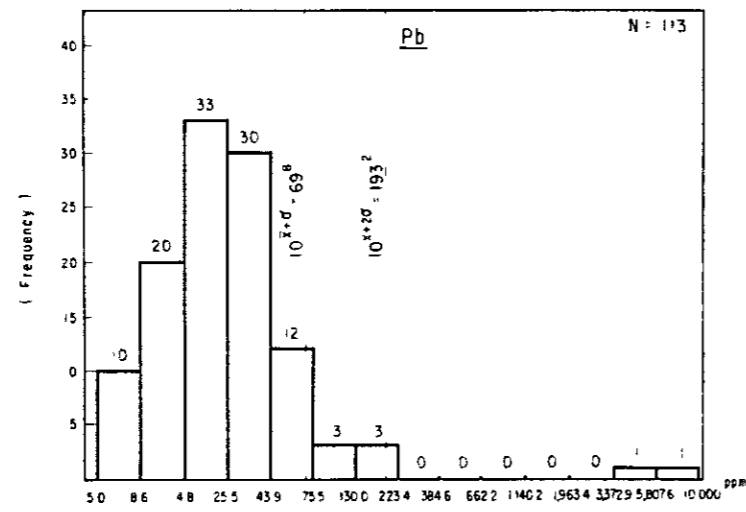
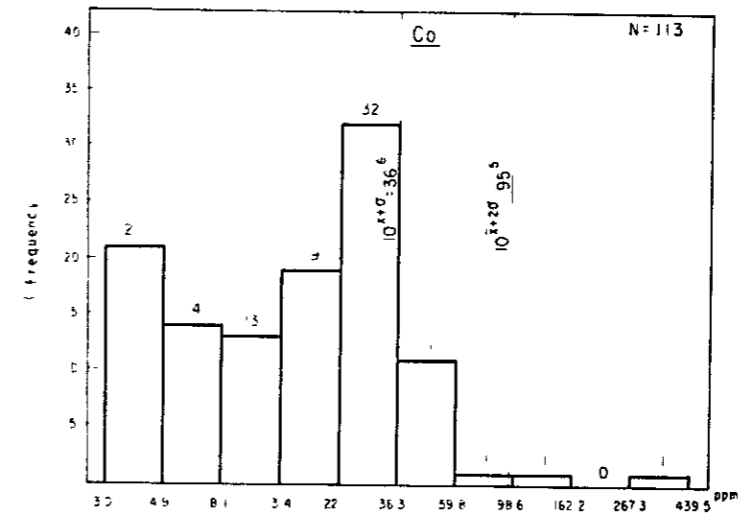
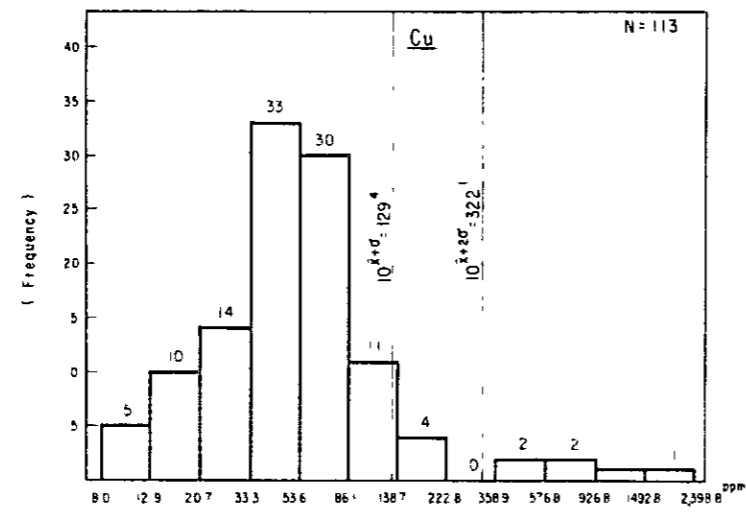


Fig. I-21 Histogram for Cu, Pb, Zn, Co, Ni, and Mn, in geochemical Data in Perau Area





**Table I-6 Mean and Standard Deviation of  
Geochemical Data in Perau Area**

Element	Max (ppm)	Min (ppm)	Mean 10x	SD 10 $\sigma$	10 $x+\sigma$	10 $x+2\sigma$
Cu	2400	8	52.12	2.48	129.4	322.1
Pb	10000	5	25.18	2.77	69.8	193.2
Zn	4500	6	41.88	2.40	100.5	241.5
Co	440	3	14.09	2.60	36.6	95.5
Ni	290	3	16.39	1.03	38.0	88.3
Mn	5700	28	707.95	3.93	2779.7	10914.4

**Table I-7 Factor Loading of Geochemical Data  
in Perau Area**

	Factor 1	Factor 2
Element	Factor Loading	Factor Loading
Cu	0.28992	0.70405
Pb	-0.01332	0.92004
Zn	0.69207	0.54181
Co	0.91388	0.20020
Ni	0.85397	0.24562
Mn	0.90075	-0.02068



in the same area of Pb.

Ni and Co are distributed close to the center of the G-line, while Mn is distributed along the Perau horizon south of the H-line.

#### 4-2-2 Factor Analysis

As an analytical method which is in order to explaining the characteristics of variable quantities, shown by multivariate data, and to finding out a scientific simplicity by hypothetical variation and small representative variation, the factor analysis is the best method.

By using a computer, by the Barimach method, multivariate data of six components of the 113 samples were calculated, and the results of this factor analysis, two factors were extracted.

The factors are characterized as having a factor variation of more than 0.5.

Factor 1 is characterized by Mn-Co-Ni-Zn, and factor 2 is characterized by Cu-Pb-Zn. As shown in Table I-7, the obtained scores of factors 1 and 2 of each samples were used in compiling a factor map (PL. I-12).

On the factor map, a high score zone of the factor 1 (Mn-Co-Ni-Zn) is distributed along the amphibolite (Alam) and the Perau horizon (AIIIs). The factor 2 (Cu-Pb-Zn), the high score zone is distributed coincide with the Perau horizon (AIIIs) from the E-line to the L-line. As for the Perau ore deposit is situated in the center of the high score zone of the factor 2.

The relationship between the mineralization and the factor 2 can be thought of as the mineralizations of Cu, Pb and Zn having been brought about by the same way.

Consequently, in future exploration of the Perau horizon, the high score area of Cu-Pb-Zn factor can be regarded as promissable.



## PART II      GEOPHYSICAL SURVEY



## CHAPTER 1 OUTLINE OF GEOPHYSICAL SURVEY

In phase II, four kinds of geophysical methods, gravity, IP Electrical, Spectral IP Electrical surveys and aeromagnetic interpretation, were carried out in the Anta Gorda area, Brasil.

Gravity survey was conducted to clarify the geological structure in the vicinity of Perau mine with a cooperation of São Paulo University. An area of the gravity survey area is 100 km<sup>2</sup> and total number of gravity points is 274.

IP electrical survey was carried out to delineate the ore horizon of Perau mine, setting 12 survey lines with total line length of 30.2 km.

And spectral IP method was conducted on two IP survey lines (Lines G and K, line length 5 km), where interesting results were observed on conventional IP method, with a cooperation of two geophysicists of Metal Mining Agency of Japan (MMAJ). The objective of this method is to collect the basic data of Perau ore horizon and clarify the distribution of Perau ore horizon.

Aeromagnetic interpretation work was performed to delineate the underground structure of the northeastern area (B-area, 3,250 km<sup>2</sup>) of the survey area, continuing to Phase I.





## CHAPTER 2 GRAVITY SURVEY

Gravity survey was conducted to clarify the underground structure in the survey area of 100 Km<sup>2</sup> in the vicinity of Perau mine.

### 2-1 Method of Survey

#### 2-1-1 Survey Planning

Observation stations are shown on Plates II-1 and II-2. Planned stations are 260 points and actual observation stations are 274 points. All these stations were measured by leveling.

The number of the stations are 102 to 380 (with lacked numbers of 161,162,251,299 and 363). The survey area is about 100 Km<sup>2</sup>, and the standard station interval is 400 m.

The observation stations were set along main roads and trails because of rough topography in the area. Therefore, the stations could not be located with uniform density. Each location of the points was decided by 1:10,000 (partly 1:25,000) maps.

#### 2-1-2 Gravimeter

Two La Coste and Romberg G type Gravimeters of Sao Paulo University and Paraná University, Brazil, were used. Specifications are listed below.

	São Paulo University	Paraná University
No. of Production	G-454	G-372
Operating Range (mgal)	0.0 – 7372.41	0.0 – 7476.48

La Coste Gravimeter is characterized by their worldwide range without the need of resetting, and the negligible drift is normally less than 0.5 mgal/month. Gravity values measured by this instrument ranges from 3,000 mgal to 4,000 mgal, whenever the station. In the low latitude countries like Brazil, however, gravity values varies from 2,300 mgal to 2,700 mgal.

Each La Coste gravimeter has its own particular correction parameter. The range of correction values is variable with the elevation and latitude of the survey area. In this case, the value shown on Table II-2-1 was adopted.

#### 2-1-3 Comparison of Standard Gravity

A gravity standard station, No. 40138B, located at Itapetininga 160 Km northeast of Adrianópolis, has been established by São Paulo University in 1978, using the IGSN

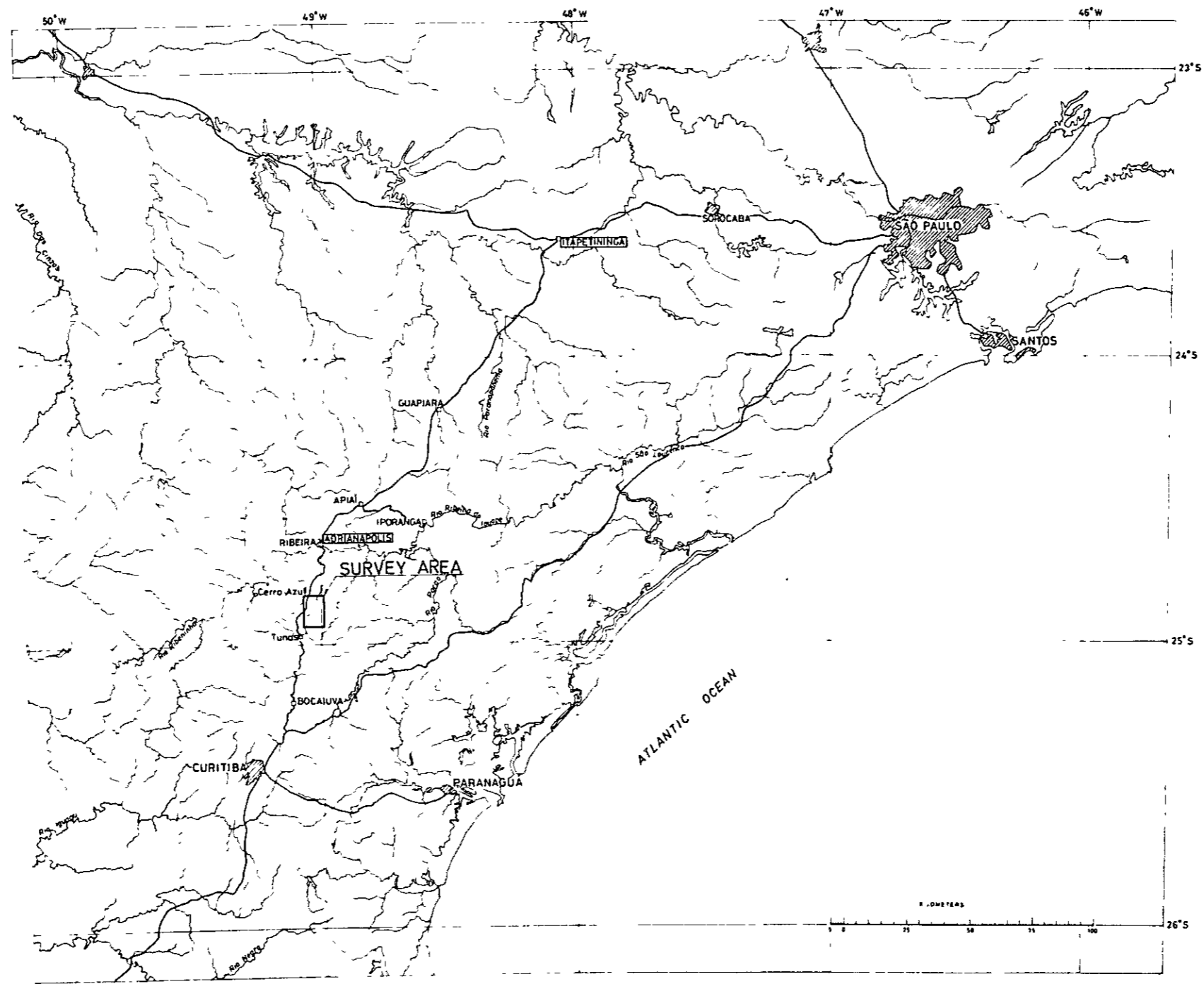


Fig. II-2-1 Location of Gravity Survey Area



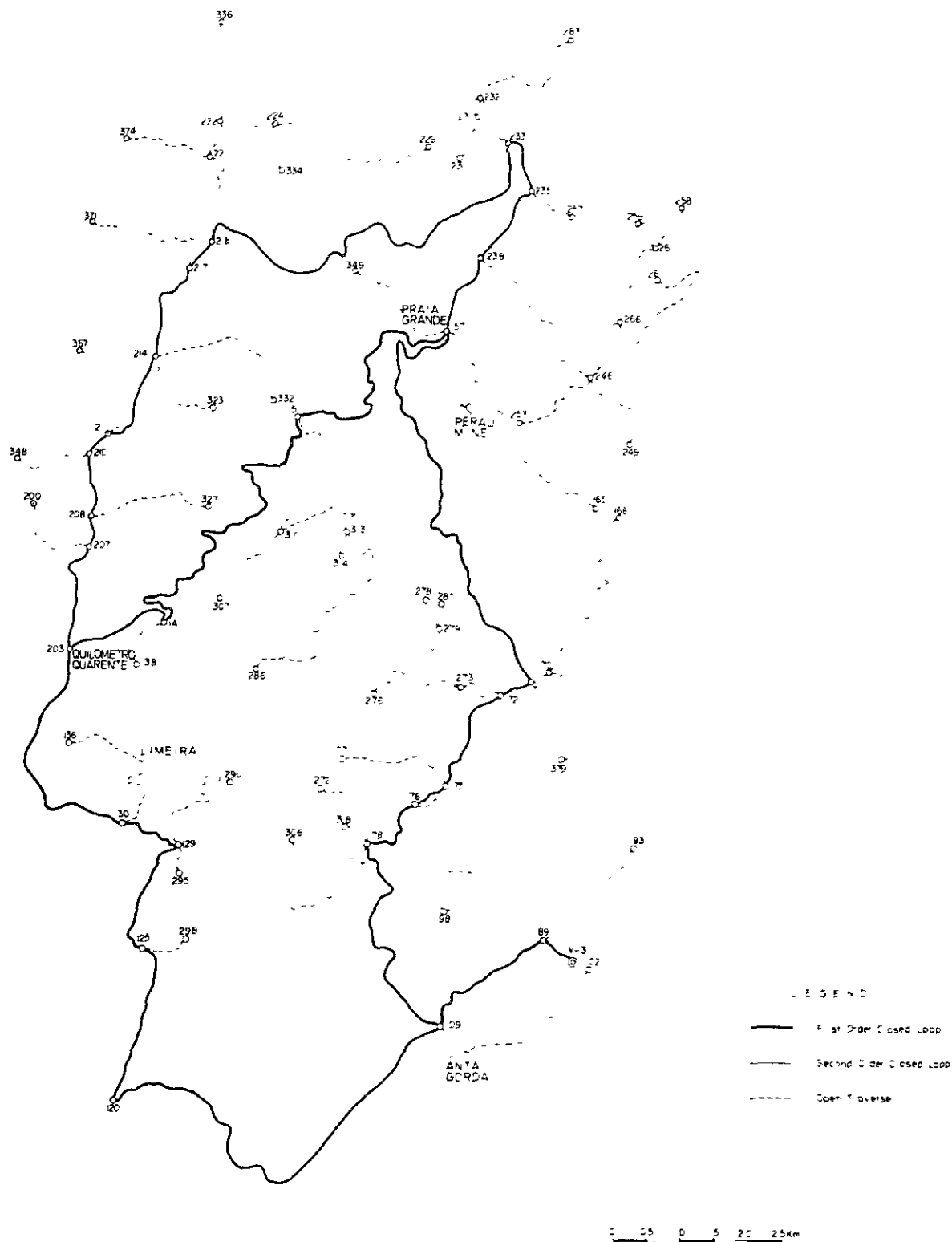


Fig. II-2-2 Route Map of Levelling Survey



(International Gravity Standardized Net) station 40136J (978,627.29 mgal) in São Paulo City. Information of No.40138B was used as a gravity base point, and gravity standard set at Adrianópolis 9000 is calculated. The results are shown on Table II-2-2. The value of 978,831.44 mgal was employed. used as a gravity base point, and gravity standard set at Adrianopolis 9000 is calculated. The results are shown on Table II-2-2. The value of 978,831.44 mgal was employed.

#### 2-1-4 Leveling

The direct leveling method was adopted for all points by Auto level B-2 of Sokkisha, Japan.

Basement of leveling is a triangular point, V-3 (1,108.03 m) established by CPRM (Companhia de Pesquisa de Recursos Minerais).

As indicated in Fig. II-2-2, the survey was taken by closed routes insofar as possible to increase accuracy.

### 2-2 Data Processing and Method of Analysis

#### 2-2-1 Gravity Correction

Several corrections should be made on the observed gravity value to determine the real Bouguer anomaly.

##### (1) Flow of Correction

The process of calculating the gravity value is shown on Fig. II-2-3.

##### a. Conversion

To obtain gravity in milligals from the reading of the counter and dial, a table of conversion is employed. In the table, the value of gravity in milligals is given for each 100 units of the counter. By using this table, and corresponding factor, the value of the gravity for any reading indicated by the counter may be obtained.

$$V_{rk} = K + k (V_r - V_{ro})$$

$V_{rk}$  : Observed gravity value

$V_r$  : Reading indicated by the counter

$V_{ro}$  : Reading for each 100 units of the counter

$K$  : Gravimeter constant

$k$  : Conversion factor



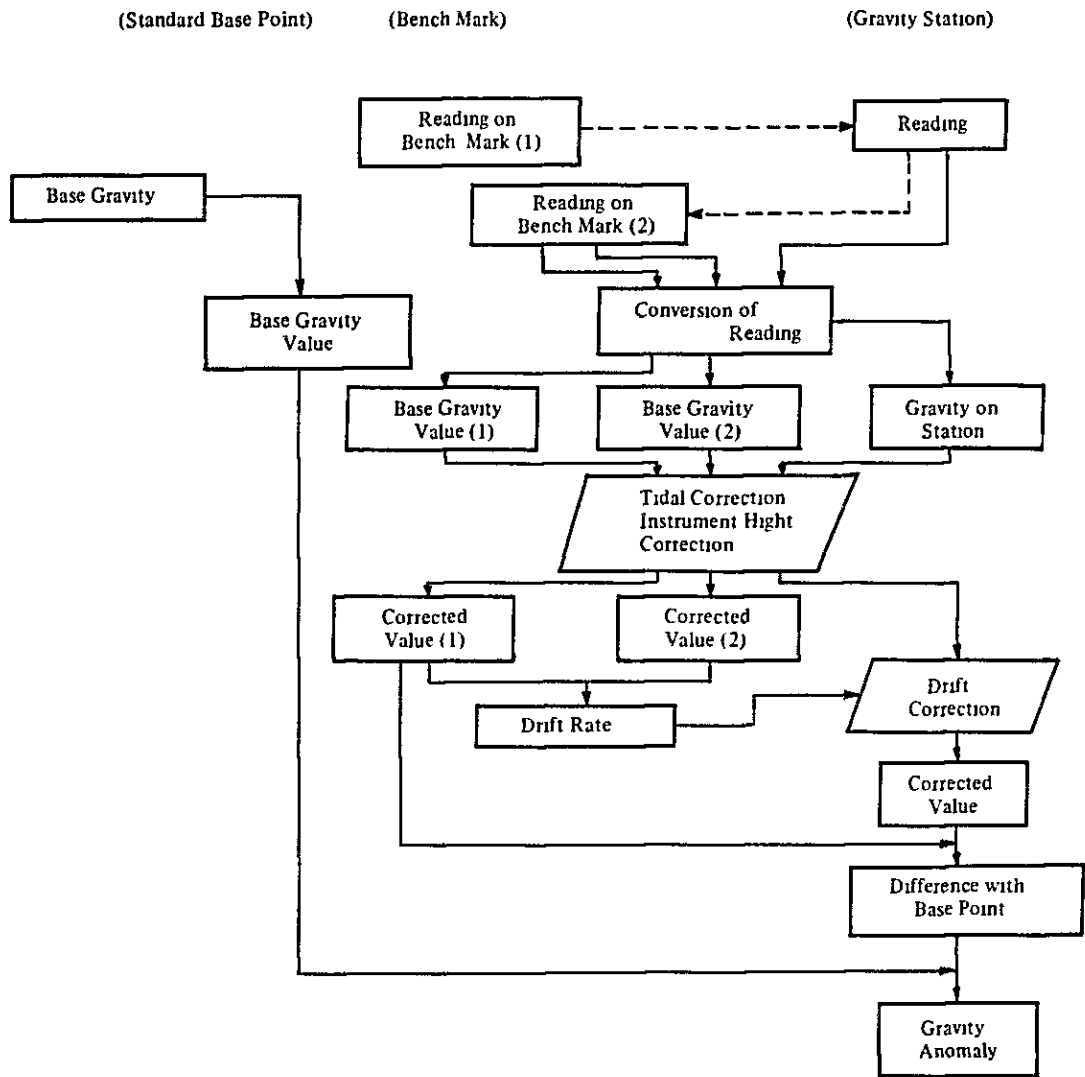


Fig. II-2-3

Flow Chart of Gravity Data Arrangement





Table II-2-1 Milligal Value for Model G Gravimeter #372 and #454

Counter Reading	#372		#454	
	Value in Milligal	Factor for Interval	Value in Milligal	Factor for Interval
2100	2243.35	1.06780	2204.69	1.05125
2200	2350.13	1.06782	2309.81	1.05142
2300	2456.91	1.06785	2414.95	1.05159
2400	2563.70	1.06788	2520.11	1.05179
2500	2670.49	1.06791	2625.29	1.05199
2600	2777.28	1.06794	2730.49	1.05218
2700	2884.07	1.06797	2835.71	1.05238

Table II-2-2 Gravity Standard Values

	# 372		# 454			
	Itapetininga (40138B)	Adrianopolis (9000)	Itapetininga (40138B)	Itapetininga (40138B)	Adrianopolis (9000)	Itapetininga (40138B)
Latitude	23° 35.57'S	24° 40.27'S	23° 35.57'S	23° 35.57'S	24° 40.27'S	23° 35.57'S
Longitude	48° 02.49'S	48° 59.88'S	48° 02.49'S	48° 02.49'S	48° 59.88'S	48° 02.49'S
Date of Observation	1981.7.23	1981.7.23	1981.7.23	1981.7.23	1981.7.23	1981.7.23
Time of Observation	11h35m	16h11m	21h34m	11h41m	16h17m	21h40m
Reading Value	2,352.547	2,537.053	2,352.525	2,228.201	2,415.550	2,228.152
Milligal Value	2,513.020	2,710.058	2,512.000	2,339.461	2,536.465	2,339.410
Earth Tide Correction (mgal)	-0.056	+0.071	+0.018	-0.057	+0.073	+0.016
Instrument Correction (mgal)	0.000	0.000	0.000	0.000	0.000	0.000
Corrected Value (mgal)	2,512.964	2,710.129	2,513.017	2,339.404	2,536.538	2,339.426
Drift Correction (mgal)	0.000	-0.024	-0.053	0.000	-0.010	-0.022
Corrected Value (mgal)	2,512.964	2,710.105	2,512.964	2,339.404	2,536.528	2,339.404
Gravity Value (mgal)	978.634.31	978.831.45	978.631.31	978.631.31	978.831.43	978.631.31

b. Tidal correction

Tidal forces are due to the attraction of the sun and the moon at the earth's surface which deviates in direction, and intensity, with time and from place of observation.

Tidal force due to the sun and the moon is calculated by the following formula.



$$V_{et} = -\Sigma 1.16u$$

$$u = -\frac{3}{2} \cdot G \cdot M \cdot \frac{a}{r^3} \left( 3 \left( \sin^2 \delta - \frac{1}{3} \right) \cdot \left( \sin^2 \varphi - \frac{1}{3} \right) + \sin 2\delta \cdot \sin 2\varphi \cdot \cos \theta + \cos^2 \delta \cdot \cos^2 \varphi \cdot \cos 2\theta \right)$$

where,

- V<sub>et</sub> : Tidal correction
- u : Tidal force of the planet
- G : Gravitational constant
- M : Mass of planets (the sun and the moon etc.)
- a : Distance from center of earth to observation point
- r : Distance between earth and planet
- δ : Declination of the planet (angle from equator to south or north)
- φ : Latitude at observation point
- θ : Angle of the planet (angle between terrestrial and planetary meridian plane)

c. Instrument height correction

This correction is used to adjust the instrument height from the station elevation surveyed by leveling.

$$V_{hi} = 0.3086 h_i \times 100$$

where,

- V<sub>hi</sub> : Correction of instrument height
- h<sub>i</sub> : Height from station level to top of gravimeter (cm)

d. Drift correction

Drift is an inherent characteristic error of gravimeter which changes proportionally with time. The rate of change in drift is not always constant as it depends upon the characteristics of a gravimeter, temperature and pressure of the atmosphere and the way of handling of the instrument. So, in this survey the closure error was regarded as drift and distributed by time allotment.

e. Gravity value

Correction on the observed value are as follows:

$$V_c = V_{rk} + V_{hi} + V_d$$

where,

- V<sub>c</sub> : Corrected gravity value
- V<sub>rk</sub> : Observed gravity value
- V<sub>d</sub> : Drift correction value



The gravity value ( $g$ ) is observed by adding a difference ( $Dg$ ) of corrected gravity ( $Vc$ ) and the corrected gravity at the bench mark ( $Vg$ ) with a base point gravity ( $Bg$ ), which has the same value as the international standard gravity.

$$Dg = Vc - Vg$$

$$g = Bg + Dg$$

## (2) Correction of Gravity

A flow chart of various corrections from a reading to a Bouguer anomaly is shown on Fig. II-2-4

### a. Free air correction

This is required correction for the elevation of gravity station because the measurement was made at a different distance from the center of the earth. The first term of the elevation correction is 0.3086 mgal/m. This is called as the elevation correction together with Bouguer correction.

$$\delta g_o = 0.3086 \cdot H_m$$

where,

$\delta g_o$  . Free air correction

$H_m$  . Altitude of the station (m)

### b. Terrain correction

A topographic irregularity (hill, knoll, slope, etc.) will exert an attraction directly proportional to its density. The vertical component of this attraction will be directed upwards and this reduces the gravity.

A term of this magnitude must therefore be added to the measured value of gravity. A station near valley is negative mass and the vertical component of its attraction will also be directed upwards leading again to an additive topographic correction.

The topographic correction is calculated by dividing the area around a station in compartments into 5 groups, namely, "far", "medium", "near", "neighbour" and "close".

The range and size of grid are shown on Table II-2-4.

The range of correction listed on Table II-2-4 means the radius of a circular plate with the gravity station as its center and without overlapping.

#### i) Terrain correction of far, medium and near

For the correction of far, medium and near, altitude informations are based on the grid of latitude and longitude of a cartesian coordinate and altitudes are read by a circular plate shown in Fig. II-2-5.



Table II-2-3 Error and Correction Value of Closed Leveling Loop

Order	Route	Observed Elevation (m)	Closed Error (m)	Decided Elevation (m)	Distance of Closed Loop (D, km)	Correction Value (m)	Precision Required $\sqrt{D}$ (m)
First	109 - 120 - 125 - 129 - 130 - 203 - 141 - 157 - 171 - 178 - 109	865 817	1 639	864 178	27.5	-1 639	1.936
Second	203 - 218 - 233 - 157	329 610	0 674	328 936	17 0	+0 674	1 303

Table II-2-4 Range and Size of Grid for Topographic Corrections

Kinds of Correction	Range radius (km)	Grid Interval		Topographic Map Used
		X (m)	Y (m)	
Far	16.00 - 64.00	6736 ( 4' )	7384 ( 4' )	1/50,000
Middle	4.00 - 16.00	1684 ( 1' )	1846 ( 1' )	1/50,000
Near	0.5 - 4.00	281 ( 10" )	308 ( 10" )	1/25,000
Neighbour	0 02 - 0.5			1/10,000 and 1/25,000
Close	0.00 - 0.02			sketch





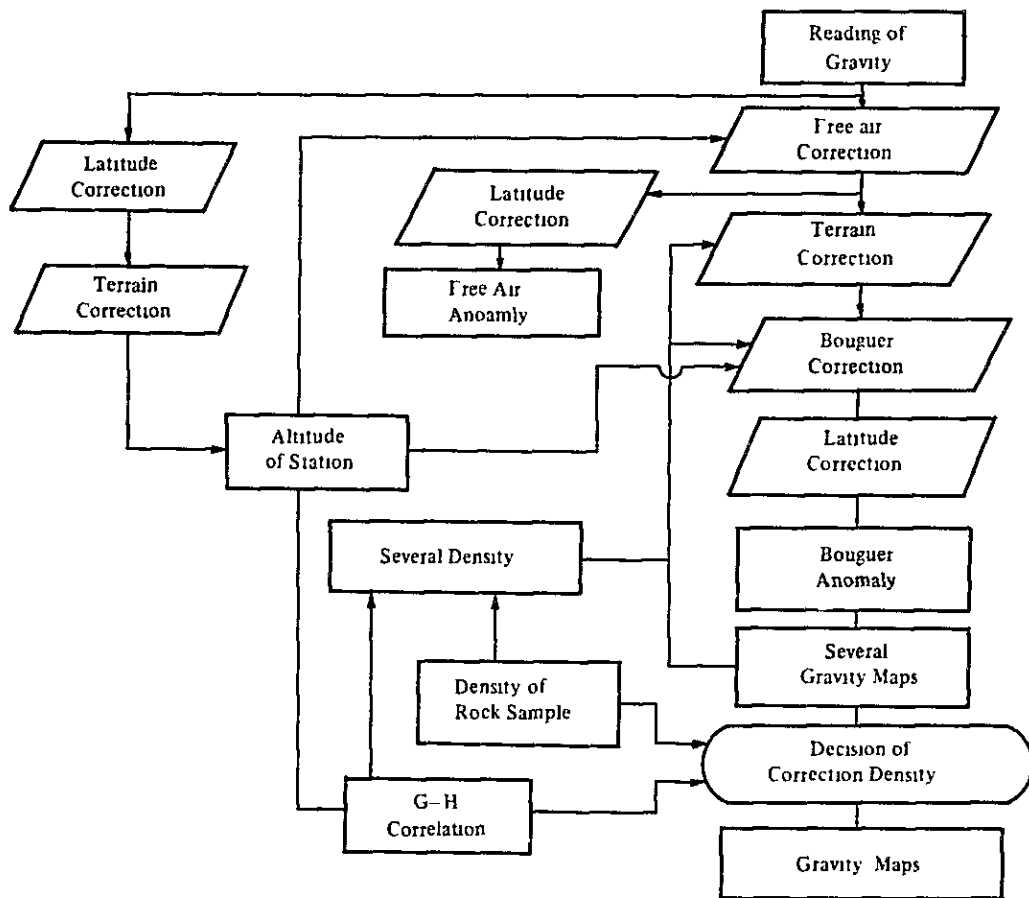


Fig. II-2-4 Flow Chart of Gravity Data Processing



Average of all altitudes in each component is used for the correction and total computed terrain correction by a formula shown below is called as far, medium or near depending upon the size of the radius.

$$\delta g_o' = \frac{2\pi}{n} G\rho(R_1 - R_2 - \sqrt{R_1^2 + (H - H')^2} + \sqrt{R_2^2 + (H - H')^2})$$

where,

$\delta g_o'$  : Terrain correction

$n$  : Number of component

$G$  : Gravitational constant

$\rho$  : Correction density

$R_1$  : Shorter radius of a component

$R_2$  : Longer radius of a component

$H-H'$  : Difference of altitude between station and average height of a component

A component in the circular plate is designed to involve at least one grid intersection of latitude and longitude.

ii) Terrain correction of neighbour

For the correction of neighbour a circular plate divided into 66 components as shown in Fig. II-2-6 with radius of 20 to 1,000 m is used. The same method and formula are adopted for the calculation.

iii) Terrain correction of close

The nearest topography within 20 m from the gravimeter is sketched and a two-dimensional topographic section is simply modified as mentioned below. The correction due to the close cliff, slope and channel are calculated. as,

$$\begin{aligned} \delta g_o' &= G\rho f \int_D^R \frac{\sqrt{R^2 - X^2}}{-\sqrt{R^2 - X^2}} \int_0^{H+(X-D)\tan\beta} \frac{ZdXdYdZ}{(X^2+Y^2+Z^2)^{3/2}} \\ &= 2G\rho f \int_D^R \frac{\sqrt{R^2 - X^2}}{-\sqrt{R^2 - X^2}} \left( \frac{1}{\sqrt{X^2 + Y^2}} - \frac{1}{\sqrt{X^2 + Y^2 + (H-D\tan\beta)^2}} \right) dX \\ &= 2G\rho f \int_D^R \left( \log \left| \frac{R - \sqrt{R^2 - X^2}}{R + \sqrt{R^2 - X^2}} \right| - \log \left| \frac{\sqrt{R^2 + (H-D\tan\beta + X\tan\beta)^2} - \sqrt{R^2 - X^2}}{\sqrt{R^2 + (H-D\tan\beta + X\tan\beta)^2} + \sqrt{R^2 - X^2}} \right| \right) dX \end{aligned}$$



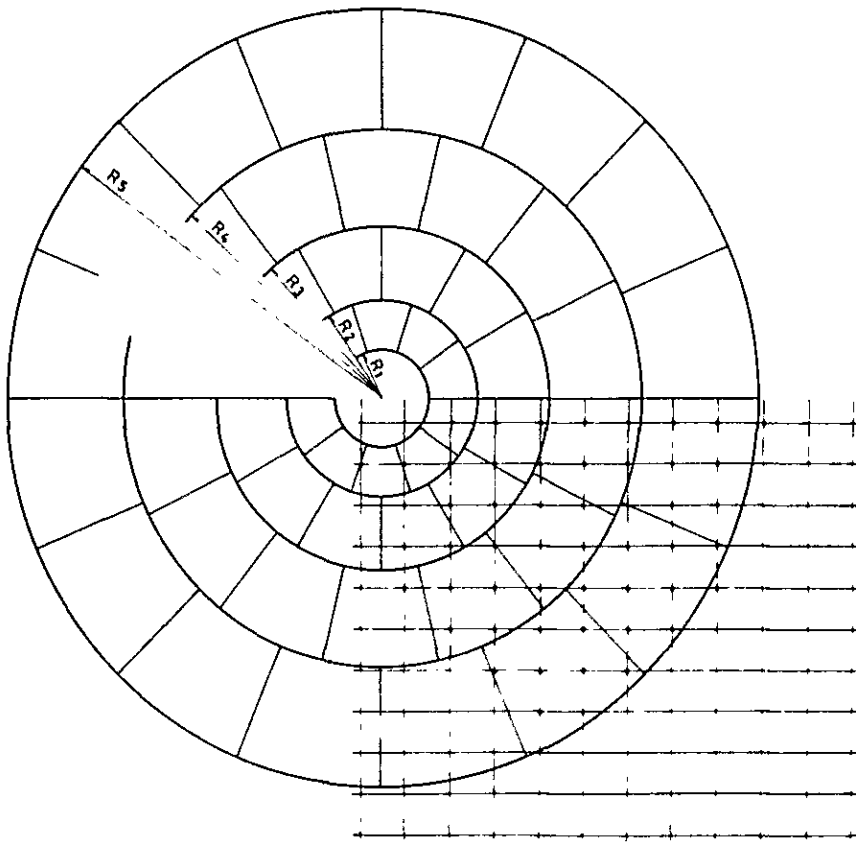


Fig. II-2-5 Disc used for Terrain Correction(Far, Middle and Near)

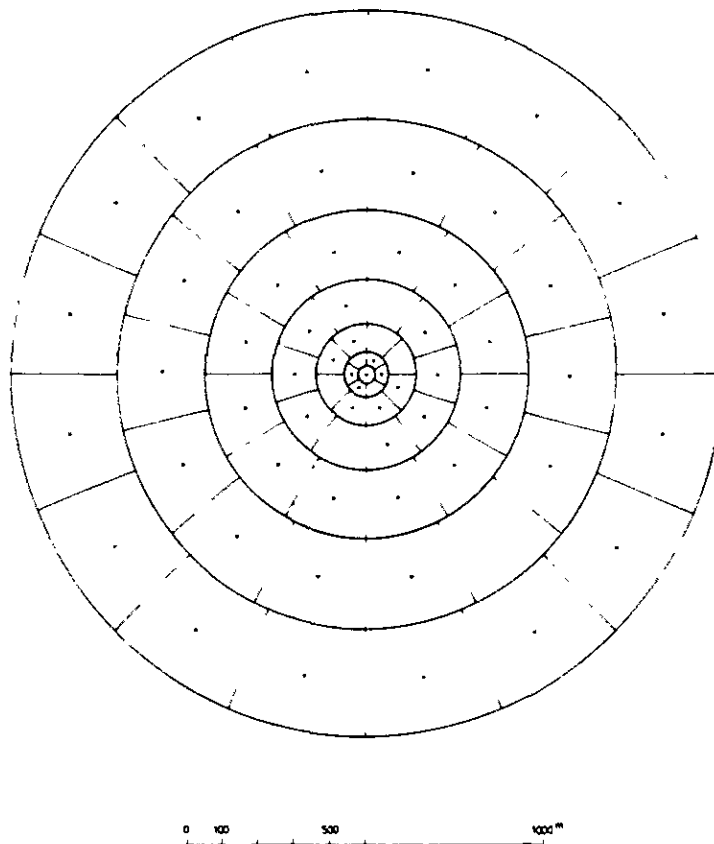
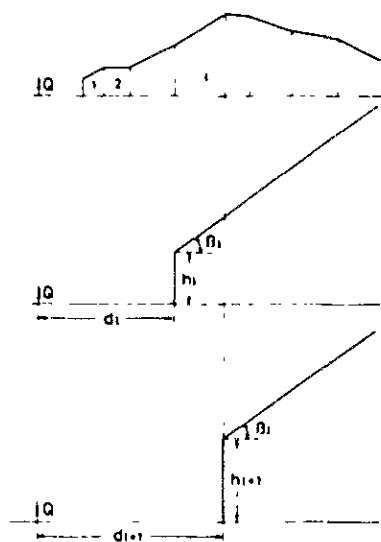
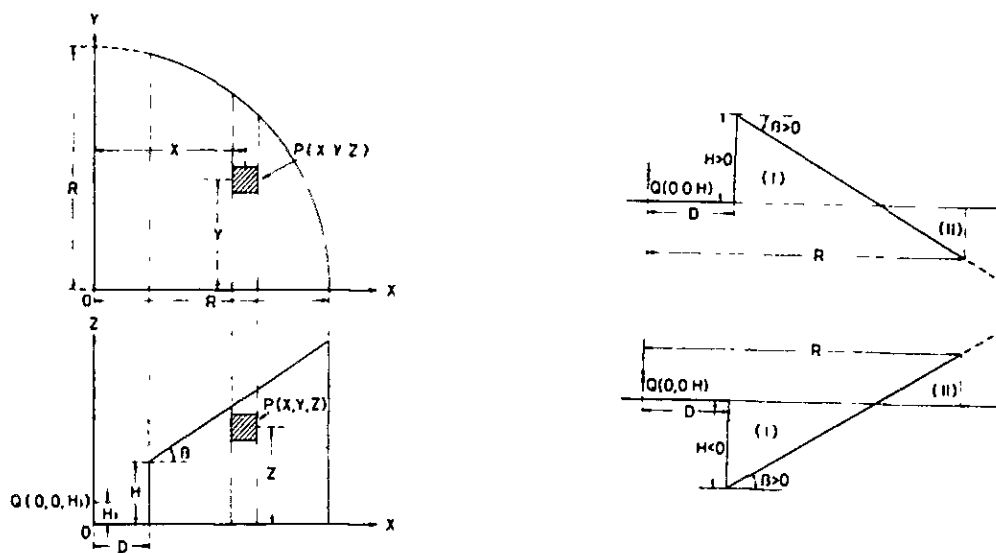


Fig. II-2-6 Disc used for Terrain Correction(Neighbour)



This integration can not be expressed by a primary function, then a digital integration by means of Simpson 1/3 law is used.

When terrain is rugged, the topography should be divided into many blocks as shown below and the summation of each calculated values becomes the total correction of close.







c. Bouguer correction

Bouguer correction is one of the height correction caused by the attraction of the rock mass between the station and the sea level or the absent mass between them. Bouguer correction is given as follows:

$$\delta g_{\text{Bou}} = -2\pi G \rho H_m = 0.0419 \rho H_m$$

where,

$\delta g_{\text{Bou}}$ : Bouguer correction

$H_m$  : Altitude of the station in meter

$\rho$  : Specific gravity (density) of the intervening rock

d. Latitude correction

The attraction of gravity on earth decreases towards the equator and increases towards poles because of the centrifugal force resulting from earth's rotation and of the earth's radius due to polar flattening.

As it is the function of latitude  $\phi$ , gravity anomaly which is the difference of absolute gravity and theoretical gravity includes the latitude correction in itself.

In 1930 International Gravity Formula was adopted by IUGG (International Union of Geodesy and Geophysics) which is,

$$\gamma_{1967} = \frac{a\gamma_E \cos^2 \phi + b\gamma_P \sin^2 \phi}{a^2 \cos^2 \phi + b^2 \sin^2 \phi}$$

$a=6,378,140$  m . Radius of the earth at the equator

$b=6,356,180$  m : Radius of the earth at the pole

$\gamma_E=978\ 032$  gal . Standard gravity at the equator

$\gamma_P=983\ 218$  gal Standard gravity at the pole

In this survey, the above formula (1967) is used for the calculation of standard gravity. The difference between International Gravity Formula  $\gamma_I$  and Normal Gravity Formula  $\gamma_N$  is,

$$\gamma_N - \gamma_I = -17.2 + 13.6 \sin^2 \phi \text{ (mgal)}$$

e. Bouguer anomaly

The difference between the corrected gravity value resulting from the above mentioned corrections and the standard gravity, is called as Bouguer anomaly,

$$\Delta g_{\text{Bou}} = g + \delta g_{\text{Bou}} + \delta g_{\text{lat}} + \delta g_{\text{lat}} - \gamma_I$$

where  $\Delta g_{\text{Bou}}$  is Bouguer anomaly value.



The Bouguer anomaly depends on rock densities. Eight density maps have been made (densities of 2.0, 2.40, 2.50, 2.60, 2.67, 2.70, 2.80 and 2.90) for both density and terrain.

#### 2-2-2 Method of Analysis

Results of this investigation are quantitatively and qualitatively interpreted, using the Bouguer anomaly map and the result of surface fit analysis together with its residual map. Two-dimensional section analysis using Talwani's method is performed quantitatively.

##### (1) Density Assumption

Although only one assumption is necessary in the analysis of data derived from the gravity survey, it is difficult to interpret geological structure by using only one density data. Assumption of the proper density has been made in several ways as mentioned below and by their combination.

##### a. Density of rock samples

In this survey, 58 rock samples were collected on the ground surface in the vicinity of the survey of the survey area and their dry and wet densities were measured. The results of density measurement are shown on Table II-2-5 and the average densities on Table II-2-6. Sample locations are shown in PL. II-1.

In this survey area, the Pre-Cambrian rocks are distributed dominantly so that the average densities are high as like 2.5 to 3.1 gr/cm.

The average density of mica schist group is 2.56, amphibolite calco-silicate rock group 2.85, quartzite group 2.63, and gneiss group 2.73. The former three groups belong to Açungui I formation and the latter one belongs to Setuva formation considered as basement rocks. And as intrusive rock, average density of granite is 2.64, syenite 2.68 and gabbro 2.93. Consequently, four layered density model is supposed with the upper density 2.5, second 2.8, third 2.6 and the basement as 2.70 intruded by 2.6 and 2.9 rocks.

The total average of all rock samples is 2.77.

##### b. G-H correlation

Gravity decreases with the altitude of measurement. The rate of decrement is nearly equal to the coefficient of elevation correction,  $0.3086-0.0419\rho$ . Therefore, when the gravity data are plotted as the altitudes on one side and latitude-corrected gravity on the other axis, the gradient of the linear line fit to the plots represents the average of rock densities in the area.



Table II-2-5 Density of Rock Samples

		Sample No	Rock Name	Density (gr/cm <sup>3</sup> )				
				Dry	Wet	Average		
Setuva Formation	Gneiss Group	1	Mica Schist	2.68	2.60	2.73		
		2	Mica schist	2.67	2.67			
		3	Mica schist	2.83	2.82			
		4	Gneiss	2.61	2.60			
		5	Amphibolite	2.87	2.86			
		6	Mica schist	2.63	2.59			
		7	Gneiss	2.84	2.83			
		8	Gneiss	2.73	2.72			
		9	Gneiss	3.11	3.11			
		10	Gneiss	2.77	2.77			
		11	Gneiss	2.83	2.84			
		12	Gneiss	2.66	2.65			
Acungui I Formation	Quartzite Group	13	Quartzite	2.65	2.65	2.63		
		14	Quartzite	2.63	2.60			
		15	Quartzite	2.64	2.61			
		16	Quartzite	2.65	2.65			
		17	Quartzite	2.55	2.56			
		18	Quartzite	2.64	2.64			
		19	Quartzite	2.54	2.55			
		20	Quartzite	2.63	2.64			
		21	Quartzite	2.54	2.55			
		22	Amphibolite	2.77	2.75			
		23	Mica schist	2.77	2.76			
		24	Mica schist	2.94	2.94			
	Calco-Silicate Rock Group	25	Calco-schist	2.91	2.92	2.82		
		26	Calco-Silicate rock	2.94	2.97			
		27	Mica schist	2.72	2.71			
		28	Mica schist	2.79	2.83			
		29	Phyllite	2.57	2.62			
		Mica Schist	31	Sericite schist	2.43		2.41	2.86
			32	Sericite schist	2.46		2.50	
	34		Limestone	2.80	2.80			
	36		Mica schist	3.09	3.08			
	37		Amphibolite	2.77	2.63			
	38		Amphibolite	3.10	3.07			
	39		Mica schist	2.54	2.51			
	Amphibolite Group	40	Amphibolite	3.02	3.01	2.86		
		41	Amphibolite	2.68	2.61			
		42	Amphibolite	3.06	3.01			
		43	Mica schist	3.01	3.00			
		44	Mica schist	2.77	2.77			
		45	Mica schist	2.86	2.86			
		46	Mica schist	2.97	2.95			
		Mica Schist	30	Limestone	2.84		2.84	2.65
	33		Graphite schist	2.42	2.42			
	35		Phyllite	2.69	2.68			
	Intrusive Rock	Granite Group	47	Granite	2.65	2.65	2.64	
48			Granite	2.68	2.67			
49			Granite	2.64	2.65			
50			Granite	2.65	2.63			
51			Granite	2.62	2.64			
52			Granite	2.62	2.61			
53			Granite	2.62	2.62			
Syenite Group		54	Syenite	2.68	2.66	2.68		
		55	Syenite	2.76	2.74			
		56	Syenite	2.64	2.65			
Gabbro	57	Gabbro	2.93	2.93	2.93			
		58	Bante	4.21	4.20			
Average				2.73				









Fig. II-2-7 shows the G-H correlation for this survey and the calculated density is 2.80 by the least square method

c. Determination of correction density

The correction density is determined to be 2.80 from both the average density and G-H correlation. Bouguer anomaly maps were drawn for two cases of density  $\rho=2.70$  and  $\rho=2.80$ , and better correlation with the geological structure was observed in the case of  $\rho=2.80$ , which used for interpretation.

(2) Surface Fit Analysis

Surface fit analysis shows the general trend of gravity feature, which is known to express gravity anomaly due to deep or large-scale structures in the vicinity of the survey area. On the other hands, the residual indicates short wavelength gravity anomalies caused by shallow and small-size structures.

The third and fifth order surface fit analyses were carried out with the following formula.

$$g(x,y) = \sum_{i=0}^m \sum_{j=0}^m a_{ij} x^i y^{m-j}$$

where,

- $g(x,y)$  : Surface fit
- $a_{ij}$  : Coefficients of polynomial
- $x,y$  : Coordinates

The coefficients are determined by the least square method using the gravity data  $G(x,y)$ . The residual is calculated by removing the polynomial surface from the Bouguer anomaly.

(3) Two-dimensional Analysis

Geological structure causing the gravitational anomaly is assumed to be as follows;

- a. Polygonal structures with different density
- b. Stratified structure of which density increase with depth
- c. Two layered structure with sediments of constant density and the basement

Judging from the geological structure and its residual gravity, either of the structures and their combinations are generally applied.

In this case, Talwani's method are adopted.

In two-dimensional section analysis, Bouguer values calculated from an assumed density structure are compared with observed Bouguer values. The density structure is modified until the calculated Bouguer values fit well with the observed values by trial and



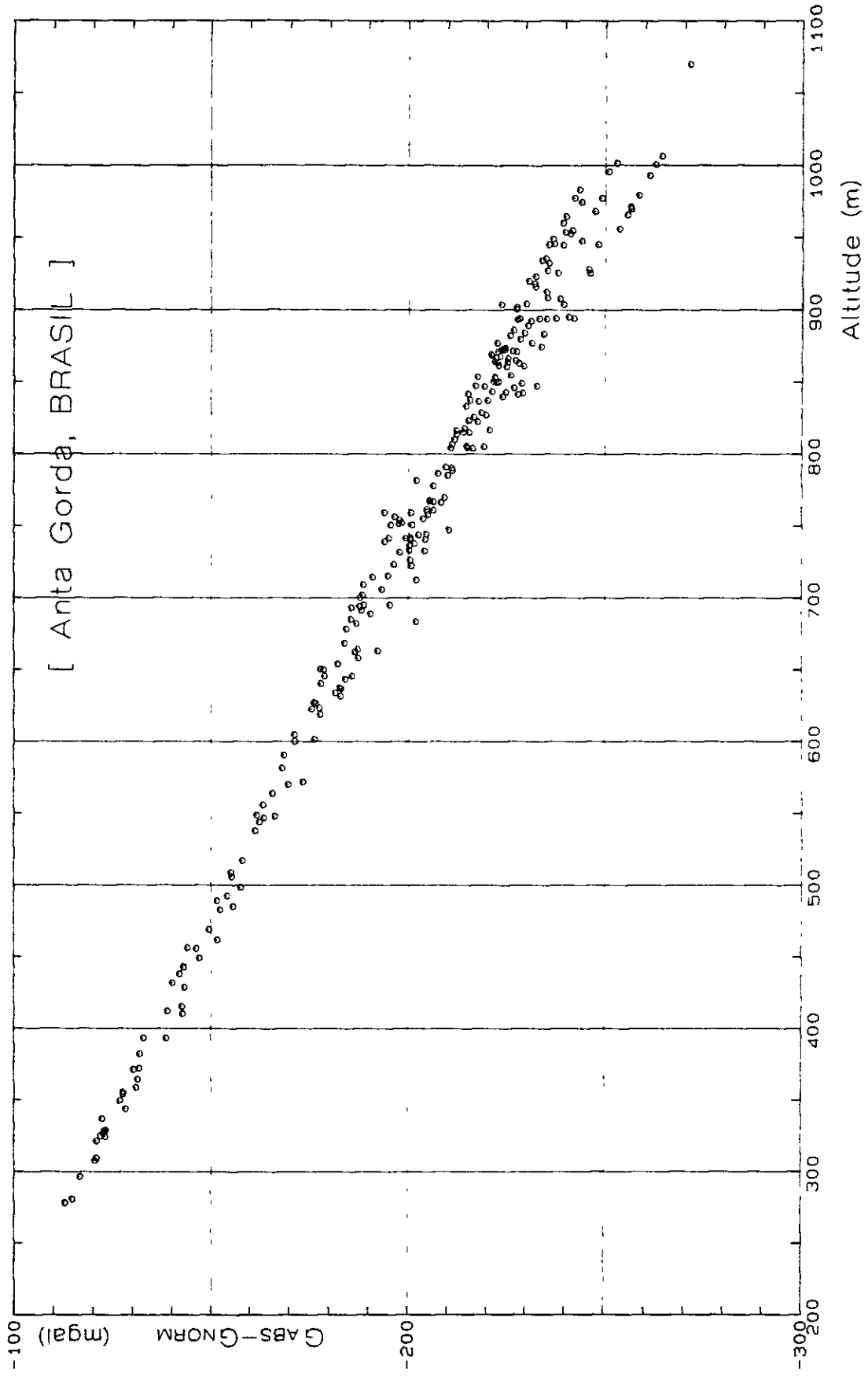


Fig. II-2-7 G-H Correlation



error. Calculation of Bouguer values is performed by an electronic computer using Talwani's formula, taking the lateral effect of anomaly into consideration.

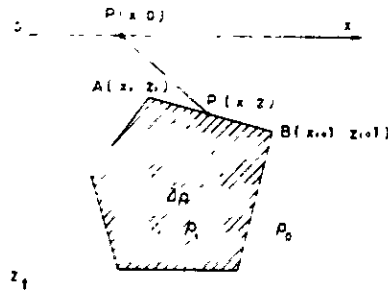
$$\Delta g = 2G\Delta\rho \sum Z_i$$

$$Z_i = \frac{(x_{i+1} - X_i) \{ Z_i(X - X_{i+1}) - Z_{i+1}(x - x_i) \}}{(x_{i+1} - x_i)^2 + (z_{i+1} - Z_i)^2}$$

$$x \left\{ \tan^{-1} \frac{Z_i}{x_i - x} - \tan^{-1} \frac{Z_{i+1}}{x_{i+1} - x} + \frac{1}{2} \frac{Z_{i+1} - Z_i}{x_{i+1} - x_i} \log \frac{(x_{i+1} - x)^2 + Z_{i+1}^2}{(x_i - x)^2 + Z_i^2} \right\}$$

When an edge of polygon is rectangle ( $X_i = X_{i+1}$ ),

$$Z_i = \frac{x_i - x}{2} \log \frac{(x_i - x)^2 + Z_{i+1}^2}{(x_i - x)^2 + Z_i^2}$$



## 2-3 Results of Analysis

Data of this gravity survey, such as Bouguer anomaly, the fifth order surface fit and residual maps, are qualitatively and quantitatively treated in the following manner.

### 2-3-1 Bouguer Anomaly Map

Among the assumed densities of 2.0 to 2.9, two kinds of densities are used to make Bouguer anomaly maps. Topography of this area is so rugged that a pattern of the contour map considerably changes by a slight change of density of 0.1. On Plates II-1 and II-2, Bouguer anomalies shown with the density of 2.70 and 2.80 respectively. Among them, assumed density of 2.80 is selected as it reflects the geological structure better than the others with less terrain effects

The total relief of the Bouguer anomaly map is over 15 mgals, with a high of -51 mgal in the southwestern corner to a low of -66 mgal in the northwestern corner. The more apparent feature is a northeast-striking belt of gravity contours which coincides to the main geological structure with NE-SW trend in this area.



The northwestern corner is dominated by gravity low with the lowest gravity anomaly value of  $-66$  mgal, indicating less dense rock. This gravity low is enclosed at its east and south sides with NE-SW trending gravity high from Epitacio Pessoa through Praia Grande towards Quilo Metro Quarenta, corresponding to dense rocks. In the southern area of this gravity high, the relief is as small as 3 mgal, with a high of  $-55$  mgal to a low of  $-58$  mgal.

Northwest gravity low corresponds to granite and gravity high to Pre-Cambrian rocks.

The closely spaced gravity contours along the northwest margin of NE-SW trending gravity high indicates the NE-striking fault structure with the downthrown on northwest.

The NE-trending gravity high indicates dense rocks at shallow depth, which may correspond to gabbro in comparison with the aeromagnetic results in which highly magnetized rocks are assumed as dyke at similar location

In Bouguer anomaly map, gneiss group of Setuva formation considered as basement rock corresponds to relatively gravity low.

#### 2-3-2 Fifth Order Surface Fit Map

The third and fifth order surface fit analyses were conducted. Better approximation to Bouguer anomaly map are observed in the fifth order surface fit map, which is used for interpretation.

The polynomial surface appears to approximate sufficiently the regional trend corresponding to the regional density structure.

On the fifth order surface fit map, the NE-trending gravity contours appear more clearly than Bouguer anomaly map.

#### 2-3-3 Fifth Order Residual Map

The fifth order residual map is shown on PL. II-6, in which the contour interval is 0.2 mgal to detect closure of gravity anomalies with small relief effectively.

This map helps to clarify many of shallow and small size structures. In particular, several of dense or relatively dense rocks are delineated better on the residual map because dominating effect of the regional gravity trend is removed.

(a) The gravity high at the northwest corner corresponds with granite and suggests that granite is concealed at shallow depth at the south of its outcrop.

(b) The steep gravity gradients along the northwest side of the NE-trending gravity high, indicating dyke of gabbro as mentioned at 2-3-1, corresponds to the NE-striking fault.

As these gravity highs are consisted of several of 3 mgal closure, the dyke structure





may be divided into some blocks.

(c) Gravity low between the northwest gravity high and the NE-trending gravity high indicates mica schist group of Açungui I formation with less density than granite.

(d) Two gravity lows at 2 Km northeast and 1 Km southeast of Perau mine may be connected together and indicate quartzite group and mica schist-amphibolite-calco-silicate group of Açungui I formation respectively. Perau mine locates on the gravity ridge between above-mentioned two gravity lows and it is suggested that this ridge may be a continuity of the gravity high mentioned at (e).

(e) The gravity high at about 2 Km southeast of Perau mine is attributed to limestone, mica schist-amphibolite-calco-silicate rocks group of Açungui I formation and partly gneiss group of Setuva formation at the south corner. From the extensions of this gravity high, it is suggested that limestone may continue to the northwest and amphibolite-calco-silicate rock group to the southwest. And also the extension to the southeast suggests that gneiss group continues to the same direction and is connected to the gravity high mentioned at (g).

(f) The gravity low southwest of gravity high (e) is attributed to quartzite group of Açungui I formation.

(g) The gravity high distributed from Serra do Cadeado towards 2 Km west of Anta Gorda, where a minor gravity low is dominated on Bouguer anomaly map, indicates gneiss group assumed as basement rock and extends to north. It is suggested that there exists anticlinal structure running along the central axis of this gravity high.

(h) The gravity low in the southeast corner corresponds to quartzite group and suggests the synclinal structure along its central axis.

#### 2-3-4 Two-Dimensional Section Analysis

In this survey area, geological structure with NE trend is dominant so that Bouguer anomaly map is characterized by the northeast-trending gravity contours. Four NW-SE profiles are selected perpendicular to the NE trend as two-dimensional analysis.

Assuming the densities of the model from the result of the density measurement, the first layer would be mica schist group ( $\rho_1=2.50$ ), the second layer be mica schist-amphibolite calco-silicate rocks group  $\rho_2=2.75$ , the third layer be quartzite group  $\rho_3=2.60$ , the fourth layer be gneiss group  $\rho_4=2.70$  and the intrusive rocks be granite ( $\rho_5=2.60$ ) and gabbro ( $\rho_6=2.95$ ). The first, second and third layers belong to Açungui I formation and the fourth layer to Setuva formation.



It is required to set a control point in order to decide the depth of boundary. Gneiss group outcrops, assumed to be basement rocks, are exposed near No. 40, No. 36, No. 37 and No. 33 of Profile A-A', B-B', C-C' and D-D' respectively so that these points are used as control points of each profiles.

As a result of two-dimensional analysis, dense rocks are assumed below the NE-trending gravity high. According to the aeromagnetic analysis results of Phase I survey, as highly magnetized rocks are estimated at similar location, this dense and highly magnetized rock may correspond to gabbro as dyke.

(1) Profile A-A' (Fig. II-2-8)

This profile is the northernmost one among four profiles. A major high-angle fault with the northwestern block downthrown and its bed dipping northwest is assumed at No. 30. Dense rocks may intrude at the southeast side of this fault.

Granite is exposed broadly northwest of No. 9.

Gneiss group of basement rocks are exposed to the southeast of No. 39 and dips at 30 degrees to the northwest from No. 39, being overlaid by quartzite group with a thickness of 100 to 200 m between Nos. 24 and 39. In the area between granite and above-mentioned fault (No. 9 to No. 23), a depth of gneiss group is about 2,000 m and the first to fourth layers are stratified at a dip of 30 degrees to northwest. A thickness of the second layer (mica schist-amphibolite-calco-silicate rocks group) is about 2,000 m and the first layer (mica schist group) are distributed between Nos. 9 and 17.

(2) Profile B-B' (Fig. II-2-9)

Profile B-B' is a cross-section across Perau mine (near No. 18).

A major fault with a downthrown on northwest at No. 20.5 and dense rock at its southwest side are assumed similarly as profile A-A'.

Gneiss group of the fourth layer is exposed southeast from No. 29 and dips at 30 degrees to northwest, being overlaid by the second and third layers. Two anticlinal and one synclinal structures are assumed at No. 30, No. 35 and No. 31 respectively. Maximum thickness of the third layer is 300 m.

In the northwest area of the fault (No. 9.5 to No. 20.5), the first to fourth layers are stratified at a dip of 30 degrees to northwest, and the second layer is not exposed, being overlaid by the first layer. So amphibolite and amphibole schist distributed on geological map in this area may be thin.

Granite is distributed between Nos. 3 and 9.5.

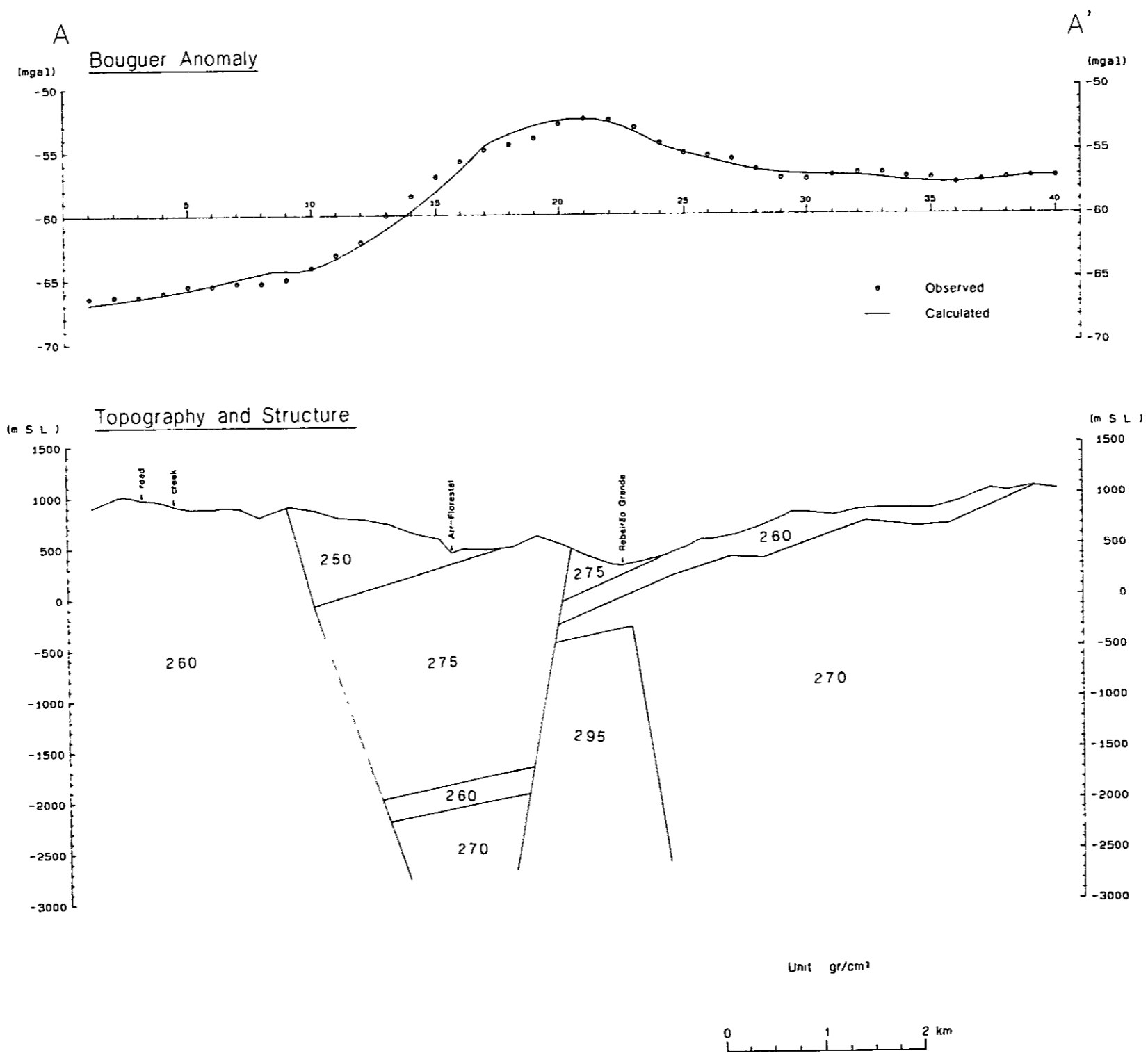


Fig. II-2-8 Gravity Profile and Structure Model(A-A')

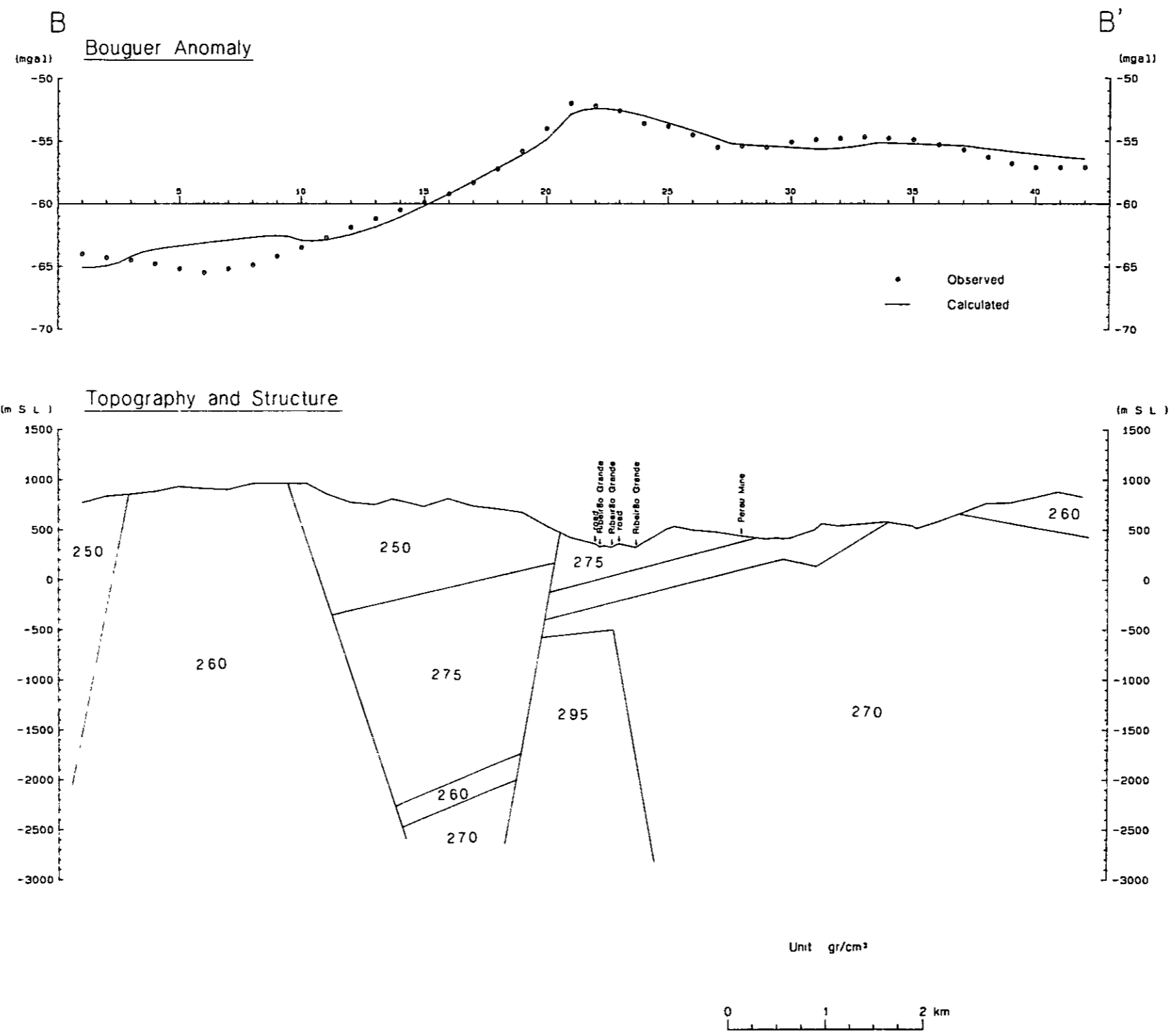


Fig. II-2-9 Gravity Profile and Structure Model(B-B')

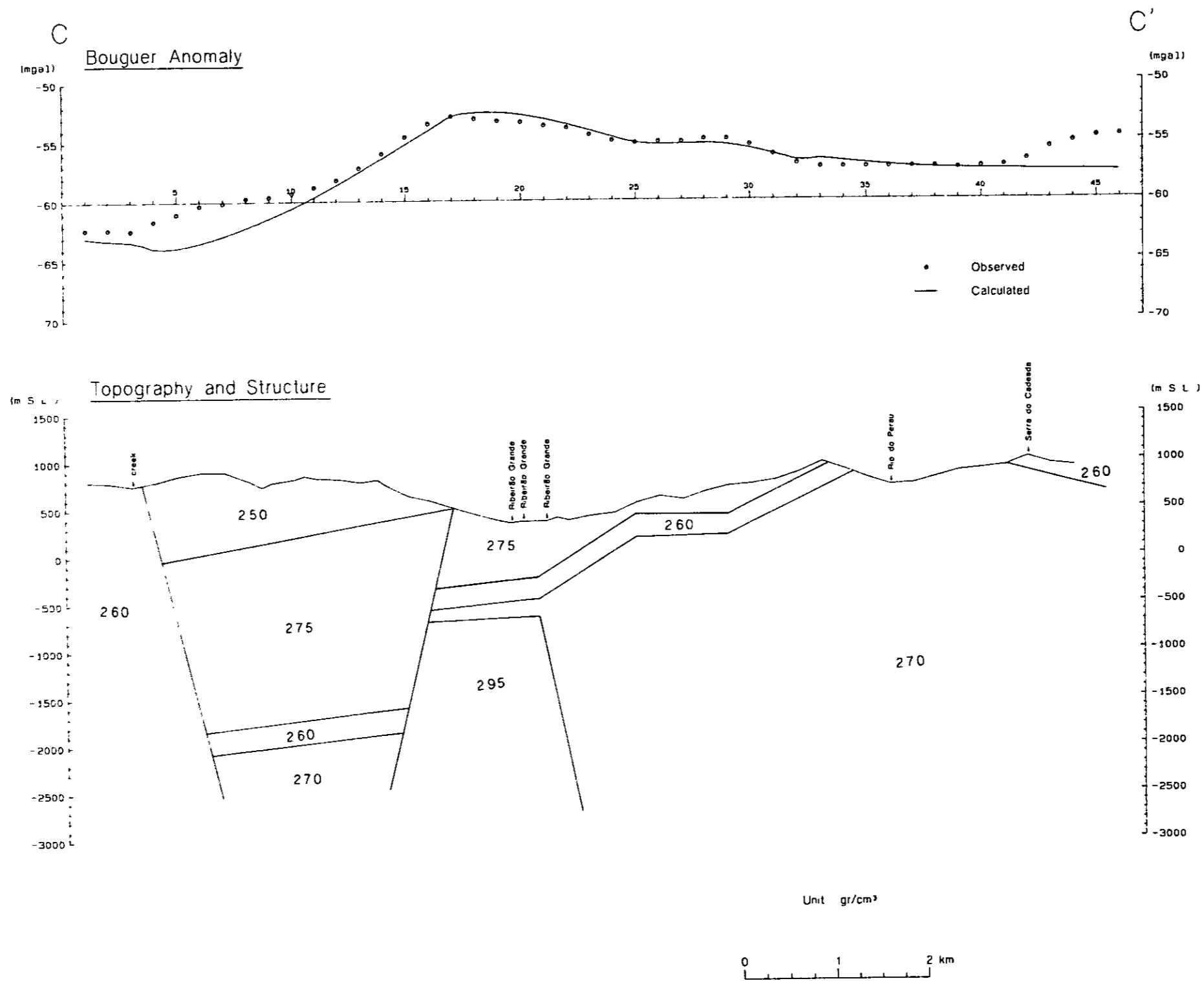


Fig. II-2-10 Gravity Profile and Structure Model(C-C')

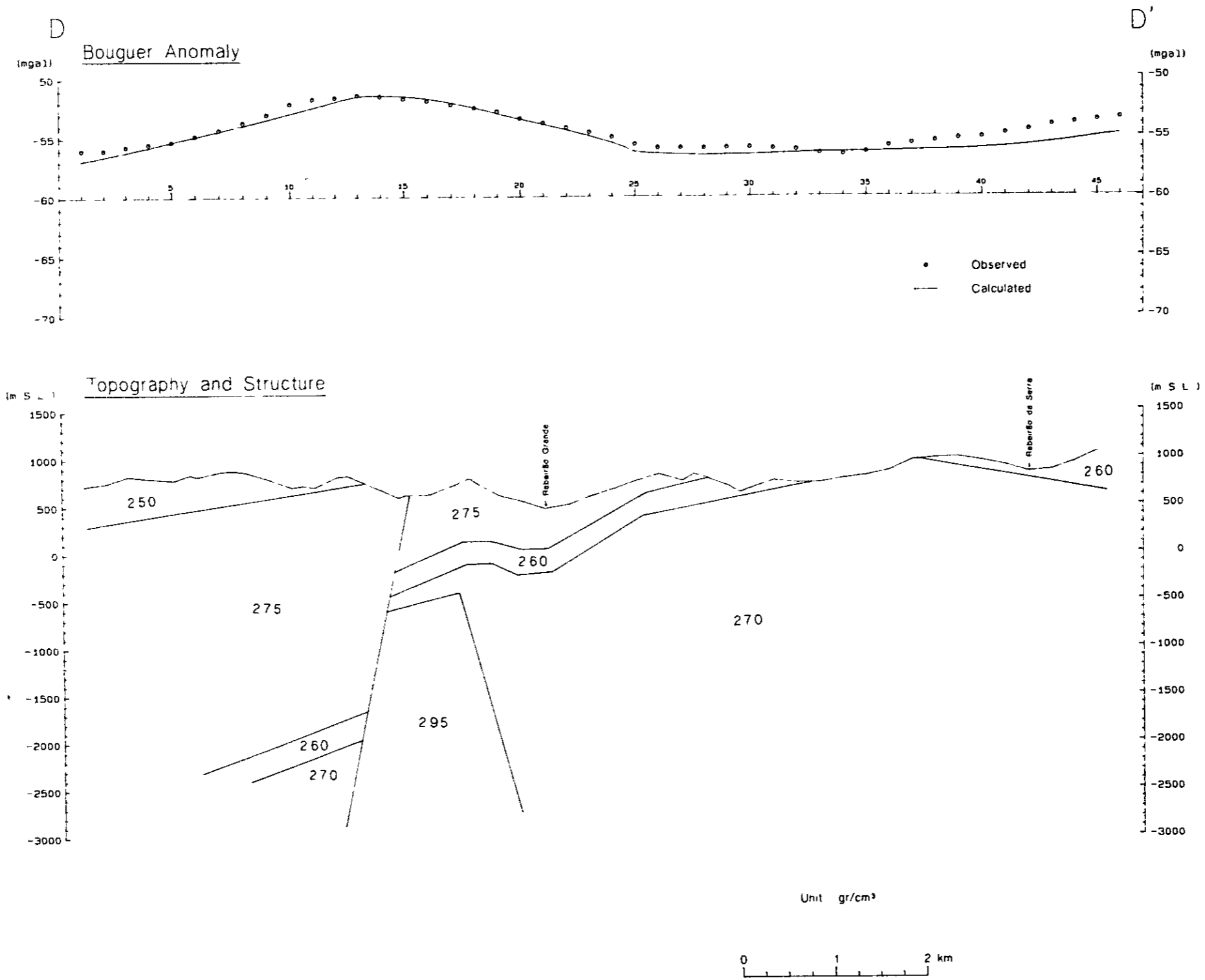


Fig. II-2-11 Gravity Profile and Structure Model(D-D')





(3) Profile C-C' (Fig. II-2-10)

Profile C-C' is a cross-section at 1.5 Km southeast of profile B-B'.

At No. 17, a major fault with a downthrown on northwest and dense intrusive rock at its southeast side wider than ones at profiles A-A' and B-B' are estimated. Granite as intrusive rock is distributed northwest of No. 3.5. Between Nos. 3.5 and 17, Pre-Cambrian rocks (the first to fourth layers) are stratified, dipping to northwest at 30 degrees.

In the southeastern area from the fault, the fourth layer are exposed southeast from No. 34 and overlaid by the second and third (thickness of 300 m) layers. Two anticlinal and one synclinal structures are assumed at Nos. 25, 35 and 29 respectively.

(4) Profile D-D' (Fig. II-2-11)

Profile D-D' is the southernmost one among four profiles.

The gravity features on this profile is different with ones of other three profiles. No gravity low appears in the northwestern part and long wavelength components are dominant.

A major fault with a downthrown on northwest is assumed at No. 15 and gabbro as intrusive rock at the southeast of this fault is estimated. Northwest of this fault, the first to fourth layers are stratified, dipping at 30 degrees to northwest.

On the other hand, in the southeastern area of the fault, the fourth layer is exposed between Nos. 33 and 37, and dips at 30 degrees to both sides. The fourth layer are overlaid by the third layer at the southeast side and by the second and third layers at the northwest side. A maximum thickness of third layer is about 300 m. Two anticlinal and one synclinal structures are assumed at Nos. 20, 35 and 21 respectively.

PL. II-7 shows the above results synthetically estimated from both the qualitative and quantitative analyses, and geological informations.

## 2-4 Summary

Gravity survey was carried out in the area of about 100 km<sup>2</sup> in the vicinity of Perau mine

The results of the survey can be summarized as follows.

- (1) The apparent feature of Bouguer anomaly map ( $\rho=2.80$ ) is the northeast-trending gravity contours which corresponds to the main geological structure with NE-SW trend in this area.
- (2) On Bouguer anomaly map, gneiss group of Setuva formation, assumed as basement rock, correspond to minor gravity lows but those distributions can not be estimated. On the other hand, those are indicated by gravity highs of 2- or 3- mgals closure on the fifth order residual map.



Gneiss group are exposed near Serra do Cadeado, being anticlinal structure with the northeast trend and dip gently to both wings. To northwest, it dips at 30 degrees repeating minor folding towards a major fault with a northeast strike from Epitacio Pessoa towards Quilo Metro Quarenta with a downthrown of about 1,500 m on northwest, indicated by the closely spaced gravity contours. Northwest of this major fault, its depth is about 2,000 m and it dips 30 degrees to northwest.

(3) Açungui I formation are distributed broadly in the survey area, overlying gneiss group of Setuva formation. Those thickness increases towards northwest at the southern area of the fault and at the northern area is more than 2,500 m at the northern area of the fault.

(4) At the southeast side of a major fault, gabbro considered as intrusive rock along the fault causes gravity highs with northeast-trend.

(5) Granite at the northwestern corner in this area causes gravity low on Bouguer anomaly map and gravity highs of 2- or 3- mgals closure on the fifth residual map. And from the latter's map, it is suggested that granite is distributed at shallow depth at the south of its outcrop.

(6) On the fifth order residual map which reflects the shallow density distribution, the distribution of exposed or burial dense rocks such as mica schist-amphibolite-calco-silicate rocks etc., are understood.

(7) Although Perau mine is located on the gravity ridge on the fifth order residual map, the relation between Perau mine and the geological structure assumed from the gravity data is not clear.



## CHAPTER 3 INDUCED POLARIZATION METHOD

### 3-1 Survey Method

IP phenomenon can be observed in time domain as well as frequency domain. It is an exceedingly complex phenomenon although it superficially resembles the discharge of a capacitor (time domain) or the variation of the impedance of an RC circuit (frequency domain).

#### (1) Frequency domain

In the frequency domain, the apparent resistivity of the ground is measured at two frequencies  $F$  and  $f$  ( $f < F$ ) IP is expressed as the apparent frequency effect.

#### (2) Time domain

By passing DC pulses of duration  $T$  in the ground the magnitude of the observed IP is expressed as  $v/V$  where  $v$  is the decay voltage remaining at a definite time after current cut-off, and  $V$  is the voltage at current on.

#### (3) Phase domain

This is a method to measure the phase angle shift between transmitted waveform and received signal waveform.

#### (4) Spectral IP

By sending multi-frequency into the ground normalized amplitude and phase to the lowest frequency are measured as mentioned in chapter 4.

#### 3-1-1 Field Measurement

Frequency domain IP method which is popularly used to date together with spectral IP are adopted in this survey by dipole-dipole electrode configuration. Eight to ten stainless steel wire electrodes are used as a set of current electrode.

#### 3-1-2 IP Instruments

IP transmitter	CH-T7802	made by CHIBA Electronics Laboratory
	CH-505	- ditto -
	Maximum output	2.5A, 800V
IP receiver	CH-7801	made by CHIBA Electronics Laboratory
	CH-7802	- ditto -



Generator	Model 421	made by Geotronics, USA
		Maximum output 3 kw, 400 Hz, 115 V
IP checker	YN-502	made by YOKOHAMA Electronics
		Laboratory
Transceiver	ICB-350 (500 mw)	6 pcs
	ICB-650 (500 mw)	8 pcs
	National (500 mw)	4 pcs

### 3-1-3 Line survey

Considering the geological structure around Perau mine, 11 survey lines perpendicularly crossing the Perau ore horizon were established in N60°E–S60°W direction with the line spacing of 300 m, and one tie line diagonally crossing with Line A, B, C and D were set up. A pocket compass and 100 m measuring tape were used for the survey of the lines. Stations were established with horizontal distance of 100 m by open traverse. For the spectral IP conducted on Lines G and K, the communication lines were set 30 m parallel apart from main line. Each station of traverse lines are named as 0, 1, 2, 3, . . . . from the west end of the line in 100 m distance. A bench mark used is at the adit of Perau mine, named G-4 of which elevation is 460.61 m.

### 3-2 Data Processing and Analysis

#### 3-2-1 Outline

##### (1) IP method

IP method is conducted by supplying AC current  $I_{AC}$  into the ground through a pair of current electrodes ( $C_1, C_2$ ) with another potential electrodes ( $P_1, P_2$ ) detecting the potential difference  $V_{AC}$ .

In this case, the apparent resistivity  $\rho_{AC}$  of the ground is calculated by the following equation.

$$\rho_{AC} = K V_{AC} / I_{AC}$$

K is a geometrical factor, and when a electrode distance and a electrode space factor is “a” and “n” respectively, K is as follows.



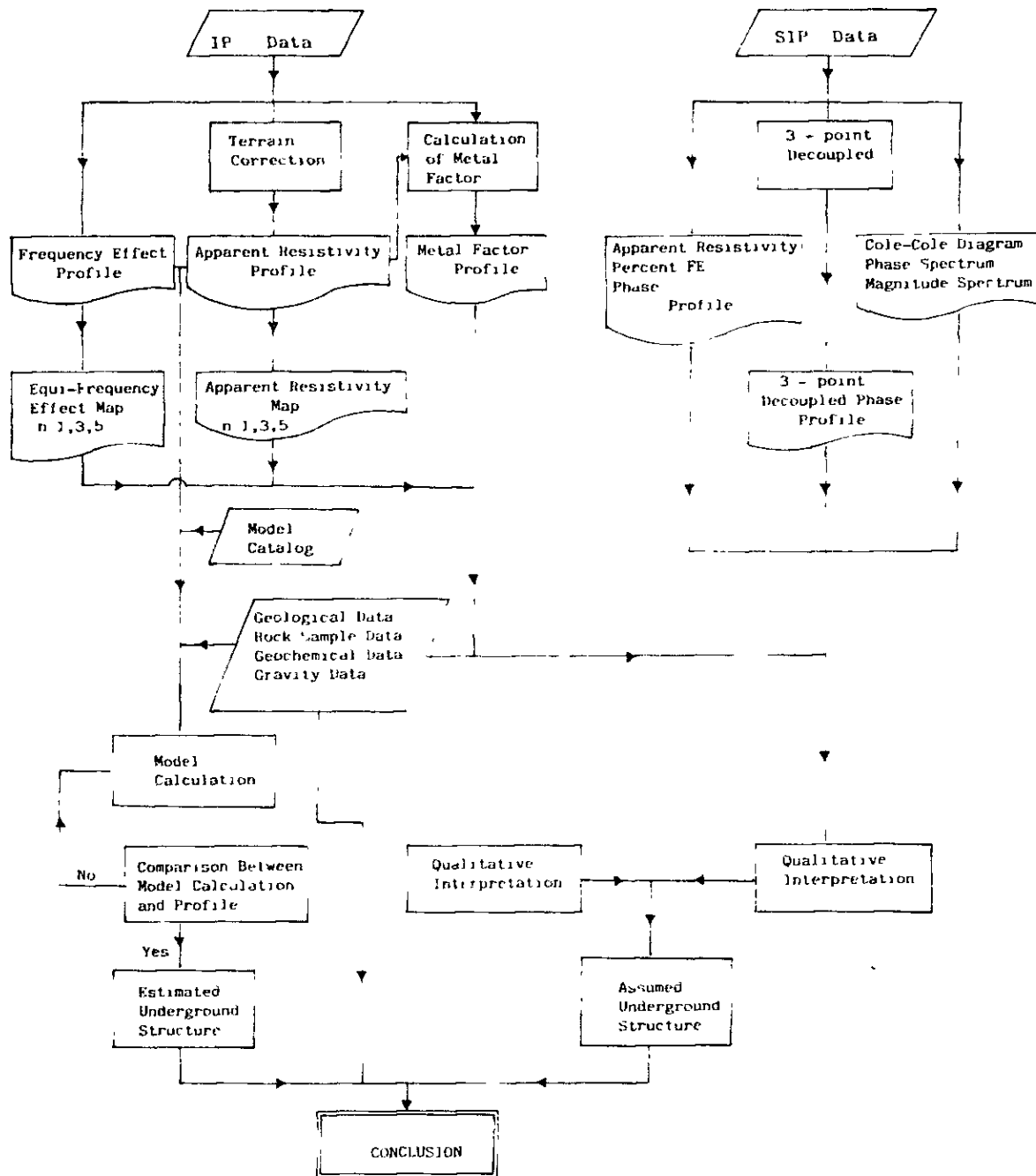


Table II-3-1 List of Survey Lines

Name of Line	Length			Space Factor
	Interval		Length Total	
	a=100M	a=200M		
A	1 0KM	2.5KM	3.5KM	n= 1-5
B	1 1KM	2 5KM	3 6KM	"
C	1 1KM	2 5KM	3.6KM	"
D	1.1KM	2.5KM	3.6KM	"
E	1 0KM	2 5KM	3.5KM	"
F	1.0KM	2 5KM	3.5KM	"
G	1 1KM	2 5KM (2 5KM)	3 6KM	"
H	1 5KM	2 5KM	4.0KM	"
I	1 5KM	2.5KM	4 0KM	"
J		2 5KM	2.5KM	"
K		2 5KM (2 5KM)	2.5KM	"
L		2 7KM	2.7KM	"
TOTAL	10 4KM	30 2KM (5.0KM)	40 6KM	

( ) For Complex Resistivity Survey





Legend

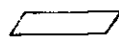
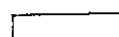
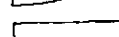
-  Input Data
-  Output Data
-  Process

Fig. II-3-1 Flow Chart of IP and Spectral Data Analysis



$$K = 2\pi / \left( \frac{1}{C_1 P_1} - \frac{1}{C_1 P_2} - \frac{1}{C_2 P_1} + \frac{1}{C_2 P_2} \right)$$

$$= \pi n (n+1) (n+2) a$$

In this survey, "a" are 200 m and partly 100 m and "n" is 1 to 5. The method used in plotting the data is shown in Fig. II-3-2.

After reading the potential difference V, keeping the current at constant, and by lowering the frequency close to DC current, the deviation of the apparent resistivity due to frequency change is directly taken. This deviation is called as the frequency effect (FE) and it is defined by the equation:

$$FE = \frac{V_{DC} - V_{AC}}{V_{AC}} \times 100 (\%) = \frac{\rho_{DC} - \rho_{AC}}{\rho_{AC}} \times 100 (\%)$$

In this survey, the frequencies used are 3.0 and 0.3 Hz.

Metallic mineral causing IP anomaly generally shows low resistivity and high FE, consequently, Metal Conduction Factor (MF) as defined below has been used to emphasize the anomalous zone.

$$MF = FE / \rho \times 1,000 \% / \Omega m$$

The value of apparent resistivity, FE and MF are plotted on the vertex of an equilateral triangle with a line connecting the middle point of dipole-dipole as its hypotenuse. A word of caution, this depth of plotting does not represent the physical property of the depth.

## (2) Terrain Correction

As FE is a ratio of resistivity deviation, it is less affected by topography. But as a geometrical factor K is assumed on the basis of half-infinite plane, the apparent resistivity is affected by the topography depending on the locations of electrodes. That is, resistivity will be detected as high beneath a hill and low beneath a valley.

For the purpose of rejecting the topographic effect quantitatively, a method using a conductive paper was adopted. This method is done by using a conductive sheet of constant resistivity and cutting the paper simulating a scaled topography. A weak current is passed through the simulated topographic section and potentials are measured (Fig. II-3-3).

As this correction is performed on the basis of the two-dimensional half-infinite plain topography, it is impossible to eliminate the effect in case that IP survey lines are parallel to a ridge or a creek. The effect of small topographic changes or the changes of the



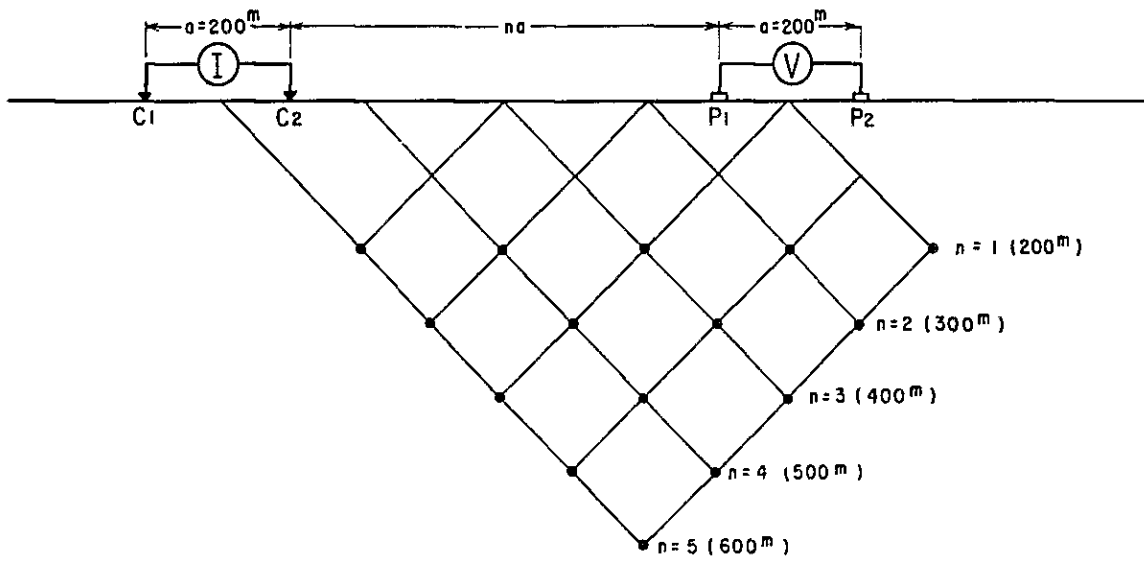


Fig. II-3-2 Plotting Method in IP Pseudo-Section

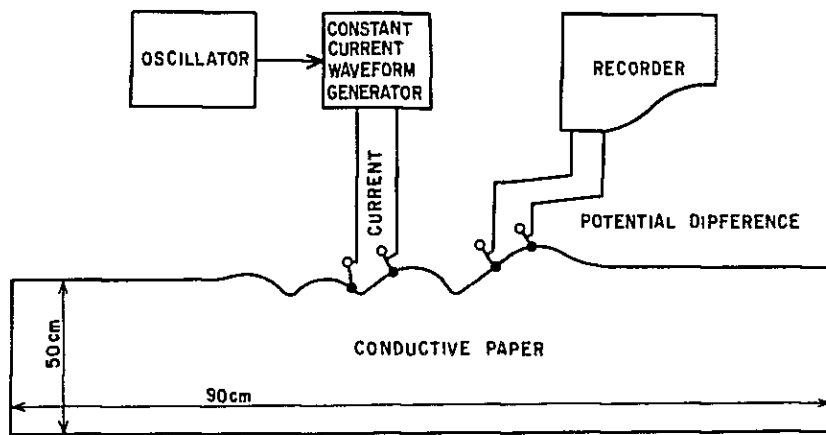


Fig. II-3-3 Block Diagram of Terrain Correction





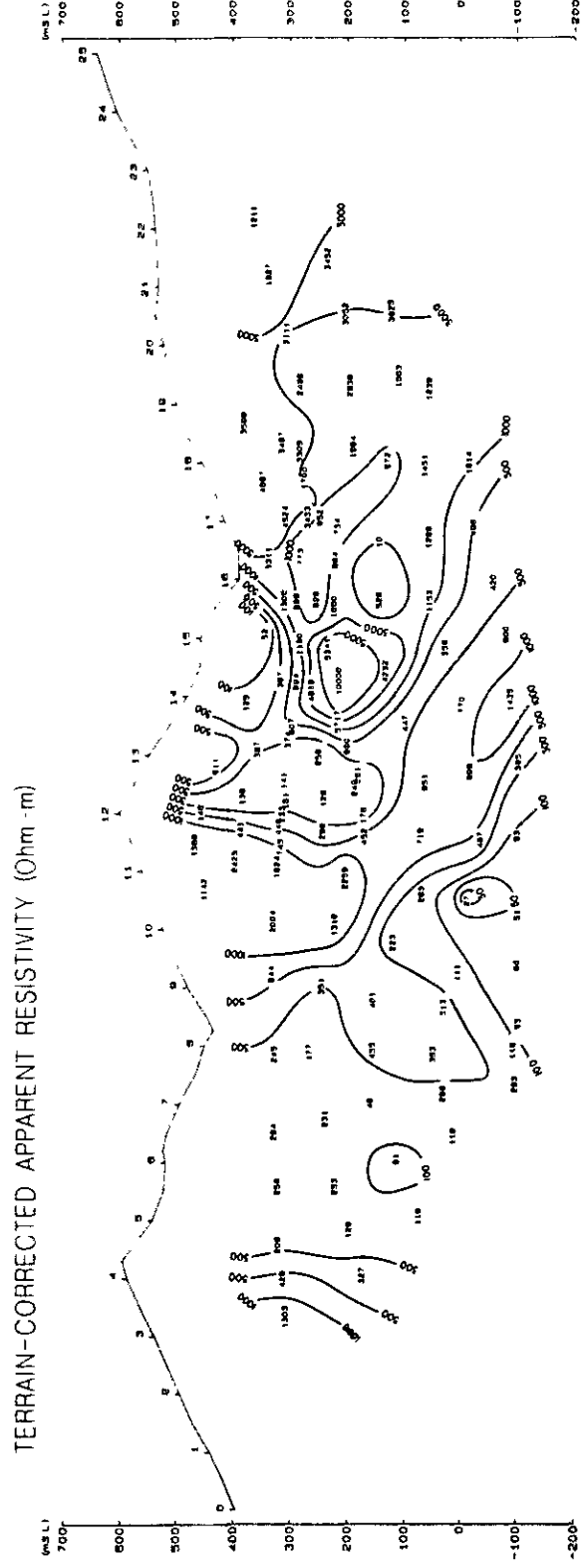
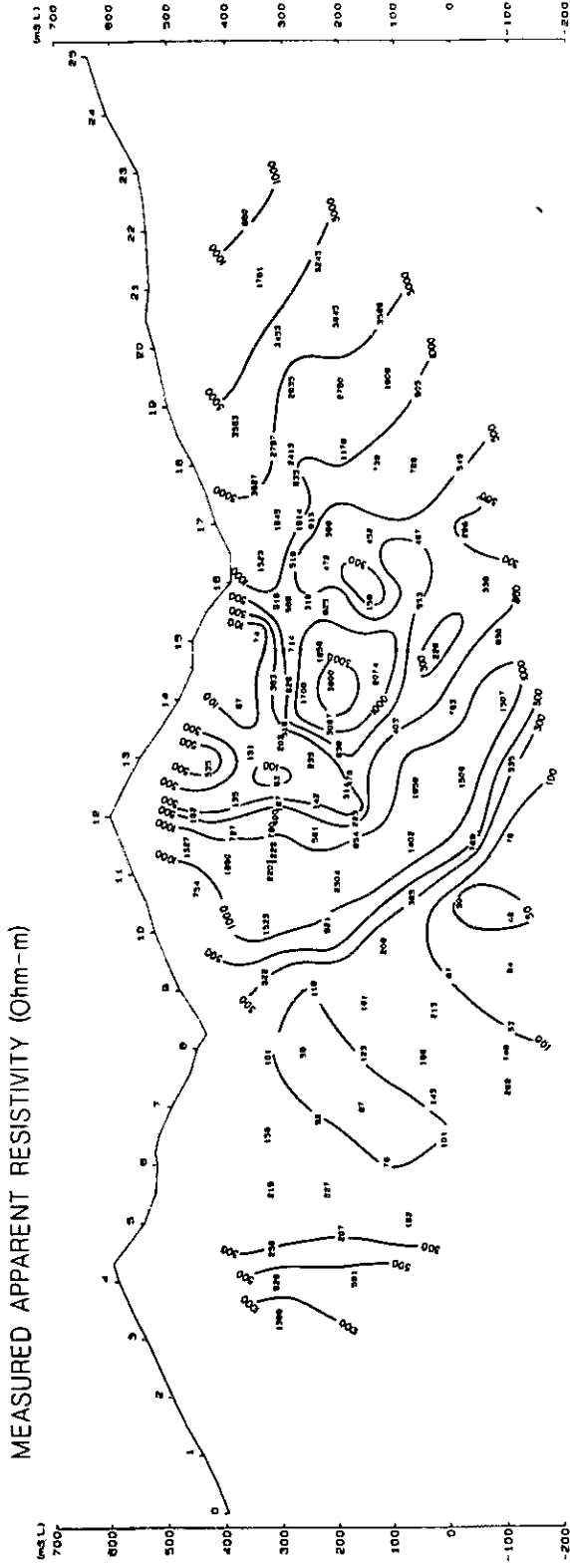


Fig. II-3-4 Example of Terrain Correction



resistivity near the surface can not also be corrected.

In the case of this area where the mountain is perpendicular to the survey line, there is a tendency that the effect of the topography can possibly be eliminated.

As the topography in the survey area is very steep and so rugged, the apparent resistivity is affected by the changes of the topography. Then, two-dimensional terrain correction had to be applied to all IP survey lines.

### 3-2-2 Physical Property Measurements

#### Outline

Physical properties measured at the surface do not necessarily indicate the real properties of rocks, ore deposits, etc., because these are affected by overburden, weathered layer and underground water. Therefore, it is important to know the underground physical properties as close as possible for geophysical exploration. There are two ways to accomplish this purpose, one is an in-situ survey, and the other is the measurement of the physical property of rock samples in the laboratory.

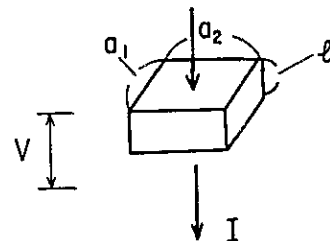
In this survey, the latter method was applied because of inadequate outcrops in the survey area. Thirty comparatively fresh rock samples were collected for the resistivity and FE measurements.

#### The Method of Measurement

In the laboratory, prior to the physical property measurements, the rock samples were cut into rectangular blocks. It is desirable to have the specimens in the same condition as at the time of sampling, so the dried samples were placed in a depressurized water tank to subject all of them to similar conditions before the measurements. The frequency used was 0.3 and 3 Hz.

The resistivity is calculated from the following equation:

$$\rho = \frac{a_1 \times a_2}{\ell} \times \frac{V}{I}$$



Where, \$\ell\$ is the thickness of the sample, \$a\_1\$ and \$a\_2\$ are the length and the width of the sample, \$V\$ is the potential difference and \$I\$ is current.



Table II-3-2 PFE and Resistivity of Rock Samples

Location and Sample No.	PFE (%)	$\rho$ ( $\Omega$ m)	Rock Name
E-21	-10.0	7485	quartzite
F-18	- 4.8	4915	quartzite
F-21	2.9	6844	quartzite
G-18.5	- 8.4	10876	quartzite
G-20.5	- 7.1	6566	quartzite
H-19	1.6	4336	quartzite
H-23	5.9	8459	quartzite
K-12	1.7	17133	quartzite
K-25	1.9	2418	quartzite
I-12.5	5.2	8451	quartz
L-23	7.4	14046	quartz
B-6	3.0	265	amphibole schist
E-6	2.1	1923	amphibole schist
F-13	2.0	1525	amphibole schist
G-3	4.6	862	amphibole schist
L-7	2.4	781	amphibole schist
D-7	0.4	5106	calc-schist
E-12.5	1.5	2136	mica-schist
G-7	11.0	3222	graphite-mica-schist
H-13.2	- 1.6	3693	mica-schist
KG-103	4.0	4573	calc-schist
KG-104	29.3	51	dolerite
C-4	1.4	2225	biotite schist
J-15	0.3	6555	mica-schist
F-16.5	1.2	4600	sericite schist
KG-6	64.8	1982	ore
KG-8	5.8	2543	calc-ore
KG-11	137.8	397	ore
KG-101	144.0	700	ore
KG-102	77.9	726	ore



## Results of Measurements

The results of physical property measurement of 30 samples collected in the field are shown in Table II-3-2. The resistivity of the specimens except the ore samples taken from Perau adit range from 51 to 17,133  $\Omega\text{m}$  and PFE from -10 to 11%. The resistivity of the ore samples range from 397 to 2543  $\Omega\text{m}$  and PFE from 5.8 to 144%.

The samples are divided into four groups, quartz, quartzite, hornblend and schist. The following consideration have been made;

The resistivity of the samples are generally higher than that of the field data. The possible reason for these differences are;

1. Specimens collected represent a small part of the rock mass which generally correspond to a hard compact part of the rocks. Apparent resistivity of the rocks in the field is affected by porous material of low resistivity such as overburden and weathered layers.
2. Silicate rocks (quartzite and quartz vein) have high resistivity while hornblend show low resistivity and mica schist show the middle values. Among the high resistivity rocks, quartzite, K-12, L-23 and G-18.5 show high resistivity of 10,000  $\Omega\text{m}$  with the average of 8321  $\Omega\text{m}$ , which suggest the rocks are compact and homogeneous. Schist show the middle resistivity with an average value of 4269  $\Omega\text{m}$  and also poor conductivity. Average resistivity of low resistivity basic rocks is 1399  $\Omega\text{m}$  and diabase have the lowest values.

In general it was found that there is a correlation of the FE value with the volume content of sulfide. Ore samples taken from Perau adit range from 64.8 to 144% which show the highest of all samples. Among the basic igneous rocks KG-104, B-3 and B-6 with pyrite dissemination show the high FE value of 29%.

Schist with high resistivity have low FE value except L-23 and I-12.5 samples in the quartz vein near Perau mine which show high FE. This FE are assumed to be caused by a small amount of pyrite along the fissures of the specimen.

### 3-2-3 IP Model Simulation

In analyzing the forms and strength of the geophysical anomalies, the results are often checked and compared with the results of the model calculation, and also with the geological structure in order to establish a hypothesis.

From 12 survey lines, 4 lines were selected for quantitative analysis. On Line G and Line K spectral IP was conducted and Line A and Line F were selected as the strong IP





anomalies were detected.

For the calculation, each sections were divided into 1,400 grids and the assumed FE and resistivity values were assigned in each grid. The CDC 6600 was used in the calculation by finite element method. The computer output printed out the assumed model form, FE and resistivity. The comparison between the calculated and actual section, especially, FE was evaluated and various parameters changed in order to approach the observed value. By this procedure it was possible to simulate the tendency and pattern of the actual structures, but they are so complicated and the combination of the geophysical properties that can be assumed are so many that it would be very difficult to conduct an ideal simulation. It was then assumed that the approximate values of the FE and resistivity are close to the observed values. For the calculation it is possible to set an assumption on the nine types of codes, but only six to seven codes were used.

### Results of Model Simulation

Simulation models are shown on Fig. II-4-17~20, which are designed to fit the observed values.

Line A Simulation was made for No.4-No.16. By west dipping (30-40) causative model with FE values of 8-12% and No.11-No.12 as its center. Calculated dipping source is a little steeper than the observed one but general pattern seem to be almost the same.

Line G A model was made at No.14-No.15 as its center where ore horizon of Perau mine is assumed to extend in west dip of about 30 degree.

Line F A general trend fits well with the observed data and a little difference at the depth of No.17-No.19 suggests that causative source may consist of two west dipping anomalies.

Line K Two anomalies are seen on this line. One is a east dipping anomaly at No.7 to No.9 as its center, and the other is a deep source in the eastern side of No.13.

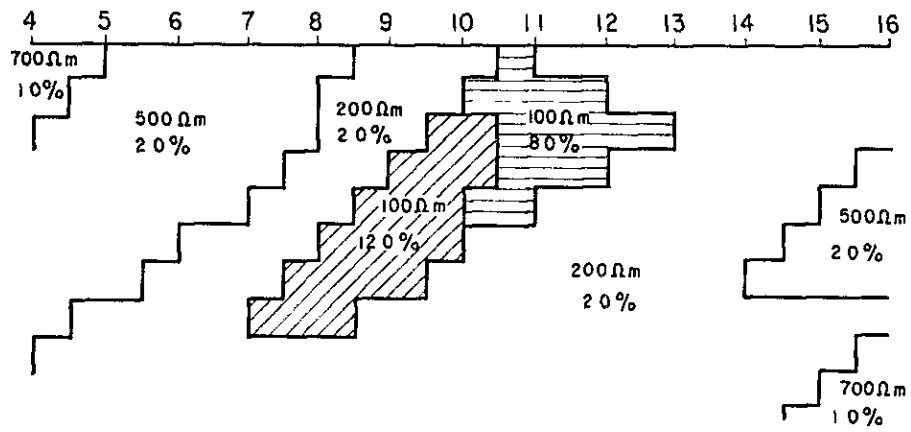
## 3-3 Results of Interpretation

### 3-3-1 Section Analysis

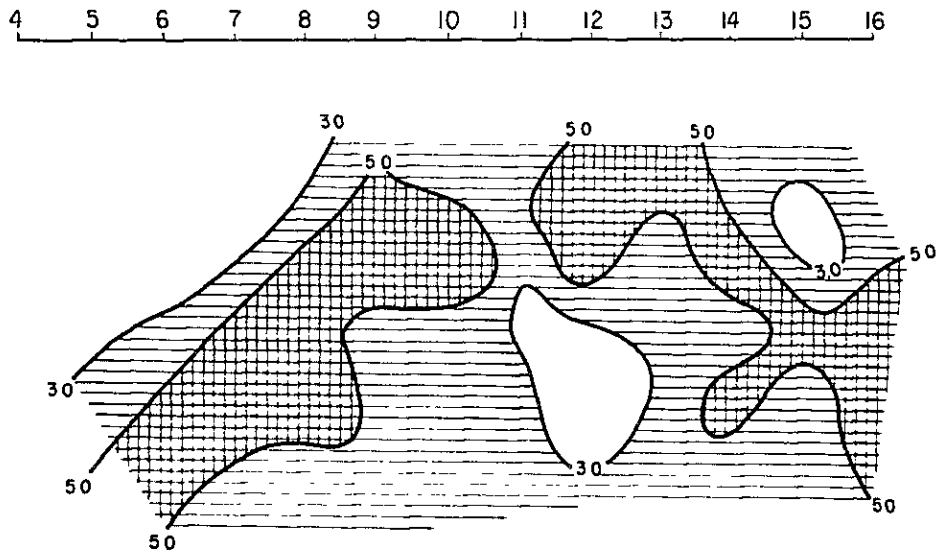
Results of the observation are shown on the profile of the survey line. Frequency effect, apparent resistivity and metal conduction factor are shown on the section. Terrain corrections are conducted on the apparent resistivity. The remarkable anomalies detected in this survey generally show low resistivity and high FE, so that metal conduction factor shows the resemblance closely to the pattern of FE. Any comments on this are omitted unless



Assumed Model



Observed Value



Calculated Value

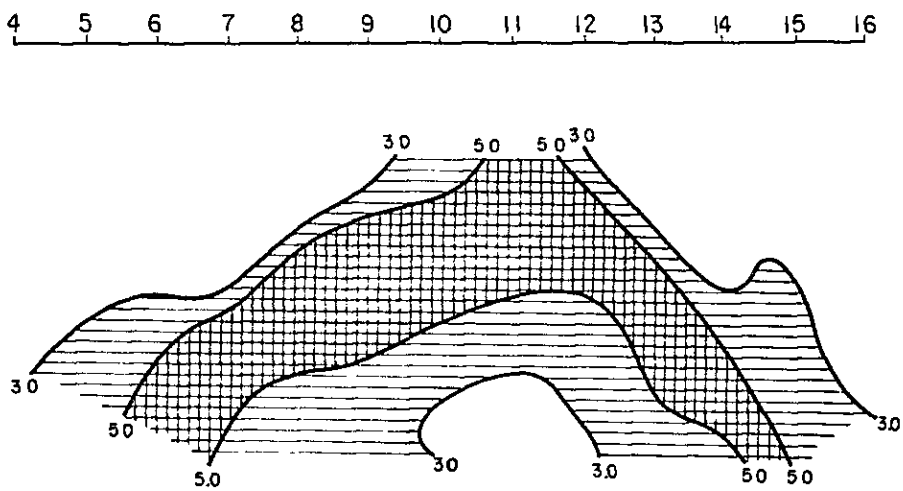
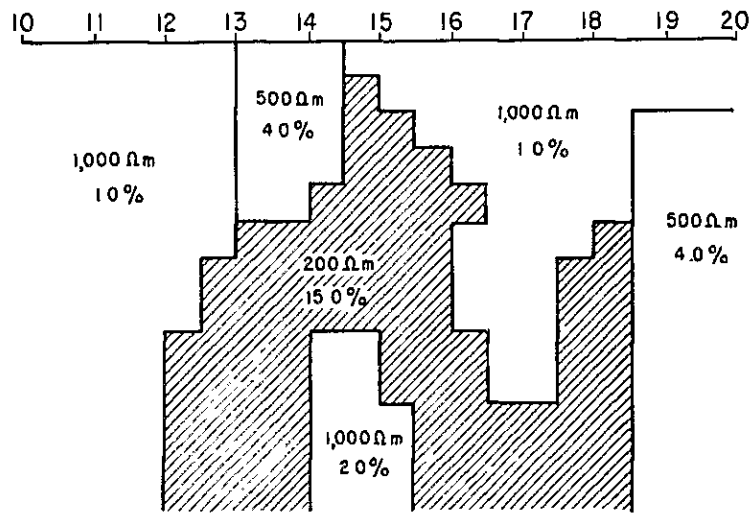


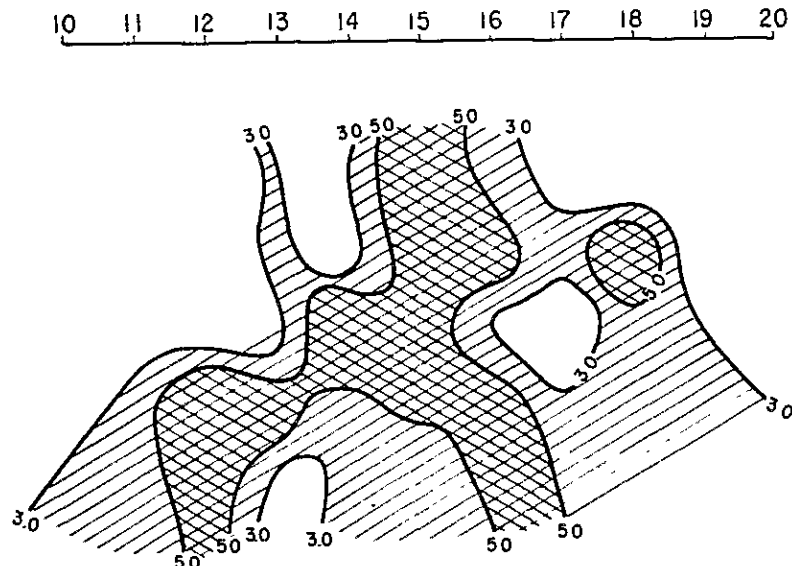
Fig. II-3-17 IP Model Calculation(Line A)



Assumed Model



Observed Value



Calculated Value

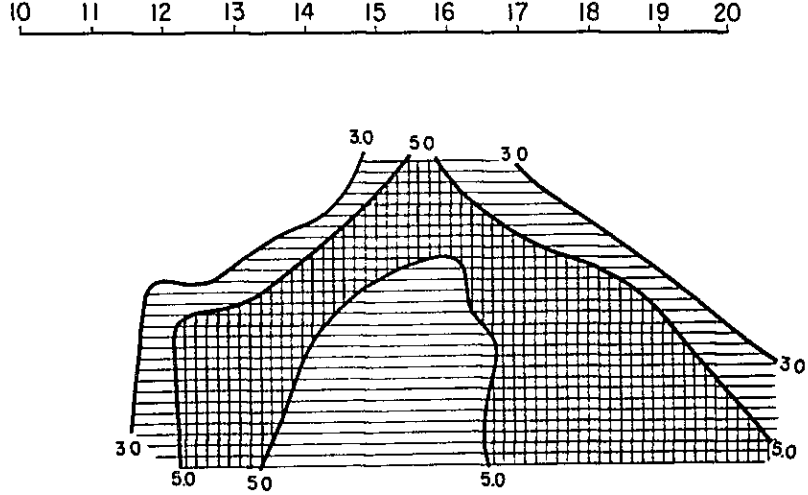
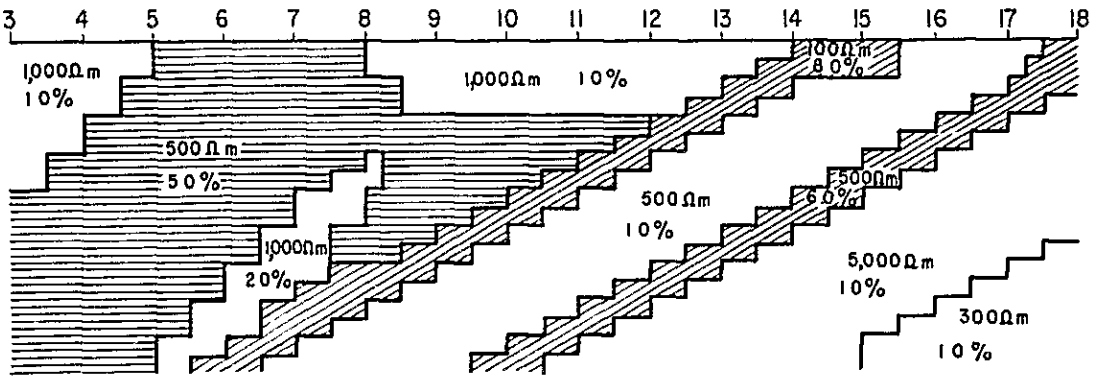


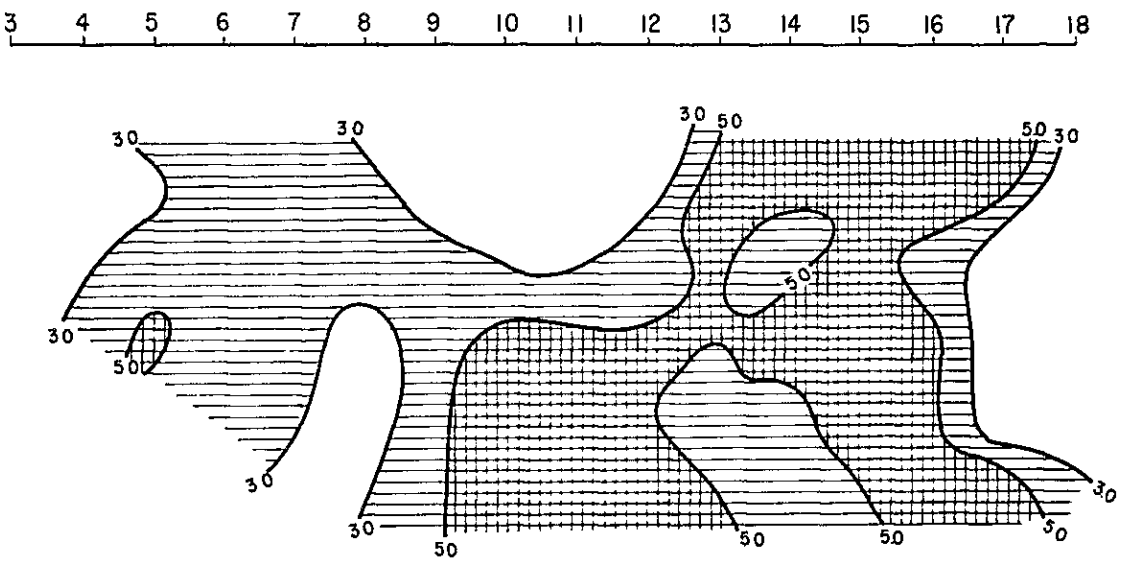
Fig. II-3-18 IP Model Calculation(Line F)



Assumed Model



Observed Value



Calculated Value

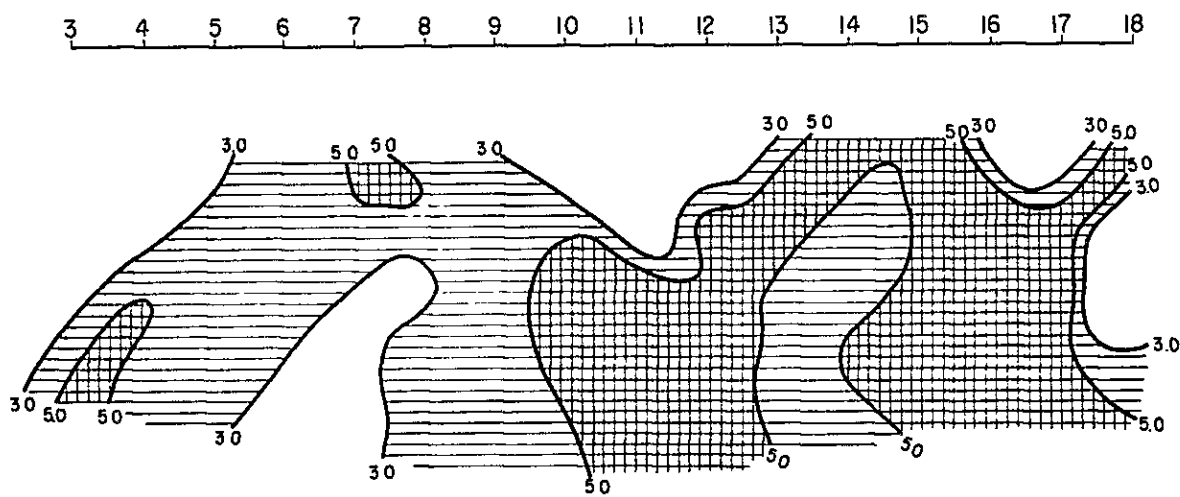
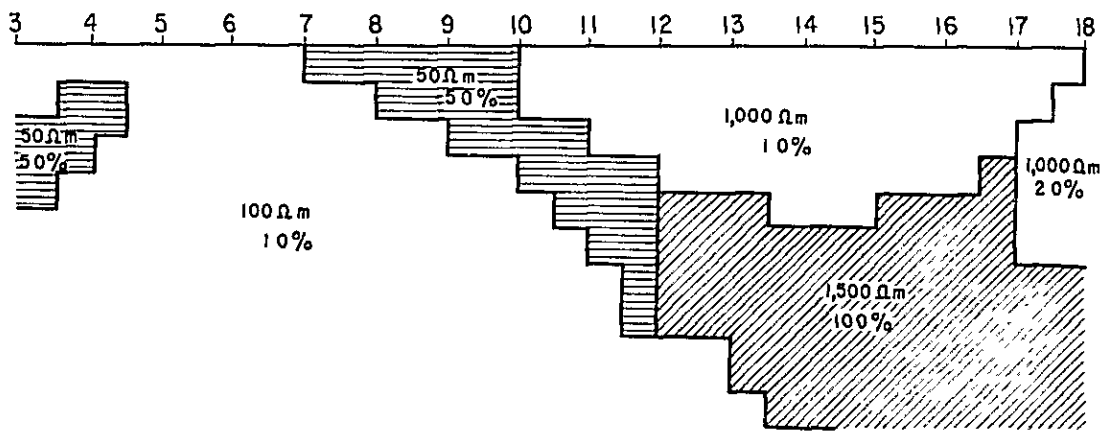


Fig. II-3-19 IP Model Calculation(Line G)

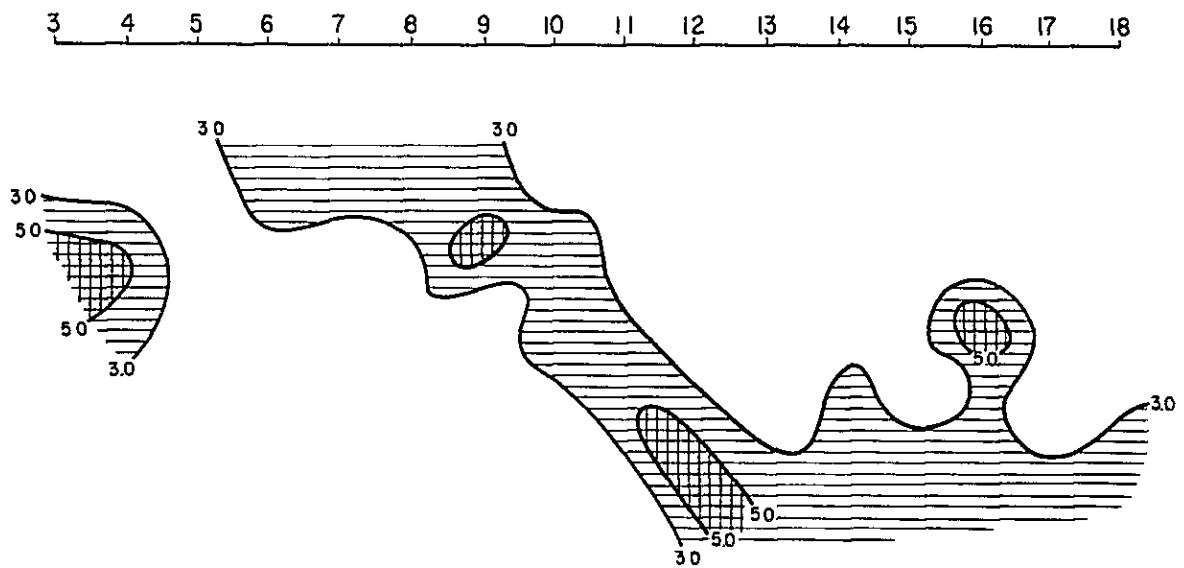




Assumed Model



Observed Value



Calculated Value

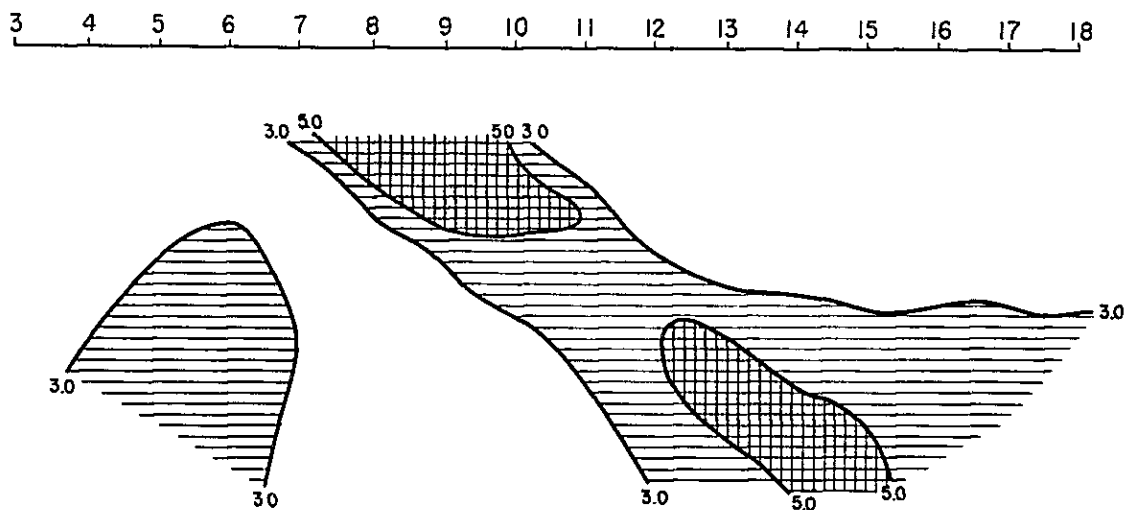


Fig. II-3-20 IP Model Calculation(Line K)



deserving special mention. FE values range from 0.1 to 11.6% in this survey and they are regarded as anomaly when they exceed 3%. On the other hand, apparent resistivity are classified roughly into three groups, namely their ranges are;

- Low resistivity : less than 500  $\Omega\text{m}$
- Middle resistivity . 500  $\Omega\text{m}$  to 1,000  $\Omega\text{m}$
- High resistivity . more than 1,000  $\Omega\text{m}$

#### Line A

In the middle of the line around No.8 to No.13 pants leg shaped low resistivity and high FE anomalies are detected with an eminent FE anomaly of 10.8%. The pattern of this anomaly suggests that the big scale of source exist from the surface of No.8 to No.13 to the depths. In this anomaly FE over 5% may be caused by flat or west dipping causative source from the shallow part of No.11 to No.13 to the depths. Resistivity are generally low as less than 1,000  $\Omega\text{m}$  over the line. Low resistivity less than 300  $\Omega\text{m}$  correspond with FE anomaly especially low resistivity less than 100  $\Omega\text{m}$  are seen from the surface of No.10 to No.13 to the depth.

#### Line B

A weak anomaly is detected in the west of No.14, in the depth of No.14 to No.20 and in the east of No.21. In the anomalous zone in the west of No.14, weak FE anomaly of 3 to 5% partly accompanied with background value near the surface are distributed. Although intermittently east dipping FE anomalies over 5% are detected from the surface of No.5 to the depth of No.10. The former weak anomaly seems to be due to the same source as the one detected on Line A and the source are assumed to be located in the west of No.3. The later are inferred to be due to the east dipping source from the surface of around No.6 to No.8 and the west dipping weak source from the surface of around No.12 to No.14 to the depths, respectively. Apparent resistivity range from 6 to 7,708  $\Omega\text{m}$  and the high resistivity more than 1,000  $\Omega\text{m}$  are seen in the shallow depth of No.12 to No.14 and the east of No.14. Low to middle resistivity less than 1,000  $\Omega\text{m}$  are widely observed in the whole area west of No.14 and the shallow part of No.14 to No.21. Eminent low resistivity (less than 100  $\Omega\text{m}$ ) are seen in the west of No.6 and shallow part around No.9 to No.12. Low resistivity detected in the west of No.6 may at the shallow part around No.9 to No.12. Low resistivity dipping anomaly of less than 100  $\Omega\text{m}$  from the surface of No.10 to No.13. As for the west dipping low resistivity anomaly found around No.9 to No.12 on Line A, no correlations are found with the adjoining lines so that this anomaly may be due to the locally small conductive



source.

#### Line C

Small scale anomalies are detected in the both ends of the line and in the depth of No.15 to No.19. An east dipping anomaly detected in the west end around No.5 to No.7 is a part of a pants leg shaped anomaly and the causative source is considered to locate in the shallow part west of No.4. Anomalies extending from the shallow part of No.9 and No.11 to the depths suggest the west dipping weak source, which may cause the anomalies detected in the east of No.10. As the anomalies detected in the depth of No.15 to No.19 and in the east of No.22 are weak and vague, it is difficult to assume the shape of the source. High resistivity zone more than 1,000  $\Omega\text{m}$  show east dipping form the surface of No.3 to No.7, expanding dominantly towards east of No.22 to the depths.

#### Line D

No remarkable anomalies are observed in this line except weak local anomalies of 3 to 4% near No.19 to No.22, in depth of No.11 and No.12 and in the shallows of No.14. Those anomalies are too weak to assume the location of the source, but the weak west dipping anomaly seen around No.19 to No.22 may be due to the west dipping source from the surface No.21 to the depths. High resistivity values more than 1,000  $\Omega\text{m}$  are locally detected in the depth of No.7 to No 18 and in the west of No.7. On the other hand, low resistivity less than 500  $\Omega\text{m}$  are detected near the surface west of No 17 and in the east of No.18. Low to middle resistivity are generally dominant compared with Line C.

#### Line E

Weak anomaly over 3% are detected in No.4 to No.8, in the depth of No.13 to No.17 and No.18 to No.20, from which the shape of the source can not be determined. Low resistivity less than 500  $\Omega\text{m}$  are recognized in the near surface of No.11 to No.16 and in the east of No.18 where FE anomalies are detected.

#### Line F

FE anomalies with a maximum value of 12.5% are observed in No.15 to No.17 as its center. Judging from their pattern west dipping source from the surface of No.16 to the depth and flat source in the depth of No.15 are assumed. This anomalous zone are believed to be formed by the combination of those sources. Corresponding with FE anomalies the same pattern of comparatively low resistivity of less than 1,000  $\Omega\text{m}$  are observed, reflecting a big contrast of geological change with the high resistivity of more than 1,000  $\Omega\text{m}$  in both sides.



#### Line G

Wide spread of anomalies are seen in No.5 to No.19, which is divided into three groups judging from the shape of FE anomaly.

- (1) FE anomaly of 3 to 5% seen in No.5 to No.8 with No.7 as its center
- (2) FE anomalies of more than 7% with No.16 as its center
- (3) Anomalies in No.16 to No 19

- (1) Comparatively wide anomaly tend to continue to the depths dipping west and it suggests that west dipping causative source exists from the surface to the depth.
- (2) Strong west dipping source is assumed to extend from the surface to the depths.
- (3) This anomaly shows the same FE anomaly pattern as (1), indicating the west dipping anomaly from the surface to the depth. As mentioned above, west dipping shape of anomaly is similar for three anomalies, but the causative anomaly is considered to be different for each case.

#### Line H

Remarkable anomalies with a maximum FE of 11.2% are recognized in the area of No.4 to No.8. This anomalous zone may be separated into two groups,

- (1) 3 to 5% anomaly detected in No.4 to No 11 seem to be separated into two areas, No 4 to No.8 and No.10 to No 11. The former is a west dipping source from the surface of No.7 to the depths, while the latter is a shallow source of No.11 to No.13.
- (2) East dipping anomaly observed from the surface of No.11 to No.18 is supposed to be due to east dipping source extending from the surface of No.11 to No 13 and a shallow flat and west dipping source in No.14 and No.15.

In the FE anomalies zone of (1) and (2) mentioned above, low to middle resistivity of less than 1,000  $\Omega\text{m}$  are detected showing the same pattern with FE anomalies. Particularly in the FE anomalous zone of (1), very low resistivity anomaly including 3  $\Omega\text{m}$  extend to the depths in west dip from the surface to the depth. It is believed that the anomaly (1) and the anomaly detected in No 5 to No.8 of Line G are caused by the same source. Both anomalies are almost the same for the low resistivity less than 500  $\Omega\text{m}$  and the high FE more than 3%, but FE values of line H are generally higher than that of Line G and the resistivity values range from 100 to 300  $\Omega\text{m}$  on Line G, while on Line H very low resistivity of 3  $\Omega\text{m}$  is recorded indicating the shape of west dipping source.

#### Line I

FE anomalies are detected in the west of No.8, No.12 to No.18, in the depth of No.19





to No.22 and in the east of No.23. As the anomaly detected in the west of No.23 appears on the western end of the line, the whole shape of the anomaly is not clear, but this anomalies are considered to be due to the same source which give rise to the anomalies on the west side of Lines G and H. West dipping anomaly detected at No.12 to No.18 is assumed to be due to the west dipping source from the surface of No.12 to No.17 to the depths. The shape of the anomaly distributed in the depths of No.18 to No.22 suggest the west dipping source in the area, however, the anomaly do not extend to the adjoining lines which means that this is a local and small scale anomaly. Obscure pattern of the anomaly detected in the east of No.23 do not enable us to assume the shape of the source.

#### Line J

In the west of No.16, wide and deep anomalies are detected from the surface, however, remarkable FE anomalies are not observed except from the surface to the depth of No.14 and No.15, where slightly east dipping anomalies of more than 5% are recognized. FE anomalous zone corresponds with low to middle resistivity of less than 1,000  $\Omega\text{m}$  and high resistivity are found only in the east of No.16

#### Line K

This line intersects with lines A, B, C and D of NE–SW direction. Some anomalies are confirmed in the west of No.4, in the shallows of No.6 to No.9 and in the depths of No.13 to No.20. The east dipping anomalies detected in the west of No.4 and in the shallow of No.6 to No.9 are assumed to be due to the same causative source. As the source locates in the west end of the line, this source is assumed to be in flat or west dipping. Deep and weak FE anomalies found in the area of No.13 to No.20 are obscure, but probably due to the same source of weak alteration as observed in the east of Lines B, C and D. In the areas of No.11 to No.17 and in the shallows east of No.20 high resistivity values are detected, while the low to medium resistivity values are dominant over this line. Especially from the surface of No.6 and No.7 low resistivity of less than 100  $\Omega\text{m}$  accompanied with FE anomaly are detected as typical MF anomalies.

#### Line L

This tie-line cuts in right angles with Lines A to J and in the both ends of line, west of No.8 and east of No.17, anomalies are confirmed, which correspond with the anomaly detected in other traverse lines. High resistivity more than 1,000  $\Omega\text{m}$  distribute widely, but resistivity less than 1,000  $\Omega\text{m}$  are seen in the west of No.5, in the shallows of No.7 to No.13 and in the depths of No.16 to No.22.

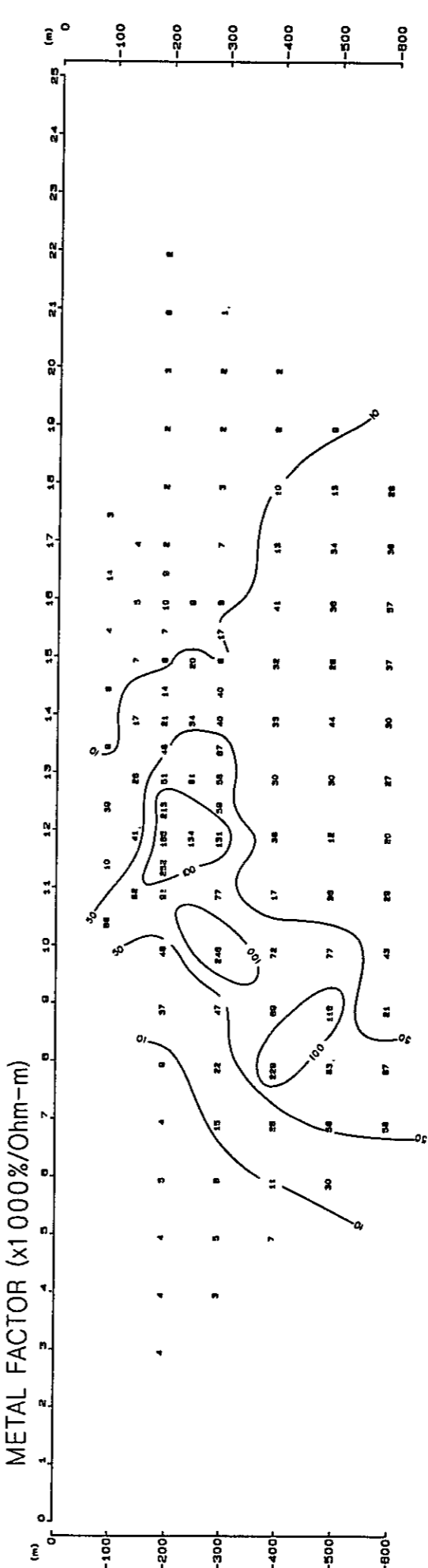
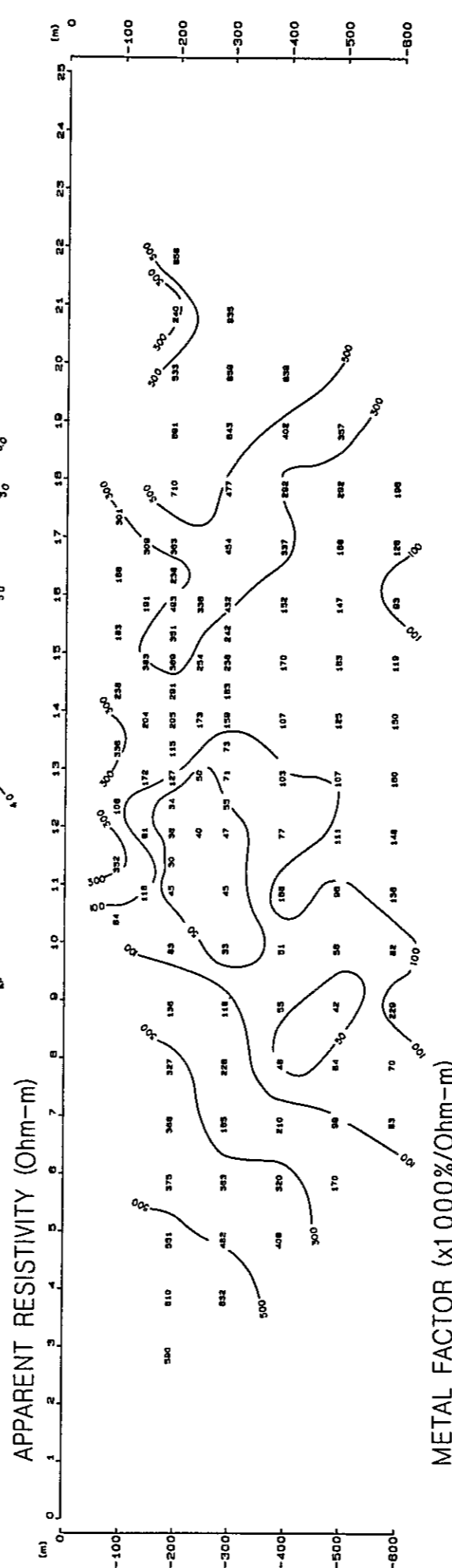
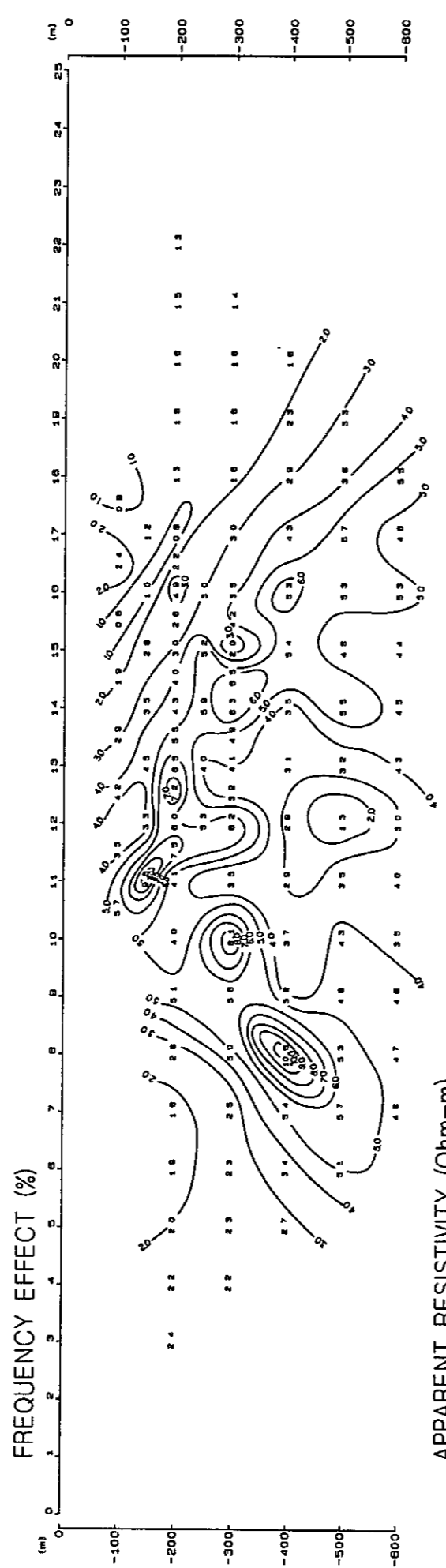
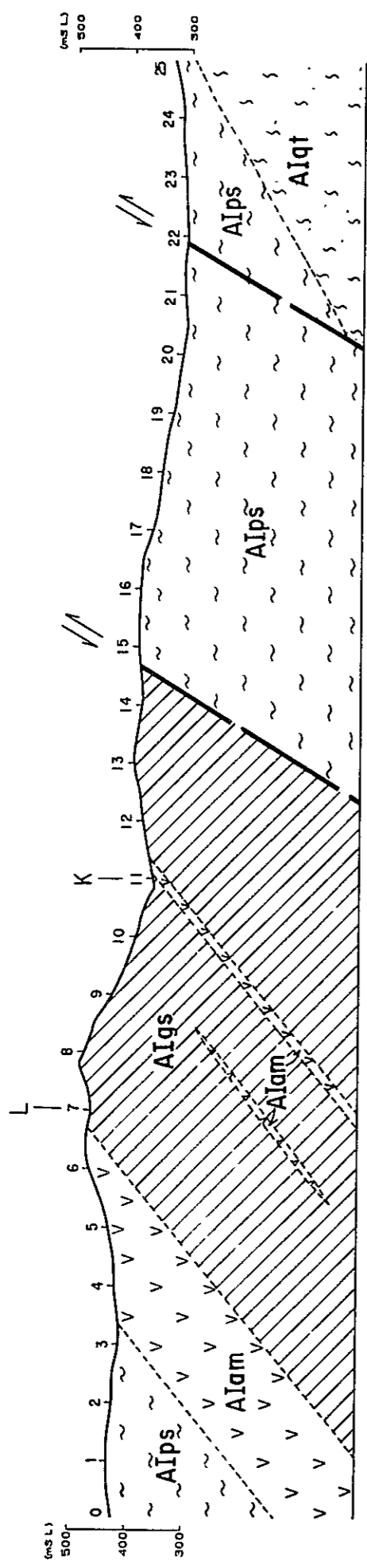


Fig II-3-5 IP Profile (Line A)

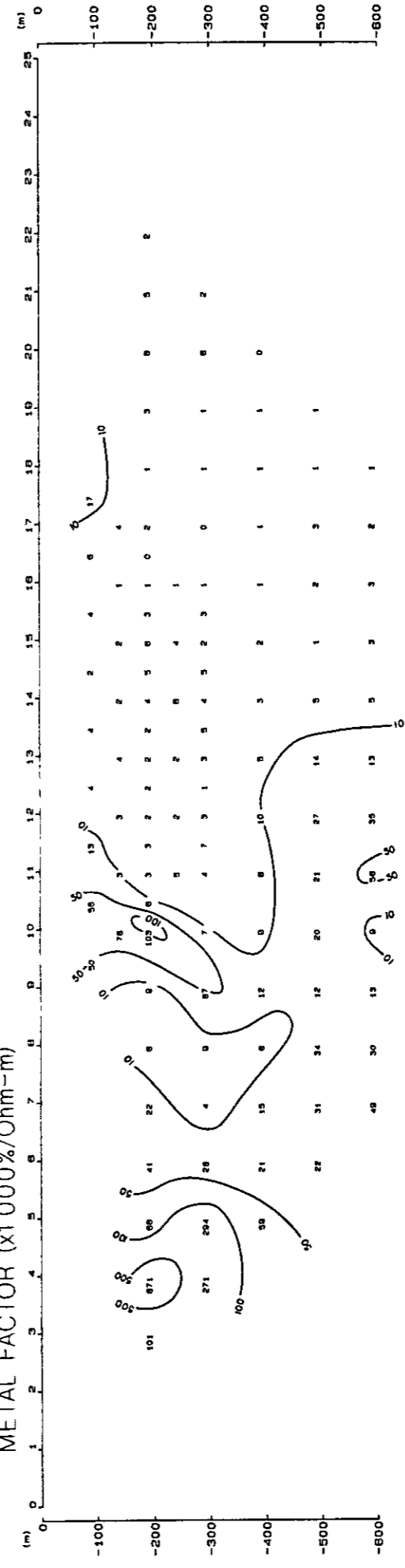
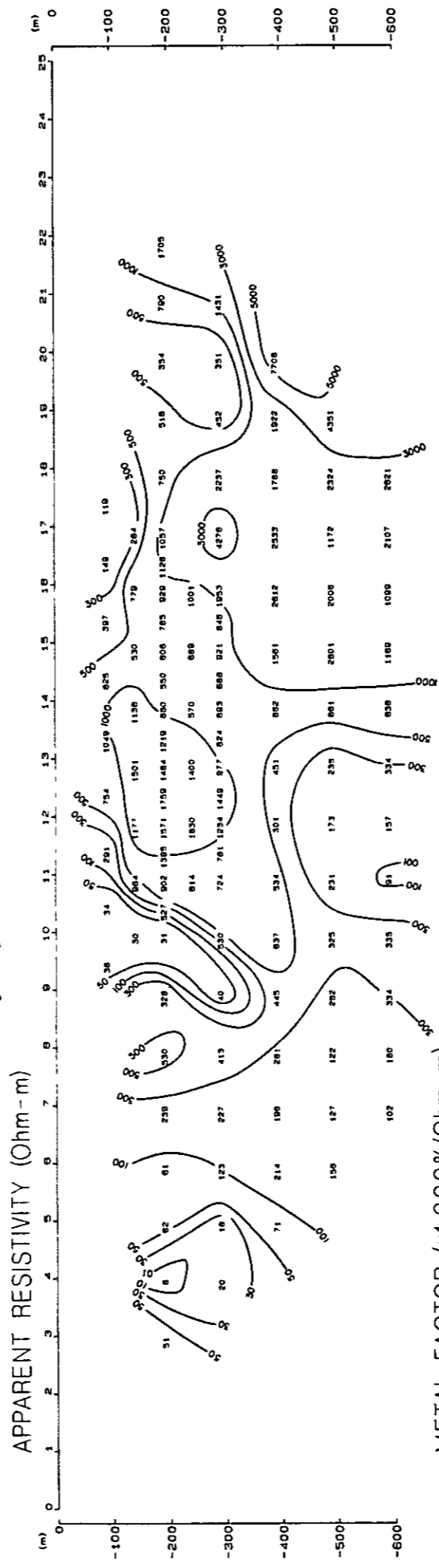
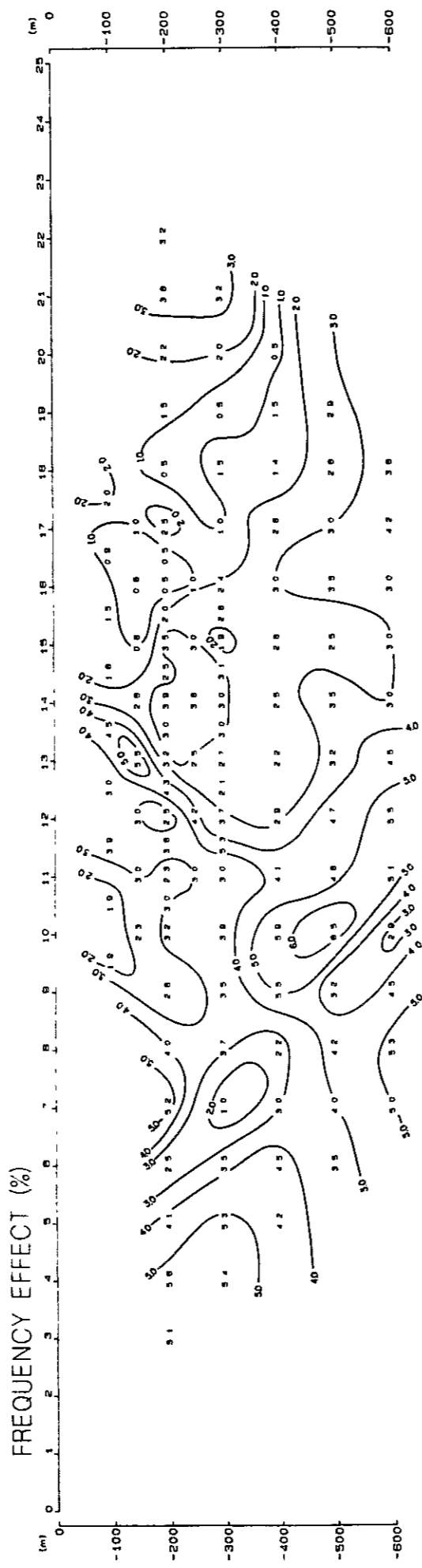
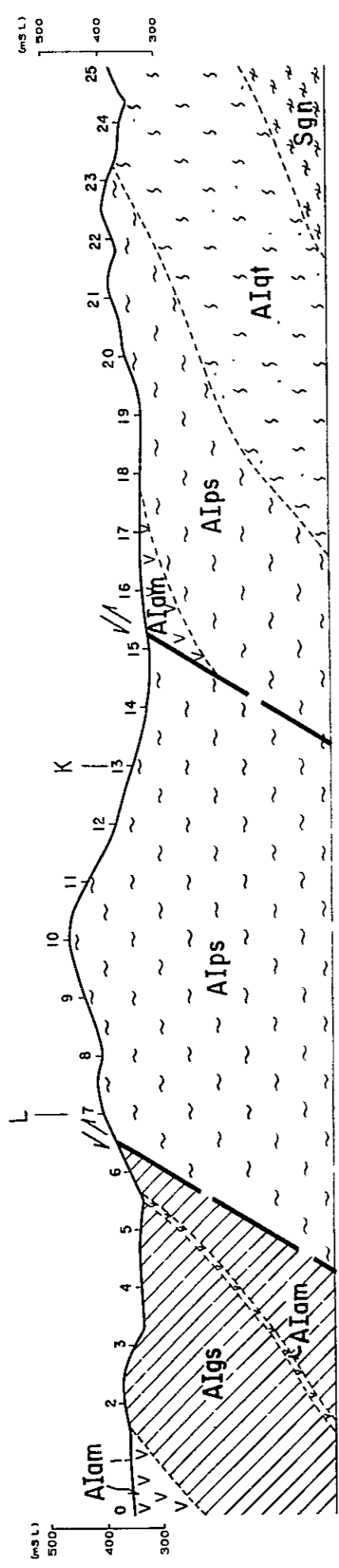


Fig II-3-6 IP Profile (Line B)

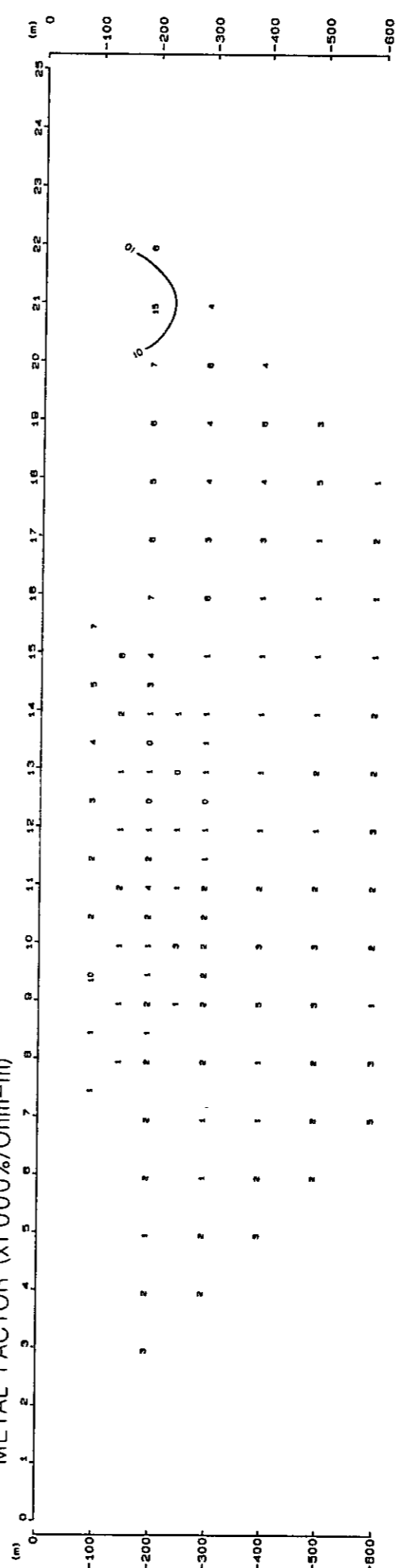
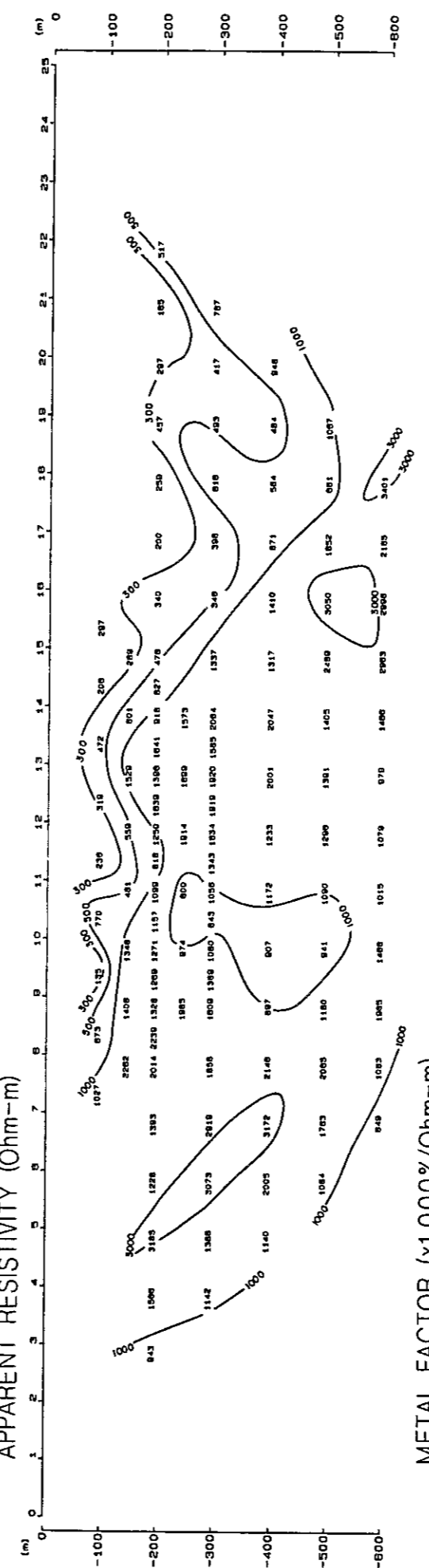
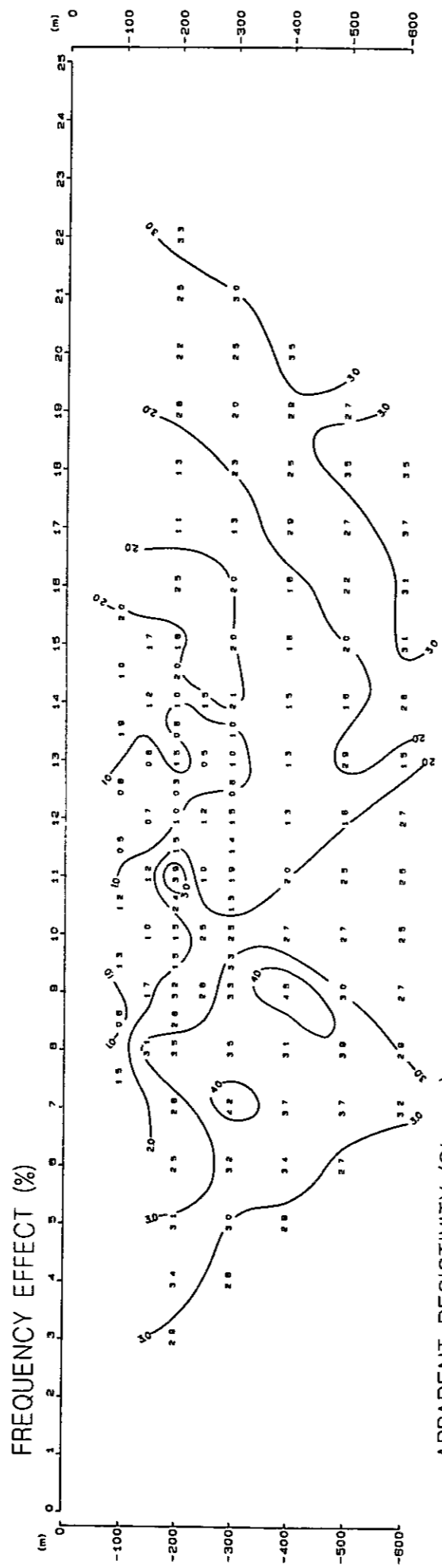
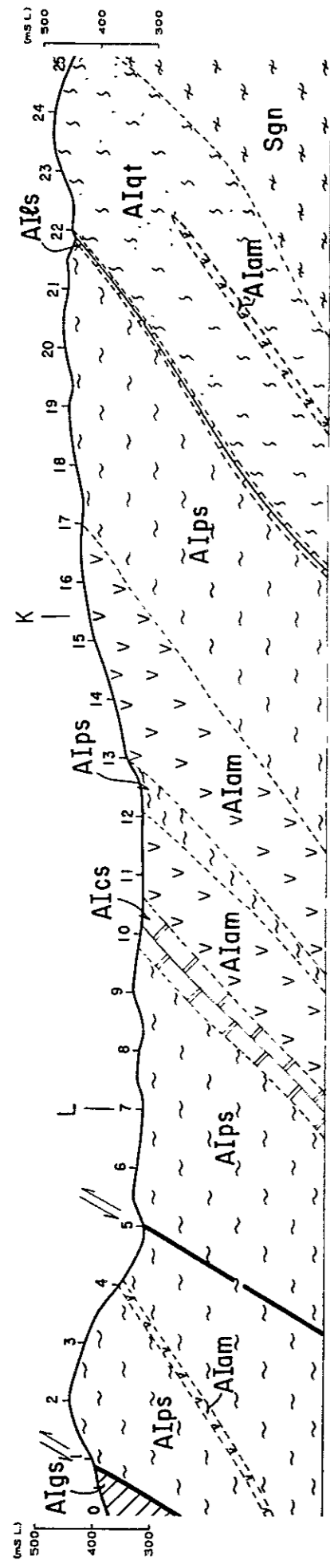


Fig II-3-7 IP Profile (Line C)

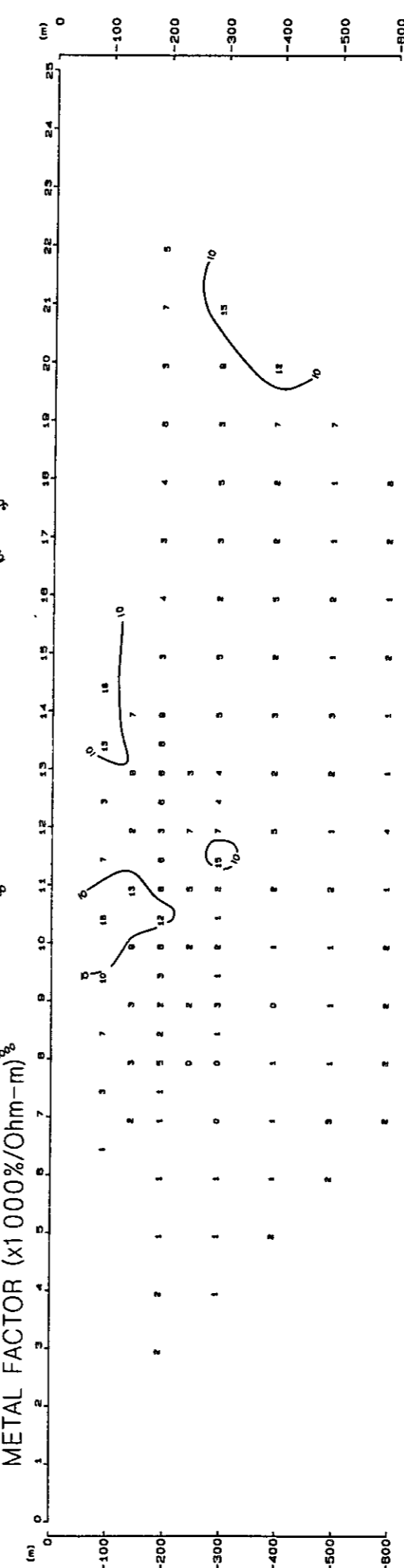
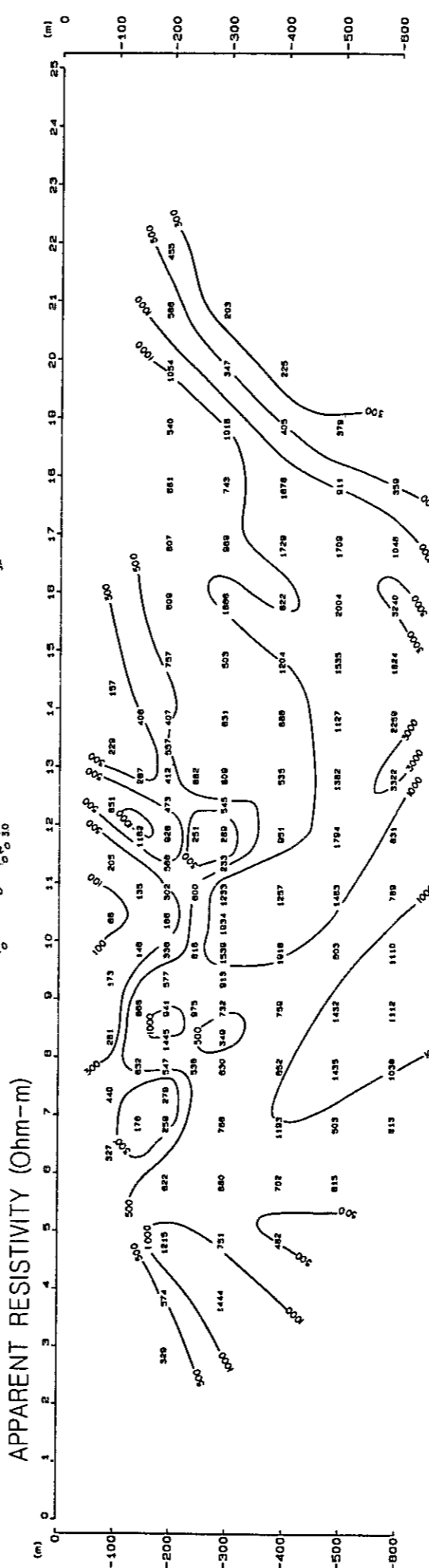
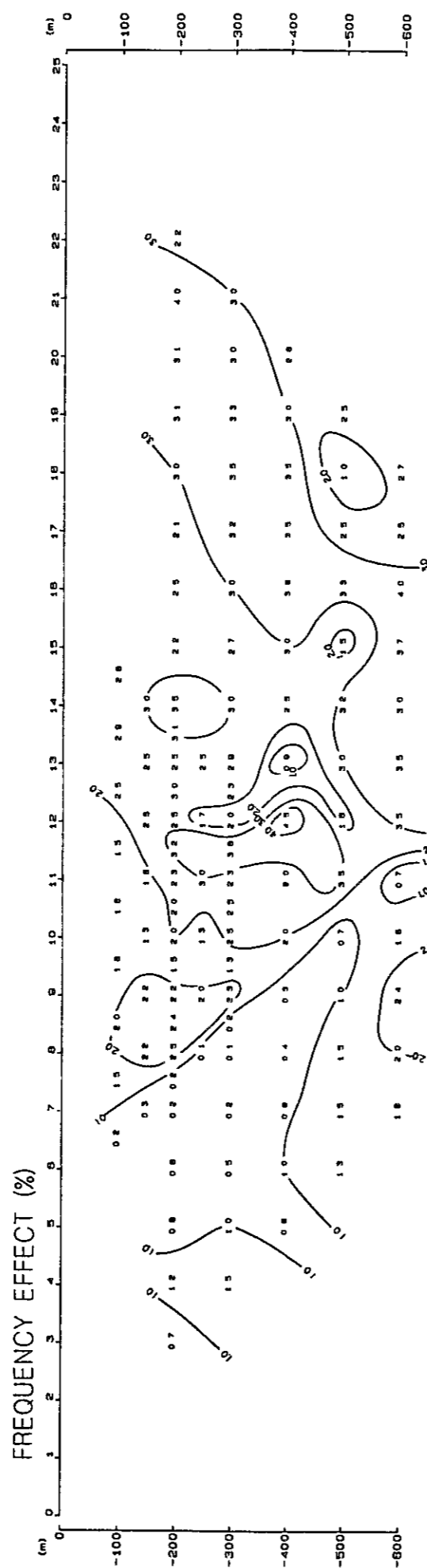
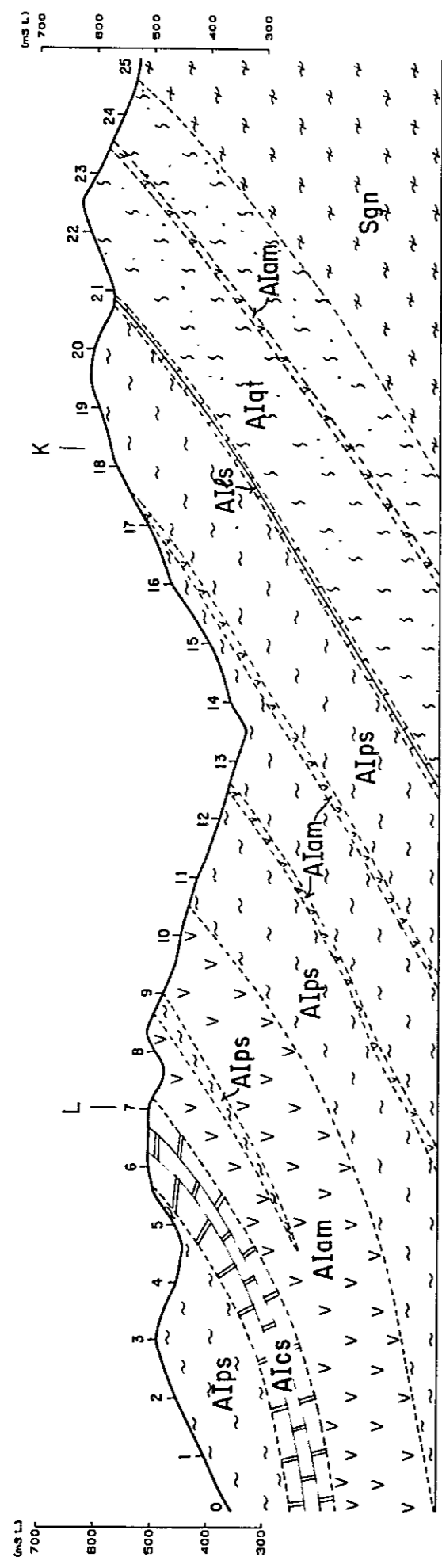


Fig II-3-8 IP Profile (Line D)

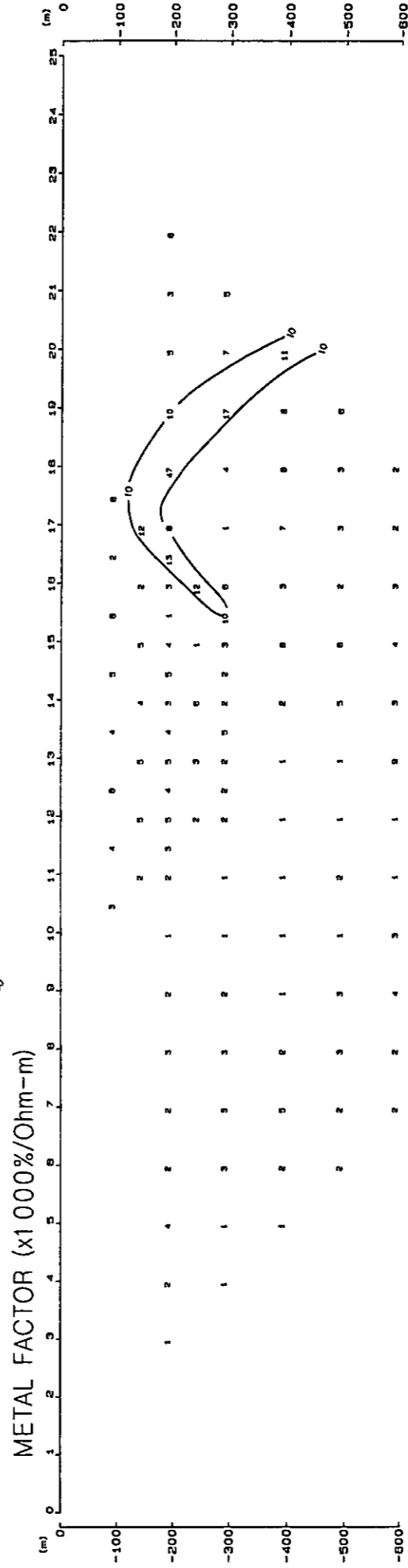
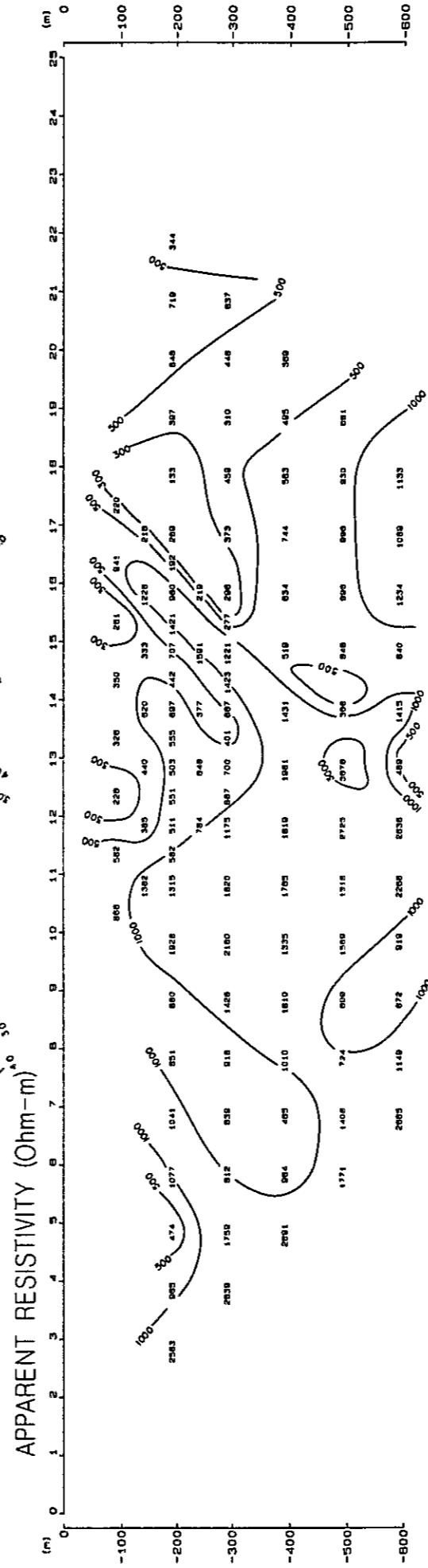
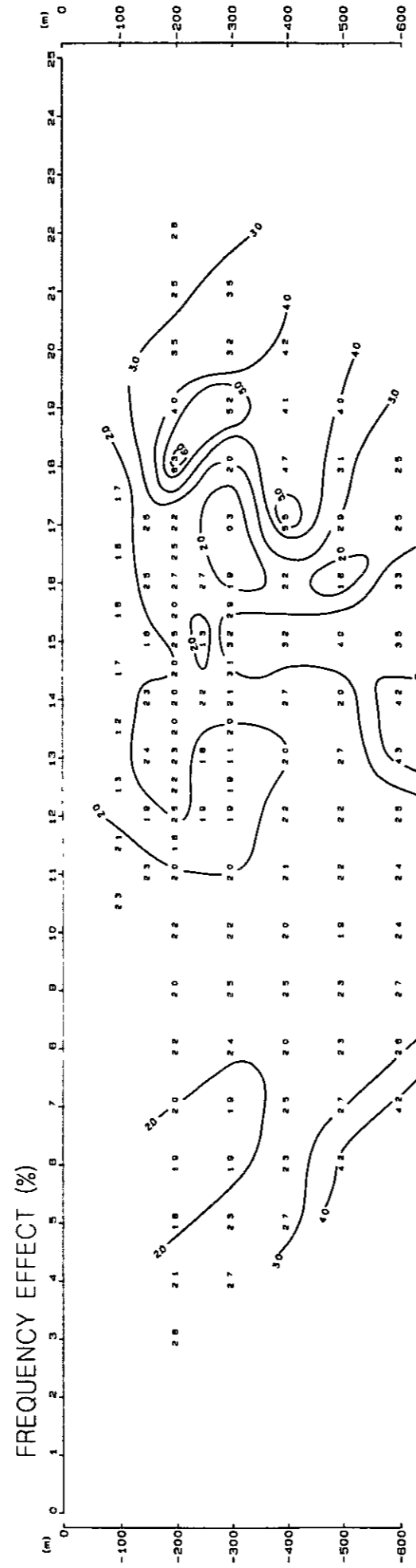
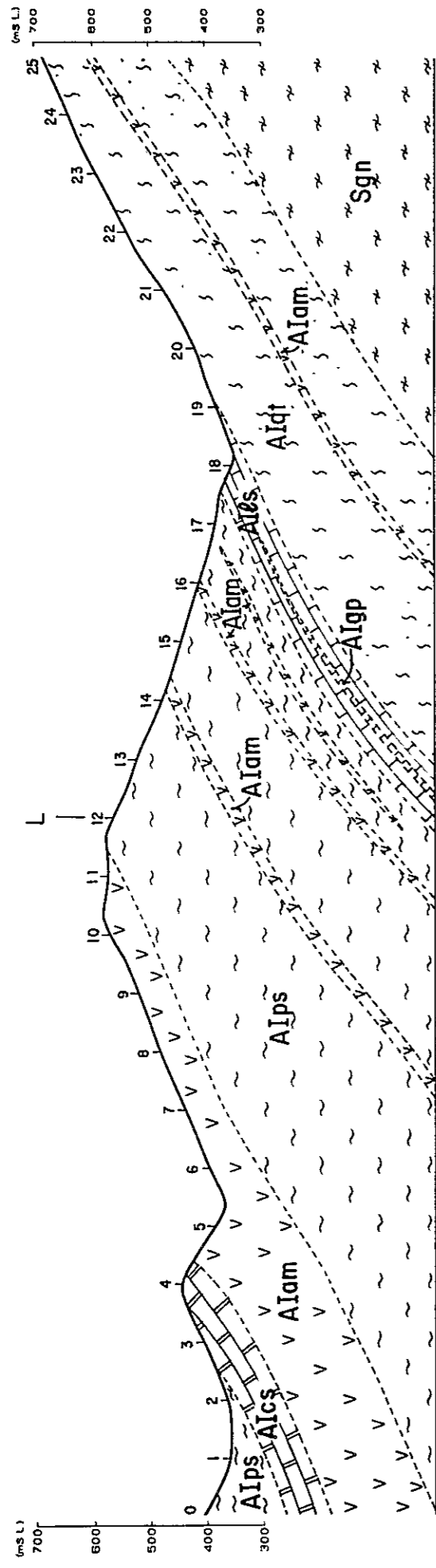


Fig II-3-9 IP Profile (Line E)

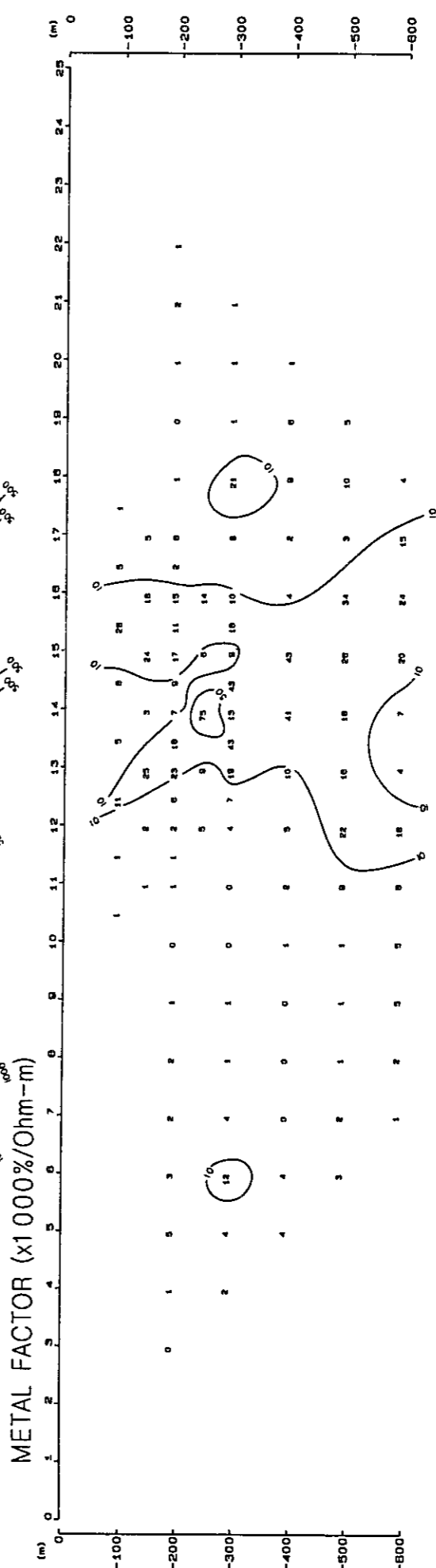
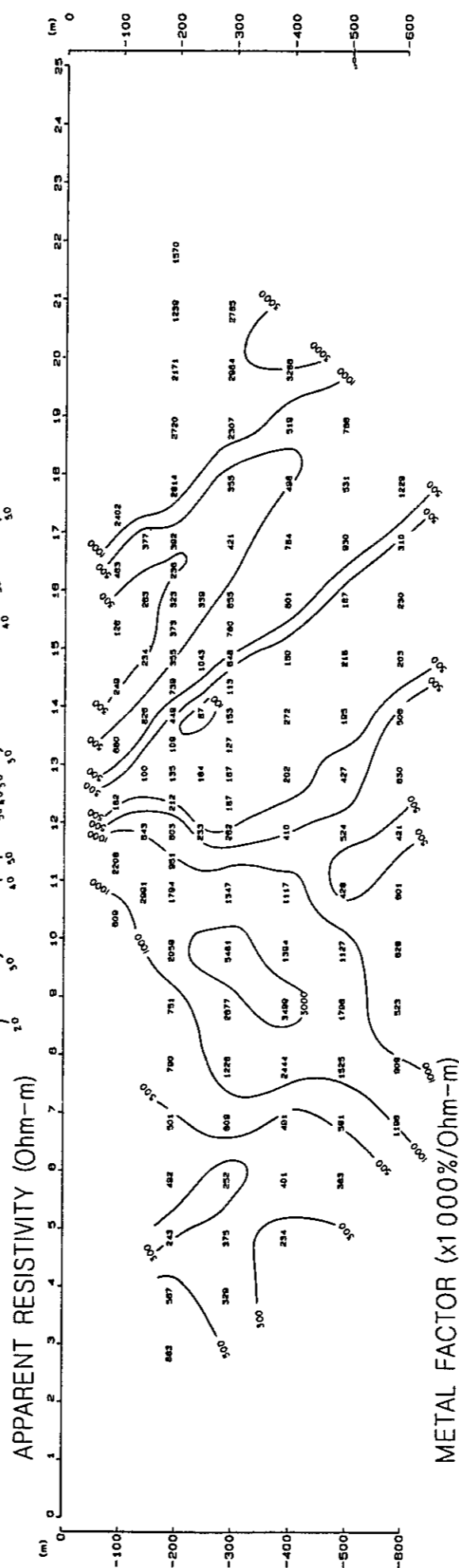
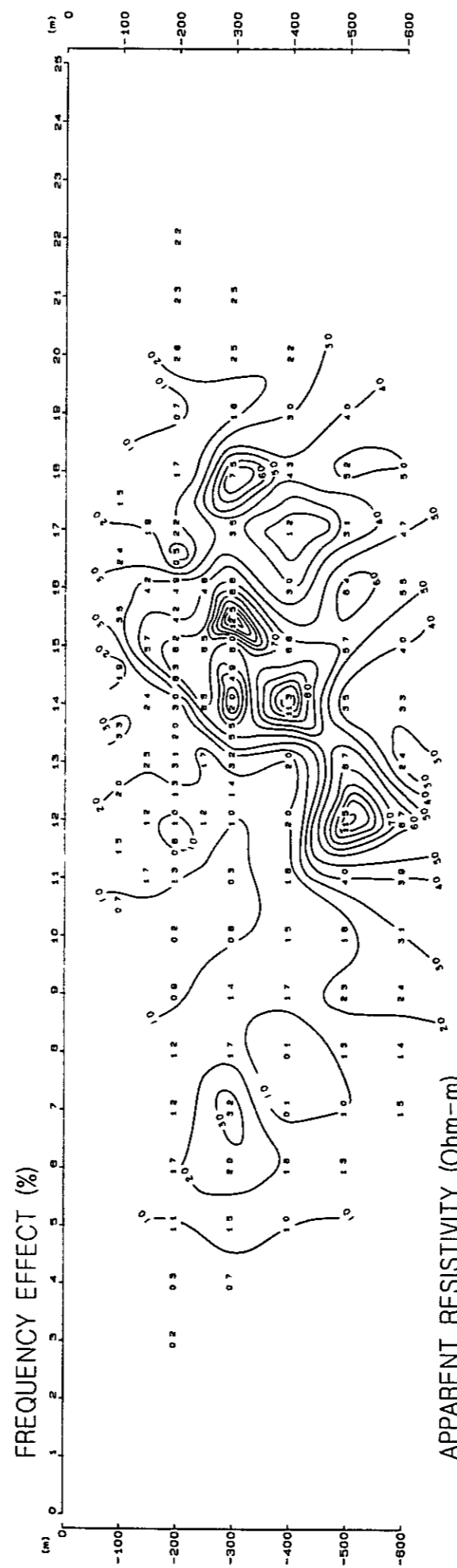
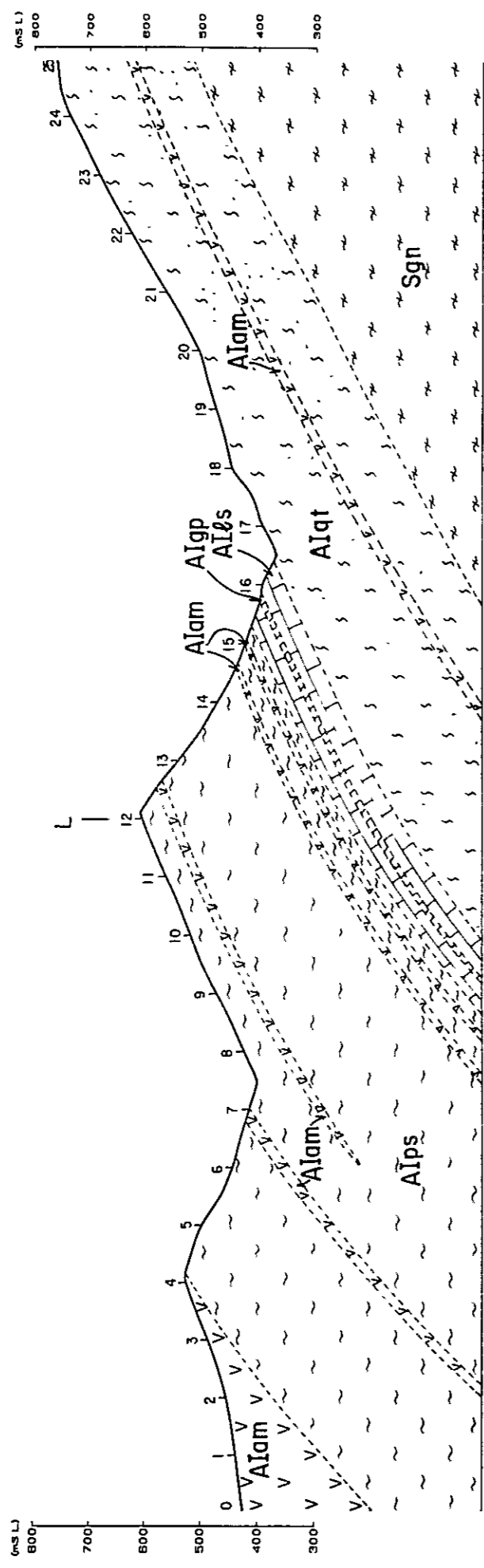


Fig II-3-10 IP Profile (Line F)



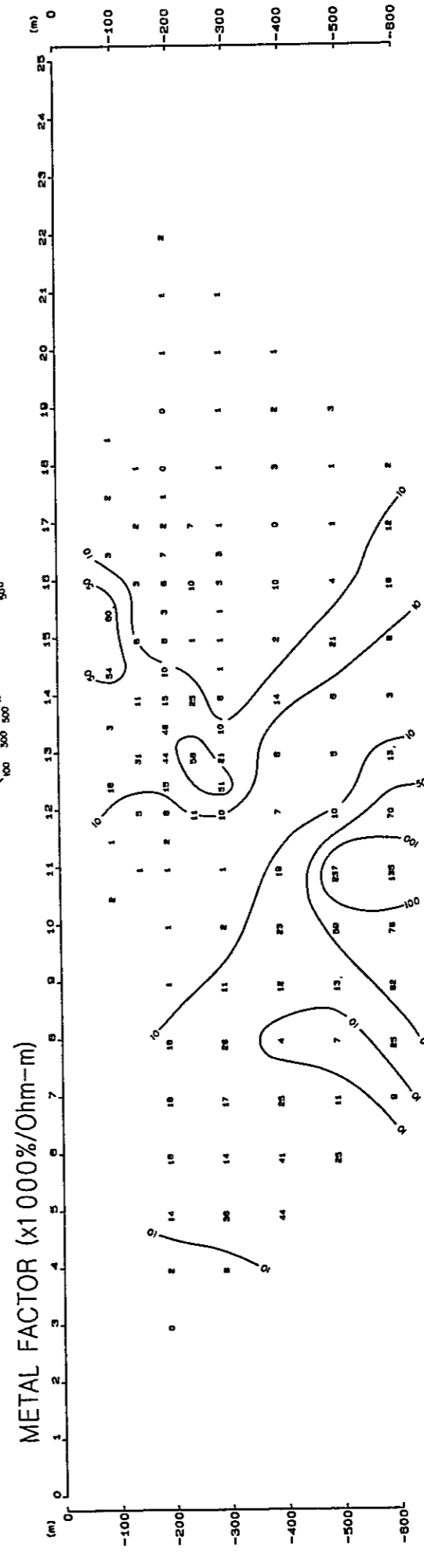
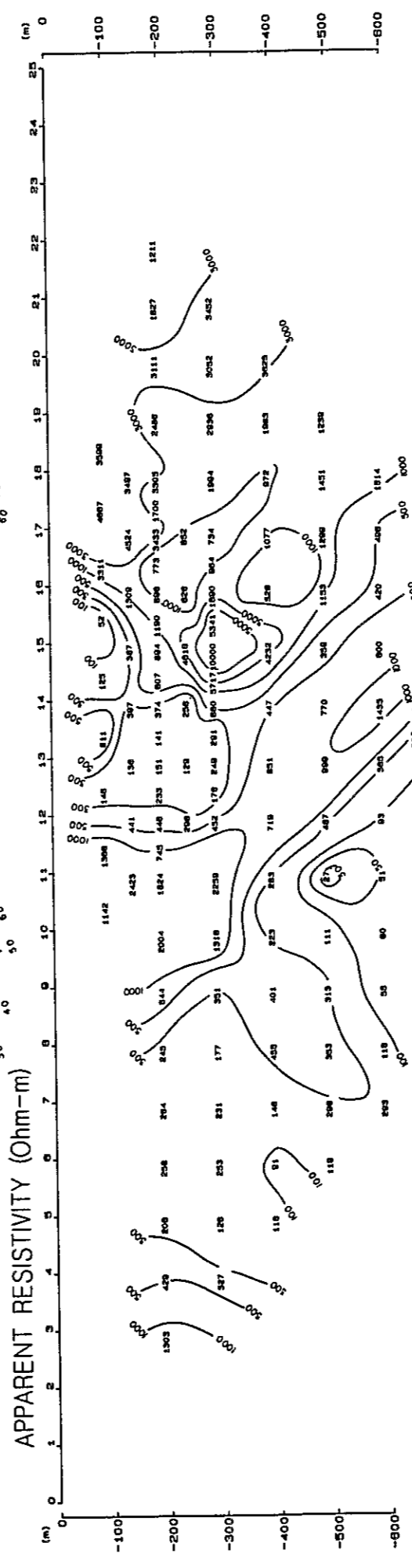
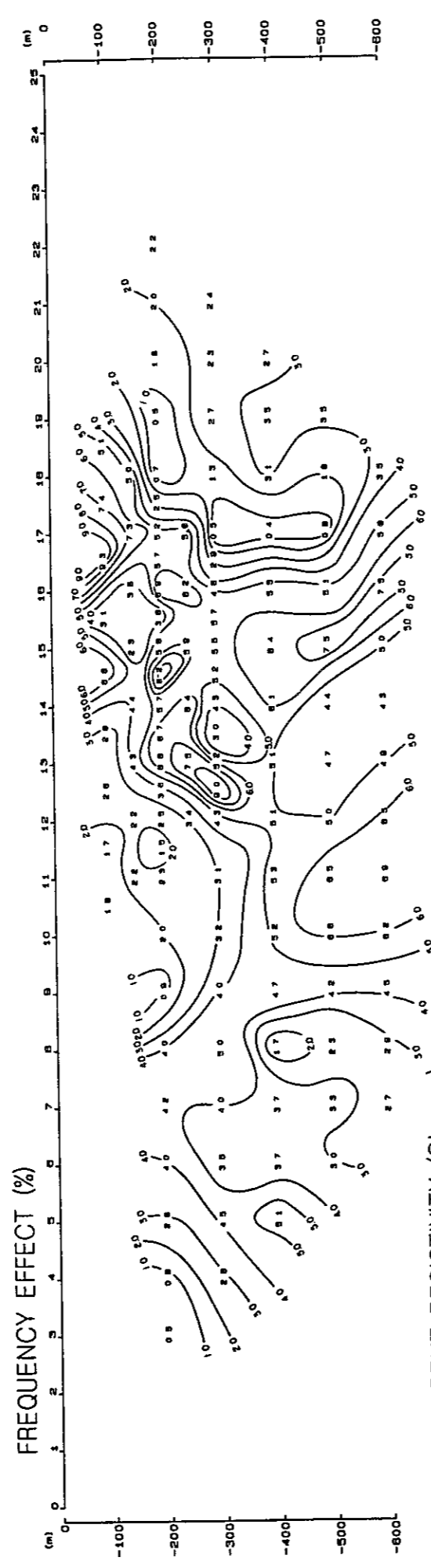
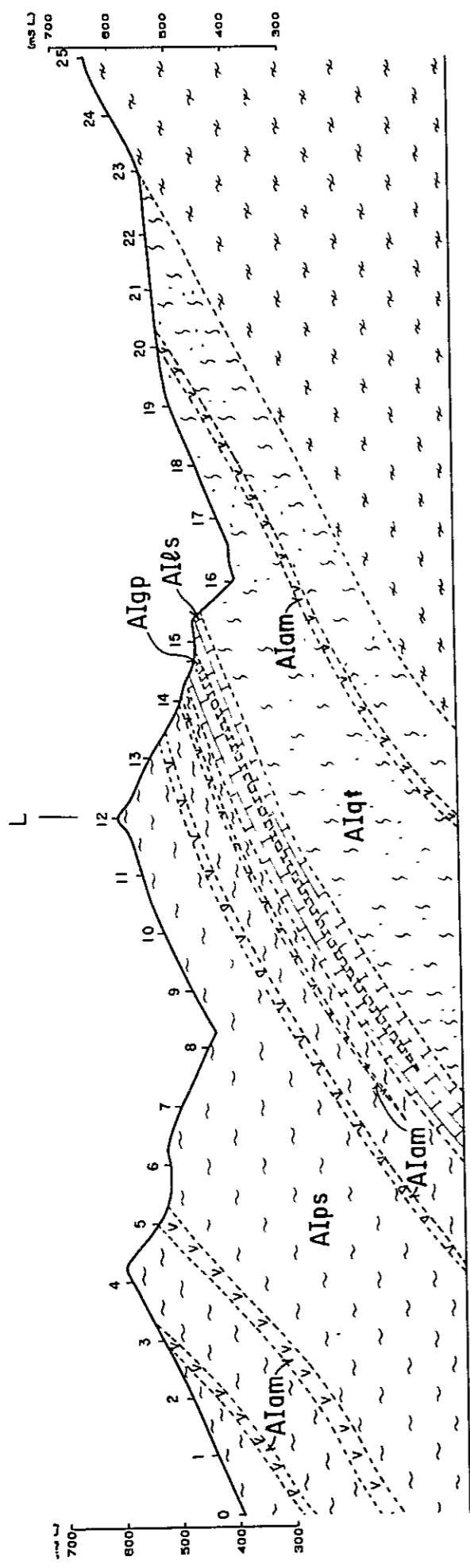


Fig II-3-11 IP Profile (Line G)

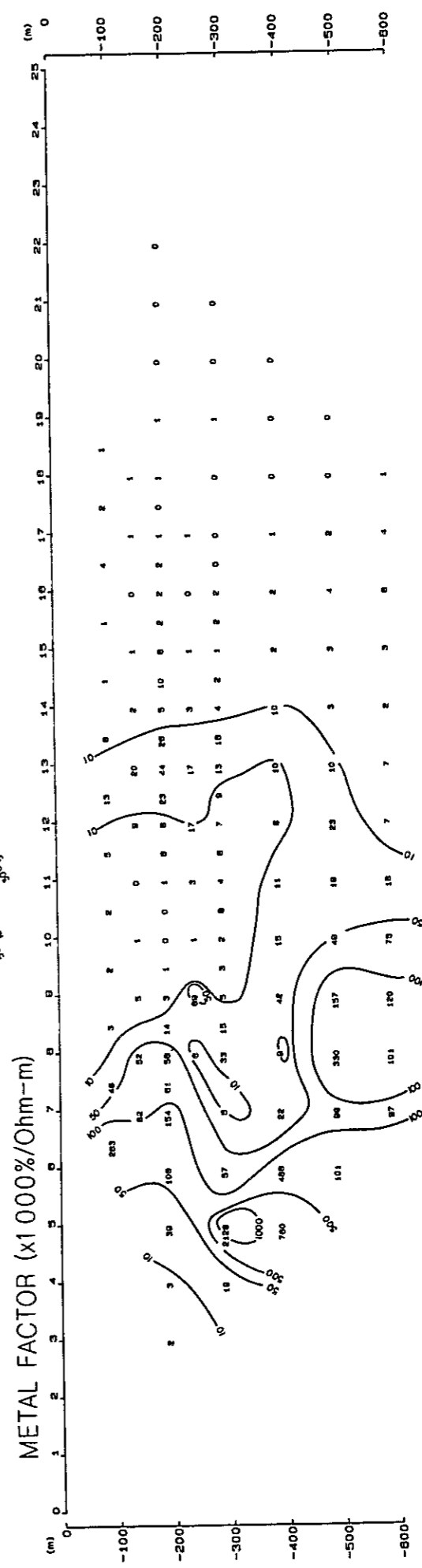
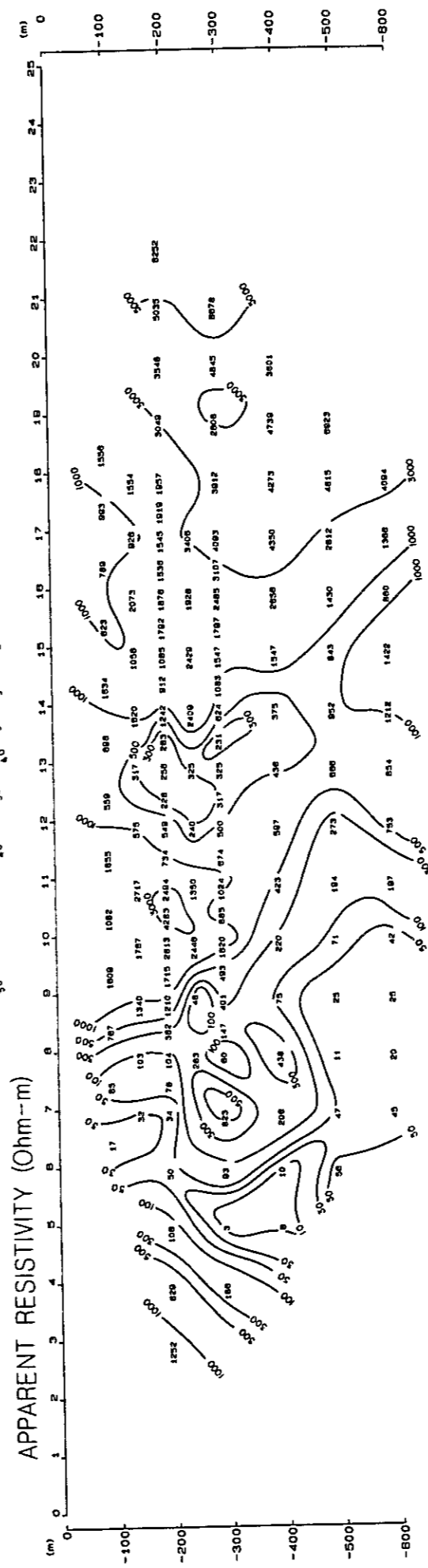
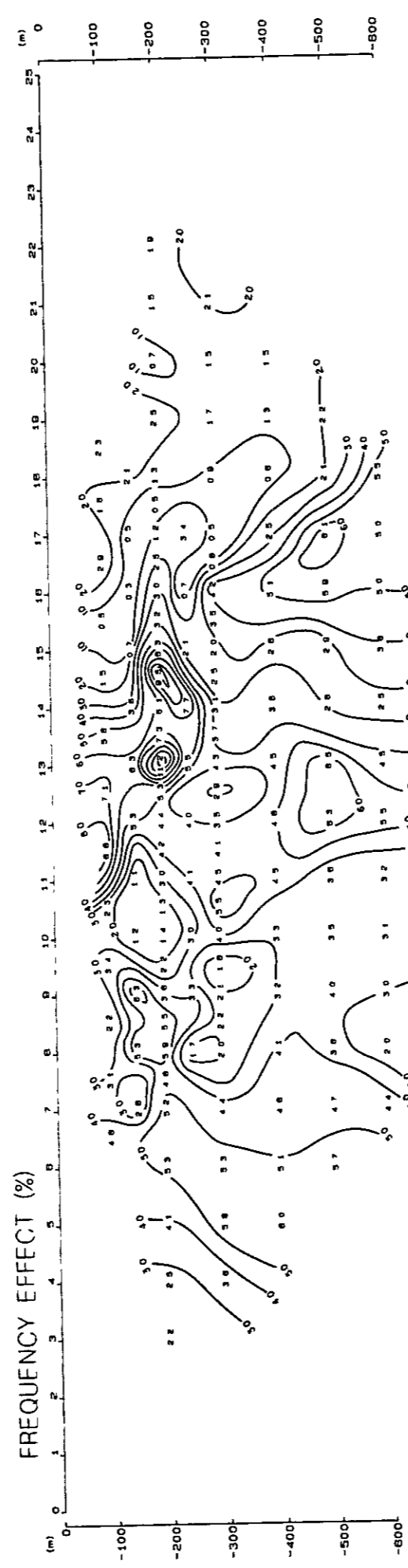
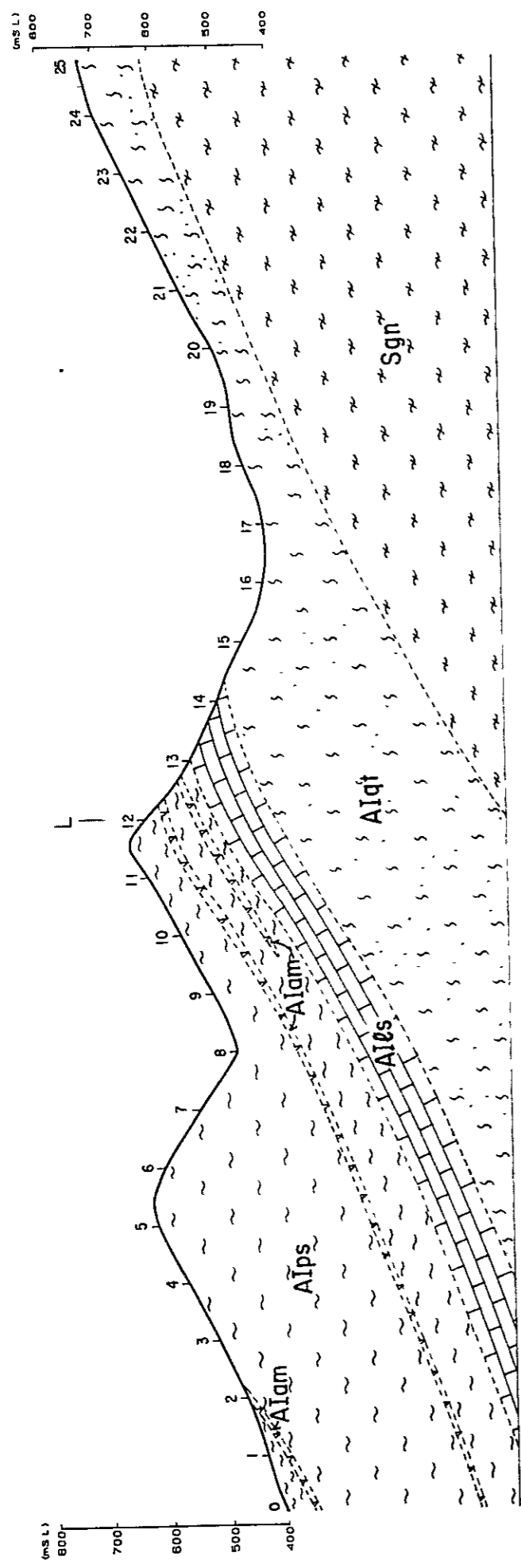


Fig II-3-12 IP Profile (Line H)

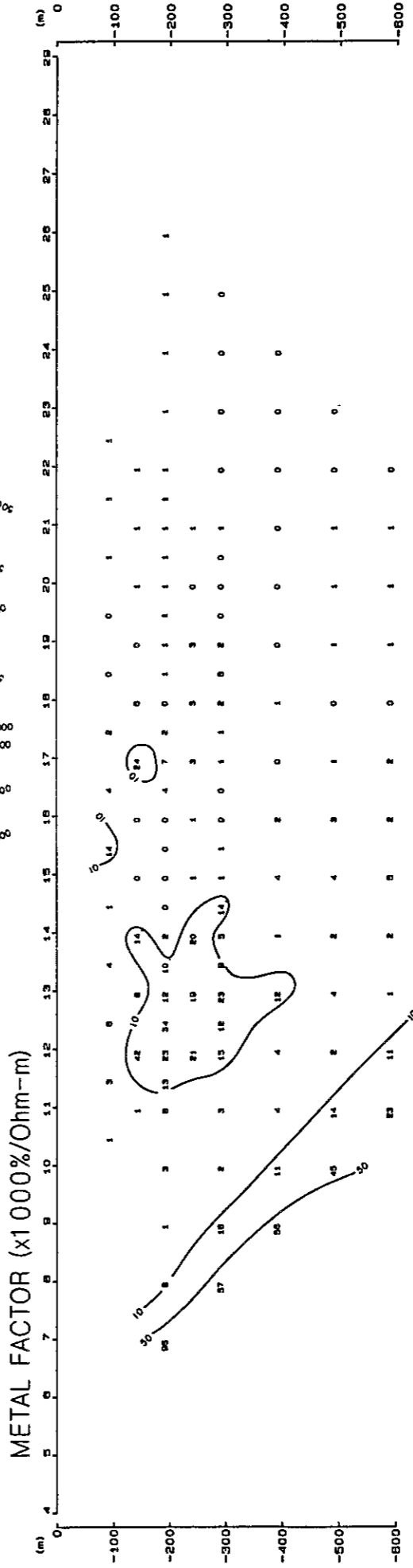
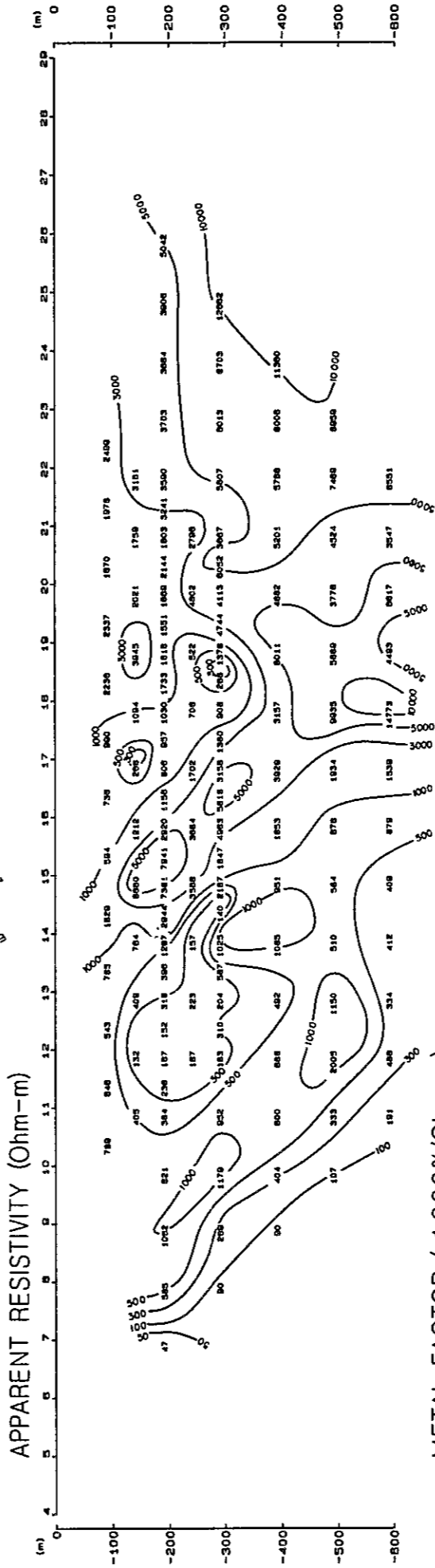
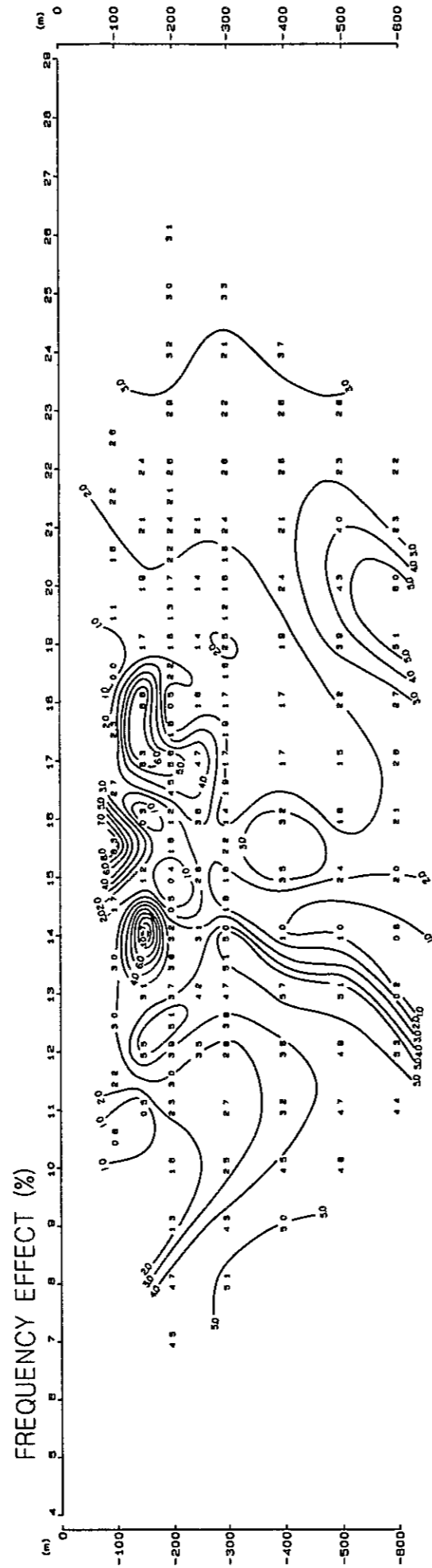
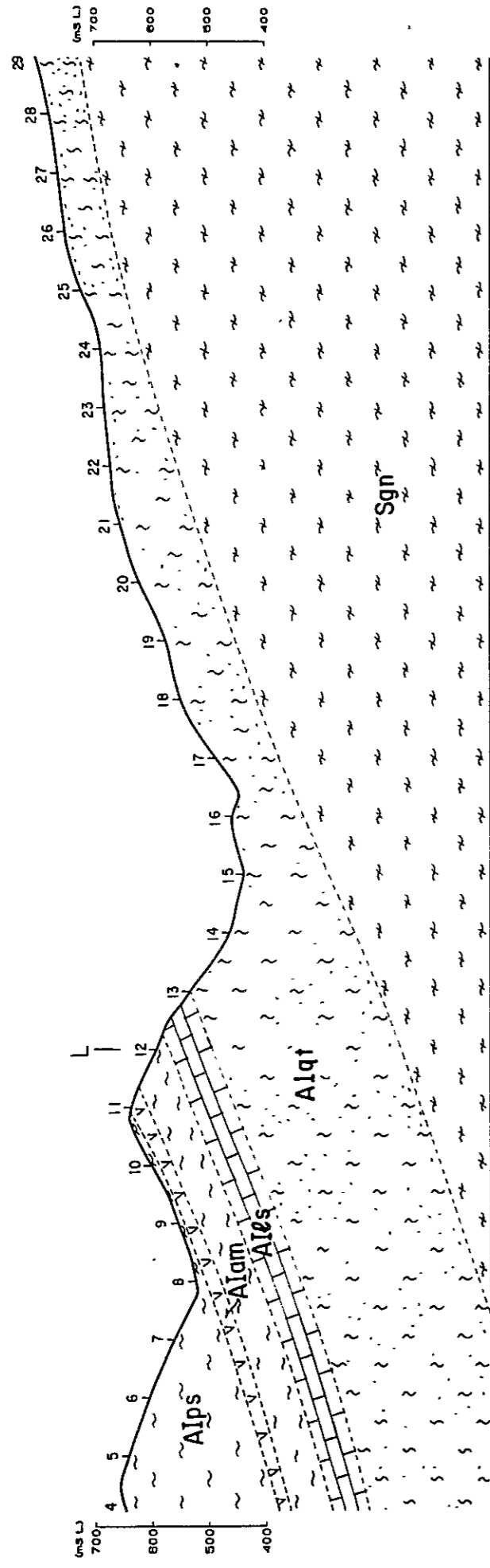


Fig II-3-13 IP Profile (Line I)

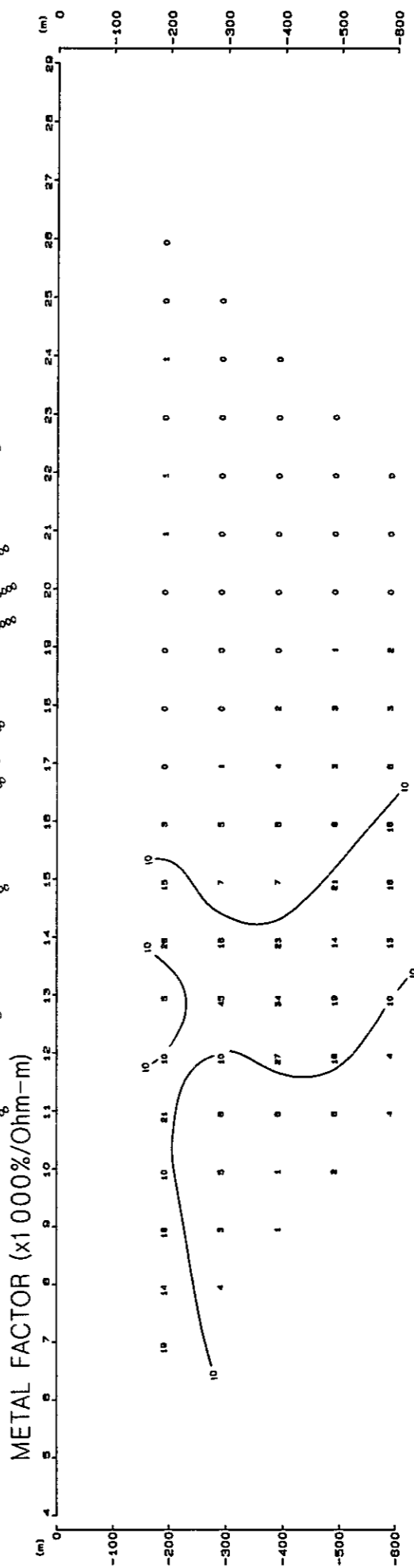
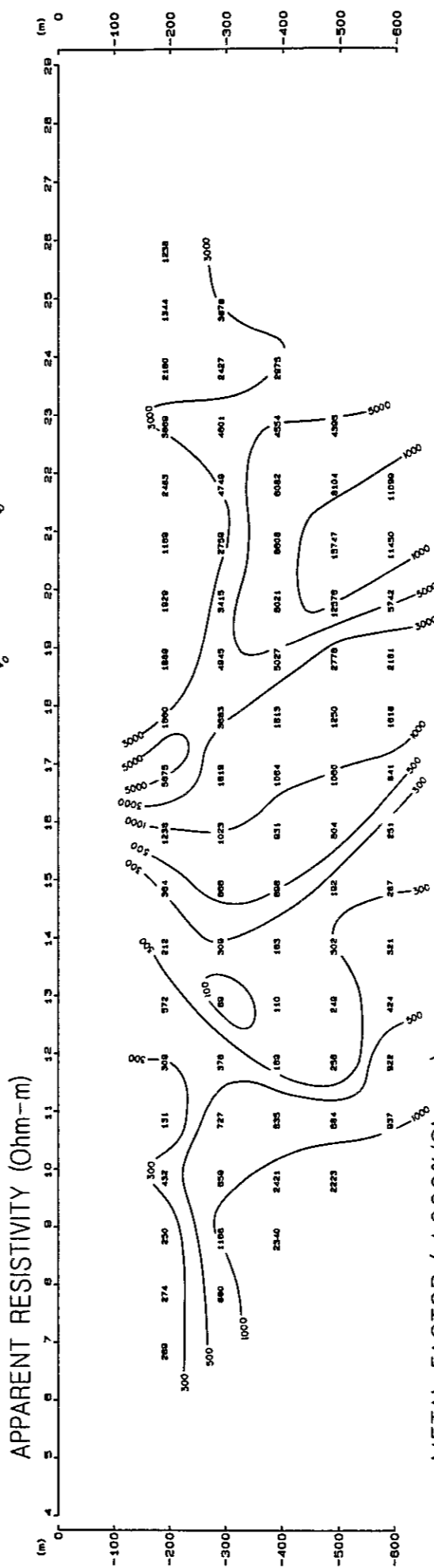
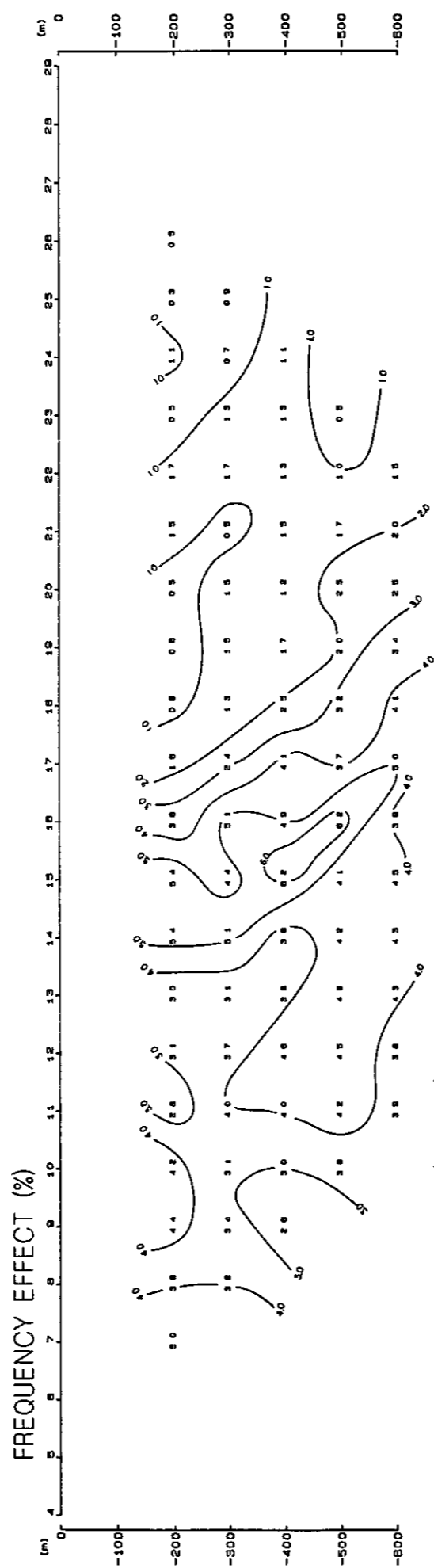
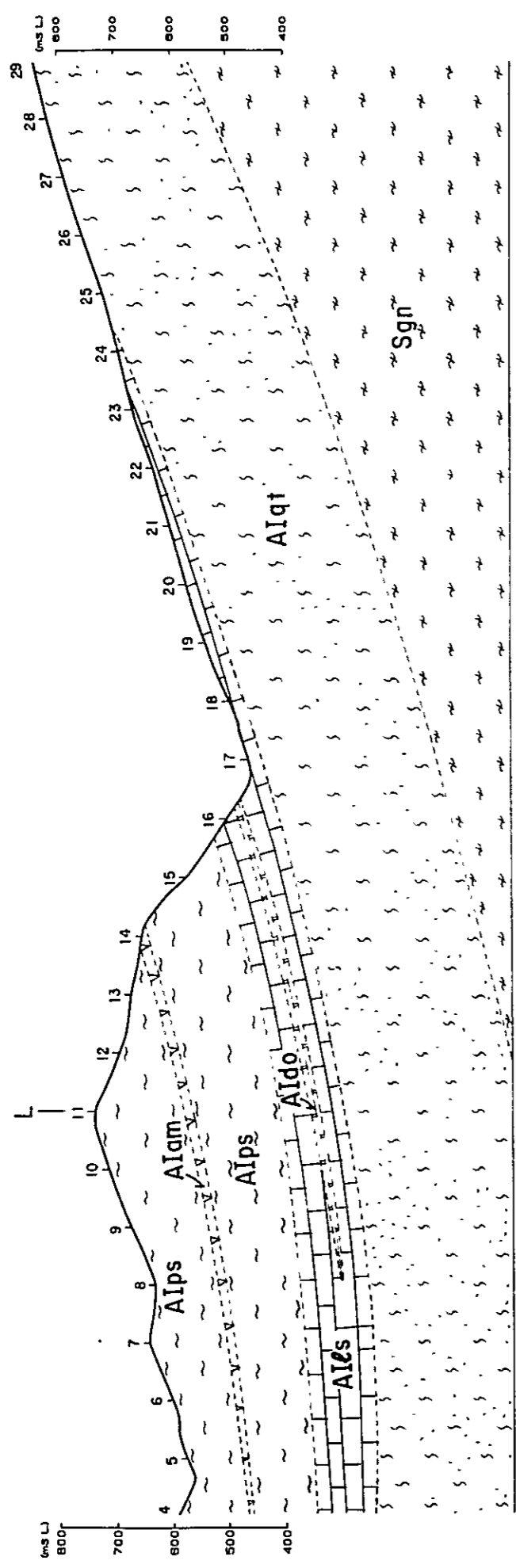


Fig II-3-14 IP Profile (Line J)

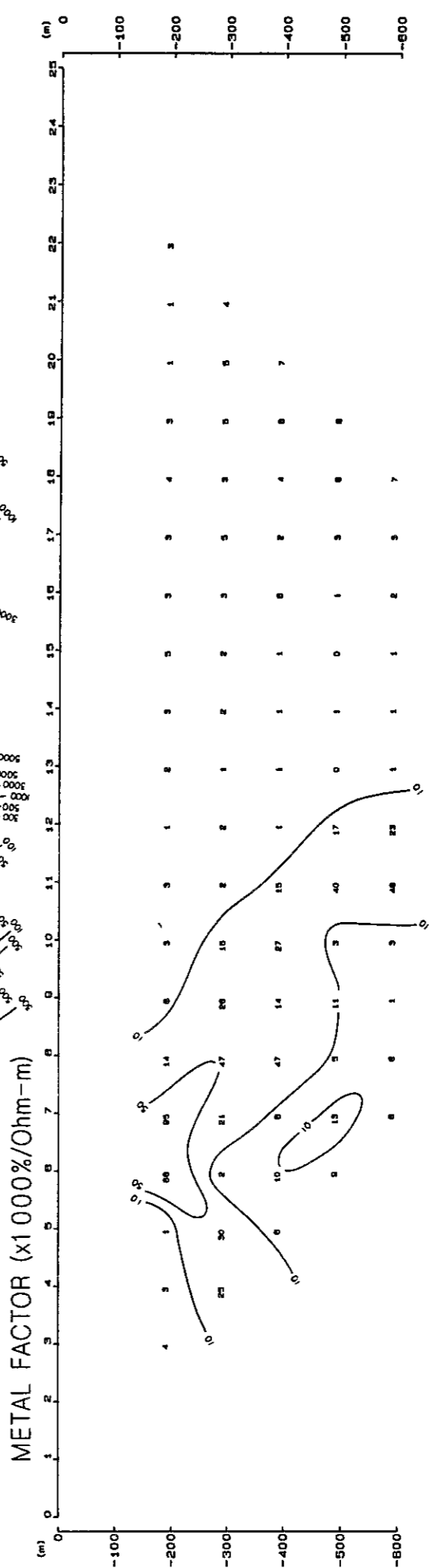
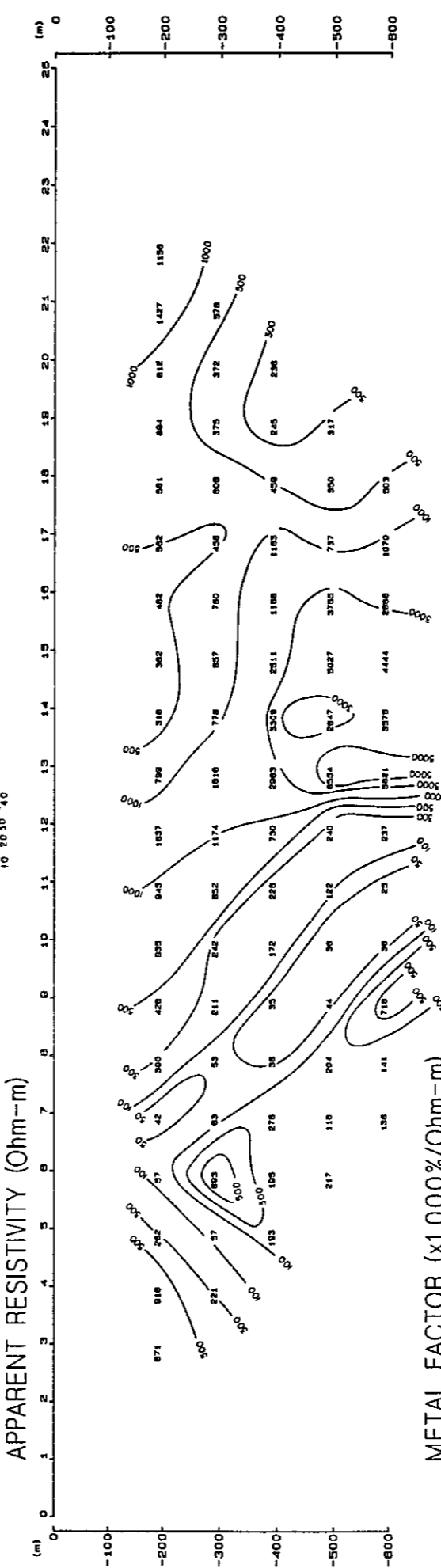
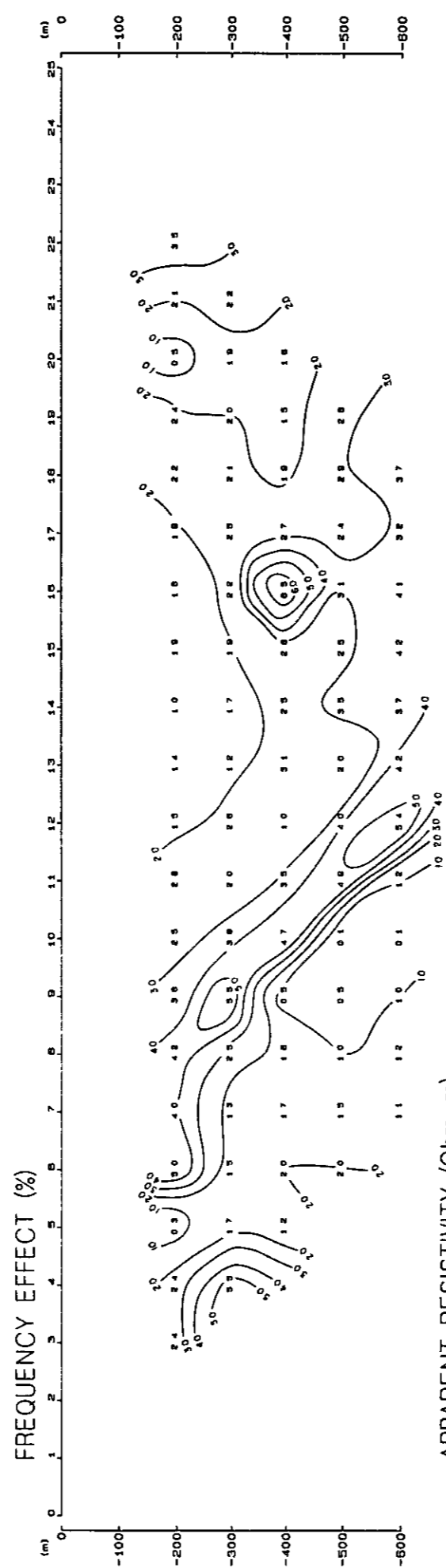
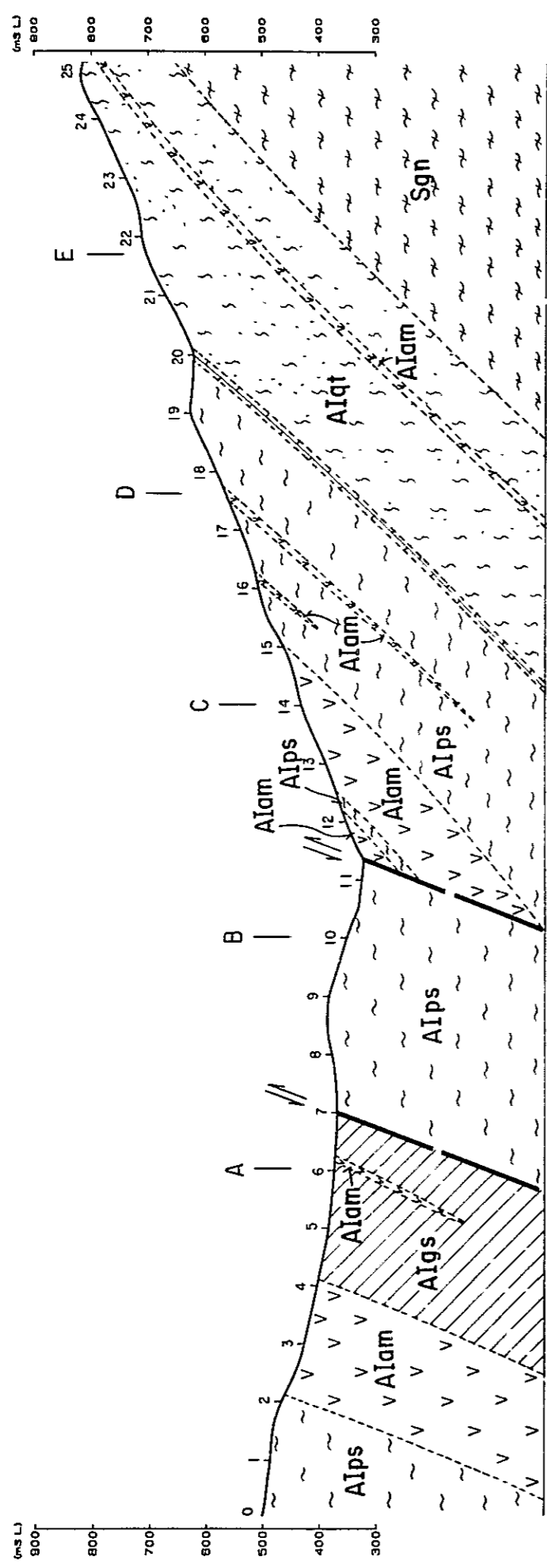


Fig II-3-15 IP Profile (Line K)

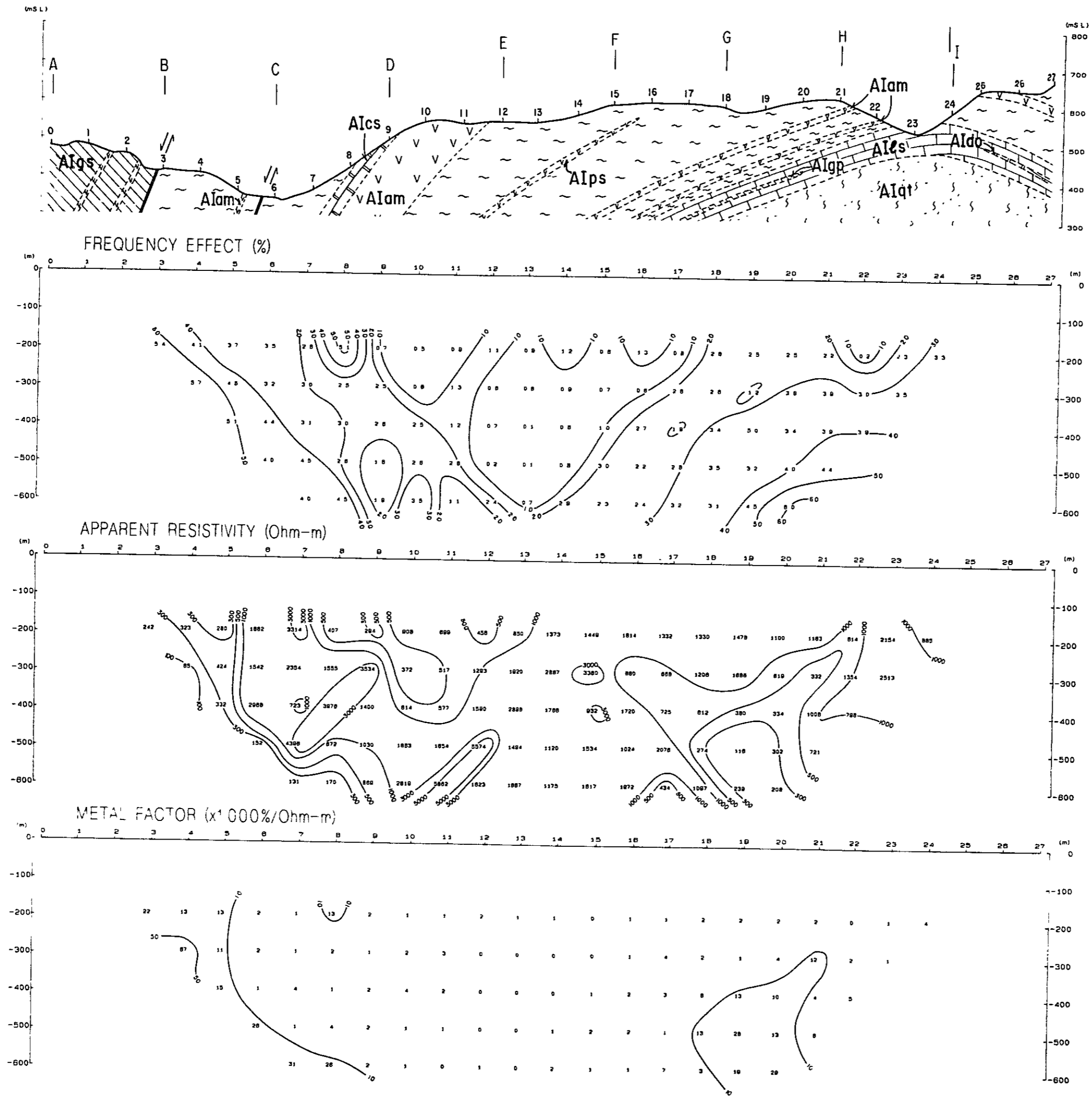


Fig II-3-16  
IP Profile (Line L)



### 3-3-2 Plane Analysis

Three types of plane maps were completed using the FE and apparent resistivity values at  $n=1, 3$  and  $5$ . The purpose of this analysis is to delineate the horizontal extent of the mineralized zone and to evaluate the dip and direction.

These maps do not indicate the information at the same level, but they show the distribution to a depth of 200 m, 400 m and 600 m below the surface, respectively.

#### (1) FE

The distinctive anomalous zones were detected in three areas as follows:

- i) The northern part of the survey area
- ii) The area east of No.20 on Lines B, C and D, and the central part of the survey area
- iii) The southwestern part of the survey area and the westside on Lines G, H, I and J.

These anomalous zones are called A, B and C anomalous zone, respectively.

#### A anomalous zone

The magnitude of anomaly becomes stronger and its extent becomes broader to the depths.

The anomaly pattern on  $n=1$  shows the banded distribution with comparatively low FE value.

The anomalous zone on  $n=3$ , which is divided into two portions and can not be seen on Line L, shows also a high FE value and seems to extend to the north. The two anomalies seen on  $n=3$  are connected on  $n=5$  to become a single anomaly pattern. This anomaly seems to be distributed in the extensive area.

The anomalous source is anticipated to widely exist at depth dipping northward, judging from the above-mentioned anomaly pattern.

#### B anomalous zone

The anomaly, which is detected east of No 20 on Lines B, C and D on  $n=1$ , continues to another anomaly distributed at depth ( $n=5$ ) along Line L. This anomaly is dominantly seen in a N-S direction on  $n=5$ .

Another anomaly observed east of Line L has a high FE value from the surface to the depths.

The anomaly of over 5% FE on  $n=1$ , which is located on the central part of above-mentioned anomalous zone, continues to the south and becomes widest on Line G. The anomaly on  $n=3$  is sporadically distributed northeast of Line F, and seems to be separated in two directions (south and southeast) at the south of Perau mine. This anomaly is





completely separated on  $n=5$ .

Consequently two anomalous sources below are inferred from the anomaly pattern.

- (a) The anomalous source whose magnitude gradually becomes higher and wider to the south and whose extension becomes wider to the southeast.
  - (b) The anomalous source which stretches at depth to the south, originating from Line D.
- C anomalous zone

This anomaly can be seen from the surface to a depth and its magnitude becomes stronger to the depth. In addition, the anomaly seems to broadly extend to the southwest and to connect to the B anomaly zone.

Although the anomaly on  $n=1$  is small, the east of Line H on  $n=3$  can be broadly seen with a high FE value. The anomaly is quite small on  $n=5$ . The source of this anomaly is inferred to gradually become shallow to the southwest.

## (2) Apparent Resistivity

The resistivity patterns on  $n=1$ , 3 and 5 are similar. The low resistivity less than  $500 \Omega\text{m}$  is seen in three areas ; (a) north of the survey area, (b) at the west side of Lines E to J, and (c) on the central part of the area. While the high resistivity more than  $1,000 \Omega\text{m}$  is distributed in two areas , (d) around Line L from the north to the southwest and (e) on the southeastern part of the area

- (a) This low resistivity zone, in which a lowest value is observed on  $n=1$ , correlates with the FE anomaly pattern. The low resistivity zone seems to dip northward and to extend to the north.
- (b) This low resistivity zone continues to (c) the low resistivity zone on  $n=3$  observed on the central part of the area. This resistivity pattern, the extent of which becomes gradually broad and shallow to the southwest and south, correlated also with that of the FE anomaly.
- (c) This low resistivity zone is seen at a shallow part to the northeast, while to the southwest, this zone is distributed from the surface to the depth and connects to (b) low resistivity zone described above
- (d) This high resistivity zone can not be seen at the depth and changes into middle resistivities ( $500 - 1,000 \Omega\text{m}$ ) that correlate with the FE anomalous zone.
- (e) This high resistivity zone becomes broad to the depth. That might indicate the resistive rock to be extensively at depth.



### (3) Relation of FE Anomalous Zone with the Geology

The interpretation for above-mentioned three anomalous zones with the geological results is presented below.

#### (i) A anomalous zone

This anomalous zone has a low resistivity and high FE value and is seen from the surface to the depth. Since graphite schist is cropped out in this zone, the source of the anomaly is inferred to be caused by graphite schist

#### (ii) B anomalous zone

This anomalous zone is separated into two anomaly types. One is the low FE anomaly zone associated with a high resistivity on the northeastern part of the area.

Other is the high anomaly zone with a low and middle resistivity on the central part of the area

The high resistivity of the former might be due to the quartzite broadly exposed on the northeastern and eastern part of the area. The low FE anomaly might be due to the amphibolite cropped out in quartzite, and the amphibolite bearing sulfide is expected to broadly exist at the depth, judging from the extensive distribution of anomaly to the depth. In addition, this low FE anomalous zone changes to a low and middle resistivity and high FE southward, and further extends to the south and southeast

The latter is assumed to be caused by another type of anomalous source, partly including the effect of above-mentioned mineralized amphibolite. Namely this anomaly zone might indicate to be caused by the Perau ore horizon. The source of the anomaly is expected to extend dipping westward, and to continue to the south and south-southeast. The resistivity of the latter is a little high (100–300  $\Omega\text{m}$ ) to a depth of 300 m from the surface and low (less than 100  $\Omega\text{m}$ ) at depth more than 500 m

A little high resistivity might correspond to calcopyrite rock and limestone which is ore horizon at a shallower depth than 300 m. A low resistivity might suggest that a amount of sulfide mineral in ore horizon increases at the depth more than 500 m, and/or that a great deal of graphite is intercalated in ore horizon.

#### (iii) C anomalous zone

This anomalous zone consists of a low resistivity and high FE, and is distributed in a south-east direction at shallow depth and in a southwest direction at the depth

As compared with A anomalous zone, the values of both FE and resistivity are similar



# LINE - G

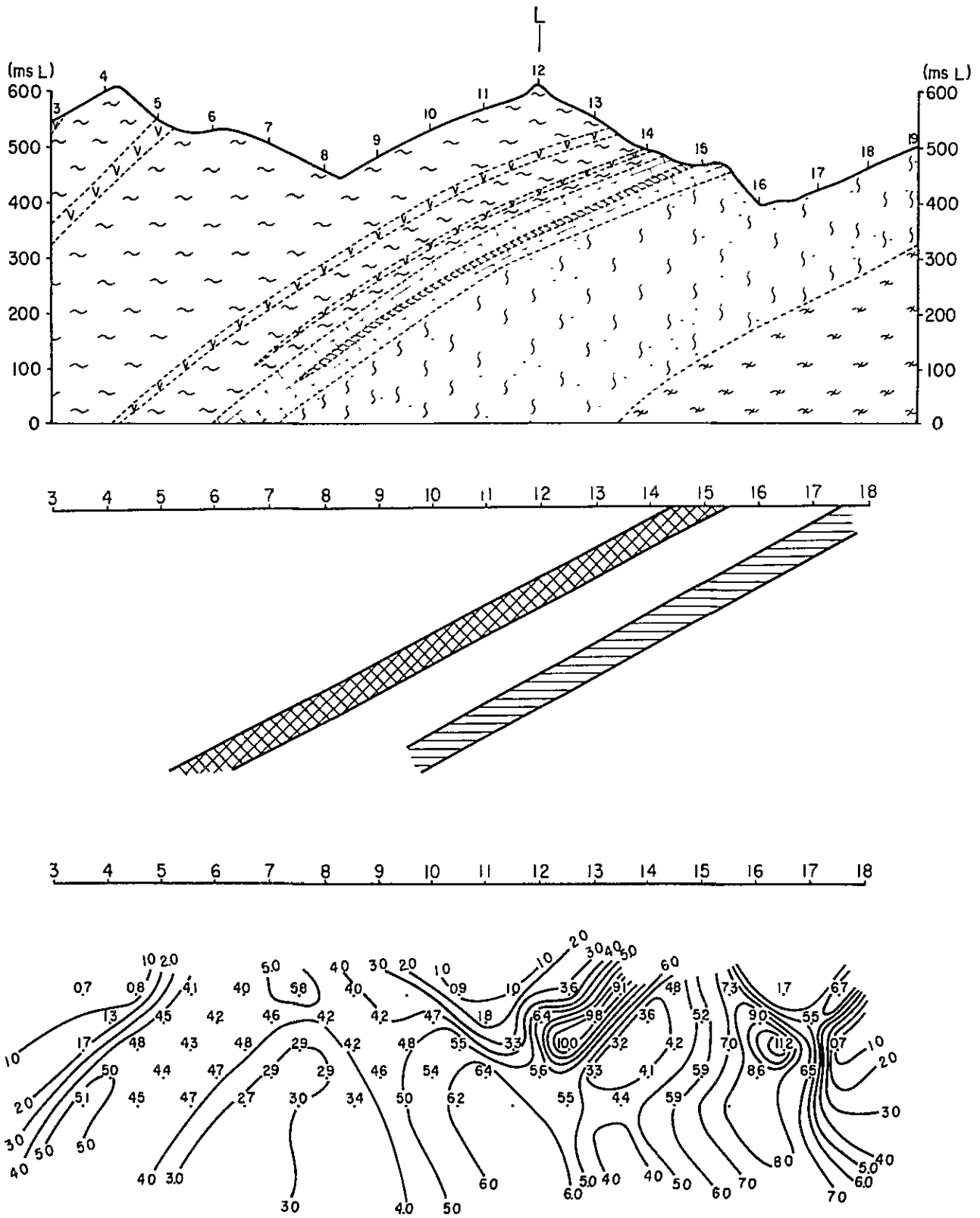


Fig. II-3-21 Relation of IP Anomaly and Perau Ore Horizon



to those in A anomaly zone. The low resistivity might be due to graphite schist exposed in this anomalous zone, and the high FE might be caused by the dissemination of pyrite and chalcopyrite in graphite schist.

The difference of graphite schist in A anomalous zone from that in C anomalous zone is as follows.

Graphite schist in A anomalous zone is loose, including coarse-grain quartz.

While, graphite schist exposed in C anomalous zone might be more conductive due to schistosity than that in A anomalous zone.

### 3-4 Summary

The summary of results obtained from the IP survey is presented here.

(1) The FE values observed in this survey are of 0.1 percent to 12.5 percent.

The FE anomalous zones of over 3.0 percent FE were detected to the north of the survey area and in the region from the central part to the southwest. These anomalous zones continue from the surface to depth with the extent of the anomalies wider at depth, and correlate with low and middle resistivity values of less than 1,000  $\Omega\text{m}$ .

(2) The resistivity values observed are of 3  $\Omega\text{m}$  to 1,000  $\Omega\text{m}$ . The low resistivity zones of less than 500  $\Omega\text{m}$  were detected to the north of the area, in the region from the north-eastern part to the southern part of the survey area, to the southwest. The high resistivity zones of more than 1,000  $\Omega\text{m}$  were detected at a shallow depth in and around the contacts between above-mentioned low resistivity zones, and broadly to the east.

(3) The results of physical measurements are as follows.

(i) Quartzite of Setuva formation shows a high resistivity and low FE.

(ii) Quartz indicates a highest resistivity and 6.3% FE value on average due to containing some sulfide.

(iii) Amphibolite, which belongs to Açungui I formation, disseminated in pyrite shows the lowest resistivity and 3.5% FE on average.

(4) The relation of the anomalous zones with the geological survey results and the summary is shown on table II-3-3.





Table II-3-3 Characteristics of Three IP Anomaly Zones

Anomalous zone		A	B	C
FE Anomaly	Magnitude	High FE (3 to 10.3%)	High FE (3 to 11.3%)	Middle FE (3 to 6%)
	Pattern	Dipping northward	There are two anomalous zones (1) Low and middle resistivity (2) Low resistivity	Dipping westward
Apparent Resistivity		Low resistivity (6 to 500 $\Omega$ m)	(1) Low and middle resistivity (2) Low resistivity	Low resistivity
Depth		From the surface to the depth	From the surface to the depth	From the surface to the depth
Type of distribution of anomaly		Banded distribution at a shallower depth Continuing to the north and northwest at depth The extent of the anomaly is not clear	Banded distribution in the south and southeast direction Banded distribution with 100 m in width to the south	Broad distribution in a southwest direction
Geology		Graphite schist	(1) Amphibolite associated with sulfide (2) Perau ore horizon	Graphite Schist
Possibility of ore deposit		No	(1) No (2) Yes	No



## CHAPTER 4 SPECTRAL IP METHOD

Spectral IP method is a new geophysical method being studied and developed since 1975. As this is comparatively a new method yet, following names are generally used;

- \* Spectral IP method
- \* Multifrequency IP method
- \* Complex Resistivity method (CR method)

In this report spectral IP method is used since Dr. S. H. Ward of Utah University adopted this name.

### 4-1 Survey Method

For the conventional IP method, the difference between resistivity measurements made at two frequencies (0.1 to 5 Hz) divided by the resistivity at one of two frequencies is measured as frequency effect. For the spectral IP method, however, all of the complex (real and imaginary) resistivity characteristics measured over a spectrum of frequency (0.001–100 Hz) must be obtained. The spectral IP method is a major step forward in electrical geophysical exploration inasmuch as it perceives the different parameters of the IP, resistivity, phase, and related electromagnetic coupling of the earth, separates their individual contributions, and presents a display for visual analysis and interpretation. Measurement of spectral IP is not basically different from conventional IP method.

#### Survey line

Line G and Line K of IP lines were used for this survey, with a communication wire line around 30 m parallelly apart from those lines (Fig II-4-1)

#### Potential Electrode

Nonpolarizable electrodes made by unglazed pottery filled with saturated copper-sulfate solution and a copper rod are used as potential electrodes. Three electrodes set in the same distance  $AB=BC$  were used in order to eject noises with differential function of the pre-amplifier as shown in Fig. II-4-2.

#### Current Electrode

Current electrode configuration adopted in this survey is shown in Fig II-4-3.



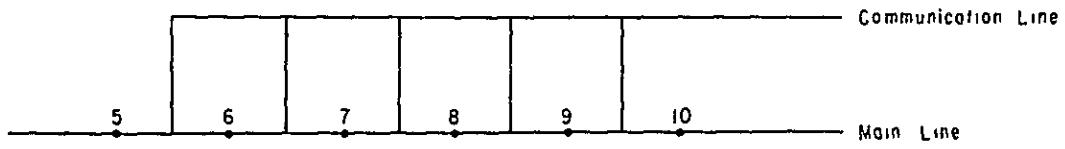


Fig. II-4-1 Survey and Communication Lines

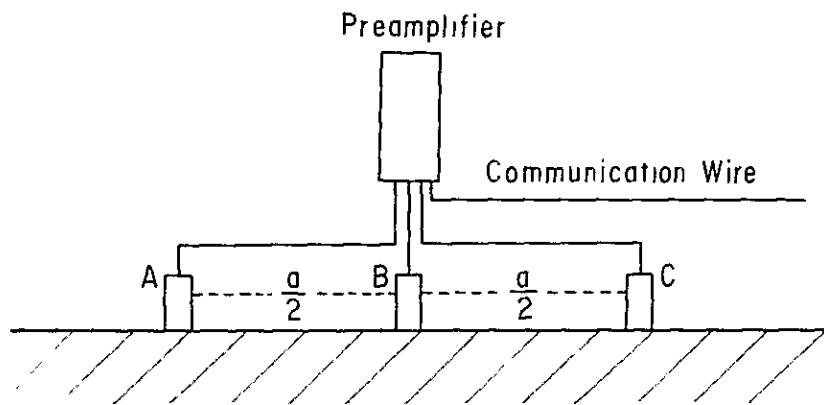


Fig. II-4-2 Arrangement of Potential Electrodes and Preamplifiers

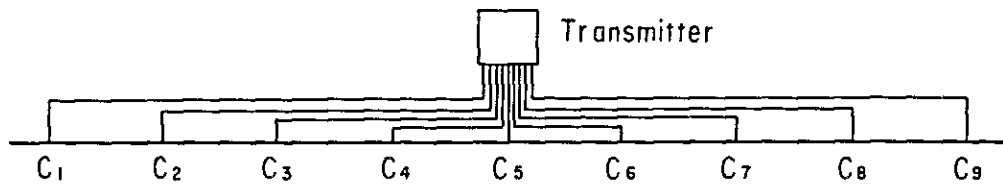


Fig. II-4-3 Arrangement of Current Electrodes and Wires



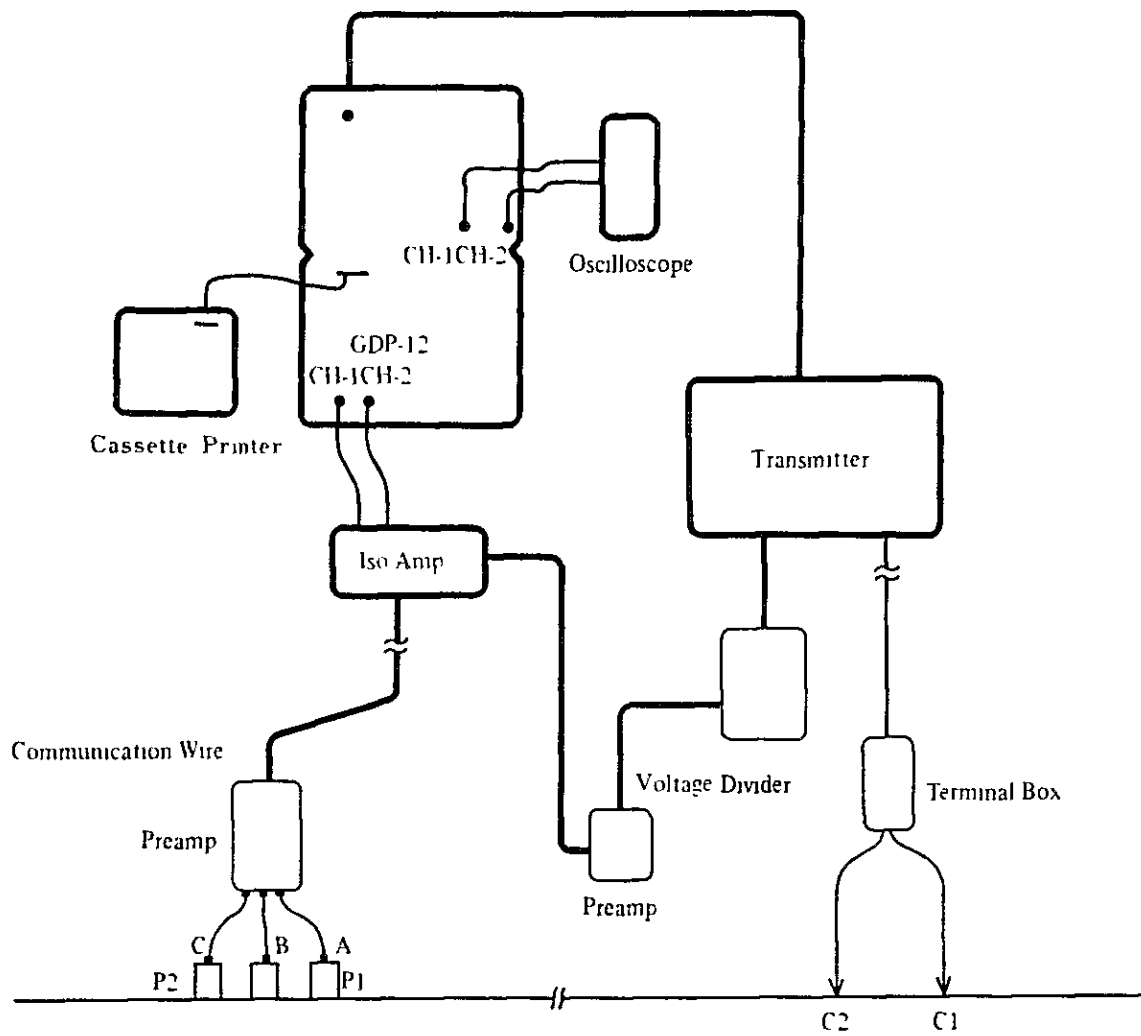


Fig. II-4-4 Block Diagram of Spectral IP Survey Instruments





and the names of the instruments are shown in Fig. II-4-4.

#### 4-2 Data Processing

For the spectral IP method normalized magnitude and phase to the lowest frequency are measured for the wide range of frequency. The results of measurements are plotted on a Cole-Cole map or on a frequency spectrum.

##### Spectral IP Theory

An exceedingly simple relaxation model which has been found to fit a variety of laboratory complex resistivity results (Madden and Cantwell, 1967; Pelton et al. 1972) was originally proposed by Cole and Cole (1941) to predict complex dielectric behavior. The circuit of Fig. II-4-5 (b) is a resistive network which exhibits a Cole-Cole relaxation. Other equivalent circuits can be envisioned which also have the same response, but this one provides a convenient analogy to one view of the pore geometry in a mineralized rock which is shown in Fig. II-4-5 (a). The general behavior of the equivalent circuit with frequency is given in Fig. II-4-5 (c). In-phase and out-of-phase are shown in Fig. II-4-6. In displaying IP phase data in graphical form, it is convenient to plot such as suggested by Cole and Cole, on which in-phase is shown against out of phase response (Fig. II-4-7).

##### Data processing

The data obtained from the field survey are phase difference ( $\phi$ ), apparent receiving potential of  $CH_2 (M_1)$  and  $CH_2 (M_2)$  and the ratio of  $M_1/M_2$  over the frequency of 0.125 to 64 Hz. Those values of real part and imaginary part calculated by the following formula are plotted on the Cole-Cole map.

In order to normalize each magnitude ratio to the lowest frequency, each  $M_1/M_2$  are divided by  $M_4$ . Then the real part is  $N_i \times \cos \phi$  and the imaginary part is  $N_i \times \sin \phi$ , where  $N_i$  is the normalized ratio of  $M_1/M_4$ .

A Cole-Cole map is obtained by plotting those real part on horizontal axis and imaginary part on vertical axis as shown in Fig. II-4-8.

##### Three point decoupling

This is a method to calculate the DC phase extending the quadratic equation of frequency and phase. Under the assumption of the quadratic function of  $y = ax^2 + bx + c$  giving frequency  $x=0.5, 0.25$  and  $0.125$  and phase  $y=0.5, 0.25$  and  $0.125$ , then

$$\phi_{0.5} = a (0.5)^2 + b (0.5) + c$$

$$\phi_{0.25} = a (0.25)^2 + b (0.25) + c$$



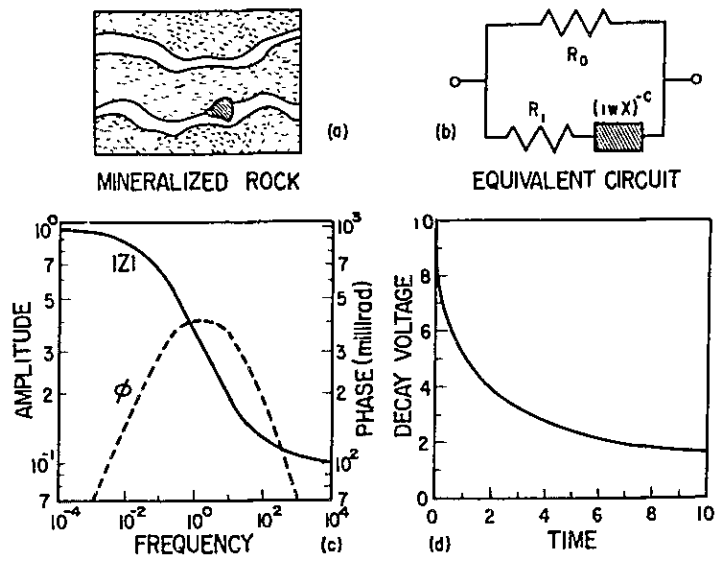


Fig. II-4-5 Spectral IP Effect

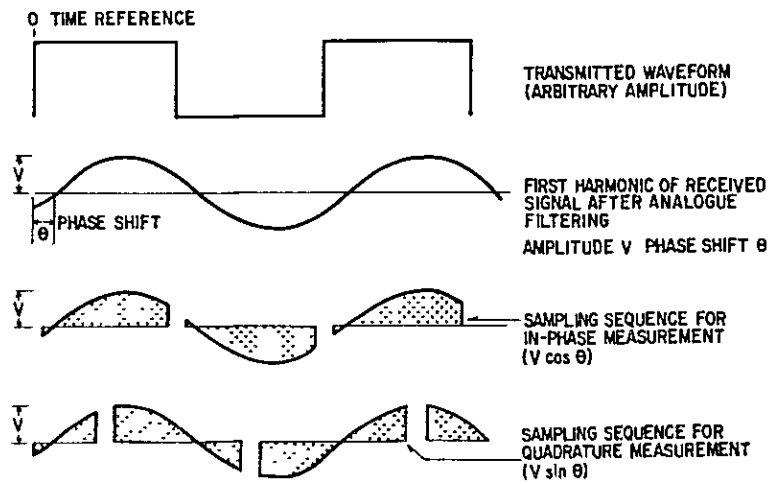


Fig. II-4-6 Transmitting and Receiving Wave-forms



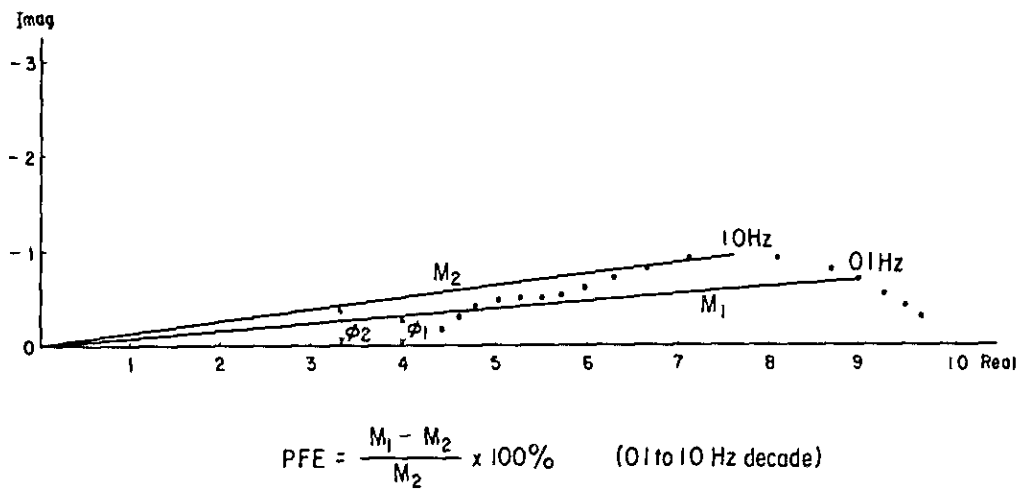


Fig. II-4-7 Relation between Frequency Effect and Phase Shift

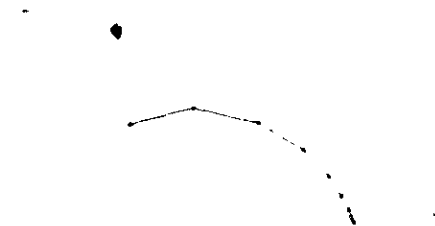


Fig. II-4-8 Example for Cole-Cole Diagram



$$\phi_{0.125} = a (0.125)^2 + b (0.125) + c$$

those formula are solved as

$$c = \frac{8}{3} \phi_{0.125} - 2\phi_{0.25} + \frac{1}{3} \phi_{0.5}$$

where, c is approximately considered as DC phase.

#### Percent Frequency Effect

PFE are calculated by using the normalized magnitude ratio N as follows,

$$\text{PFE (0.125-1.0)} = (N_4 - N_7) / N_7 \times 100$$

$$\text{or, PFE (0.125-1.0)} = (M_4 - M_7) / M_7 \times 100$$

### 4-3 Interpretation

#### Line G

Apparent resistivity is generally high and IP effect is weak in the eastern part of No.16 becoming eminent towards east, which is considered to be due to quartzite, as the rock sample measurement show low FE and high resistivity. Strong west dipping IP anomaly are detected around No.14 with a good coincidence with the horizon of Perau ore deposits, which is located in the middle of the anomaly. This concludes that the anomalies are due to Perau ore deposit. This anomaly is named as B. Weak east dipping IP anomalies are seen around n=1 of No 10 with apparent resistivity higher than 1,000  $\Omega\text{m}$  and comparatively low resistivity are also seen on both side. Especially on the western side, apparent resistivity is lower than 200  $\Omega\text{m}$ , which suggest the complex structure with big resistivity contrast. Low apparent resistivity of 200  $\Omega\text{m}$  with strong IP anomaly are seen between No.6 and No.8 showing pants-leg shape anomaly. The negative coupling phenomena are the characteristics of this anomalous zone, which are often seen in the low resistivity layer surrounded by high resistivity. This zone is named as C anomaly.

#### Line K

East dipping low resistivity zone is extending from the surface to the depth at No.8. On the eastern side of this low resistive anomaly IP effect is generally weak and the resistivity is high. In the western side, pants-leg shaped strong IP anomaly with low resistivity anomaly are seen. This anomalous zone is called as A. As graphite schist distribute around No.5~No.8 where anomaly A are detected, this anomaly is considered to be due to graphite schist, which seems to develop to the depth in northeast dipping.

Thus, on both Line G and Line K, strong IP anomalies of A, B and C were detected.





Anomalies A and B are considered to be due to Perau ore deposits accompanied by graphite schist and pyrite, but those two anomalies were expected to be detected before this survey. One of the purpose of this survey is to know each characteristics of the anomaly for the future study. Each characteristics of anomaly A, B and C are as follows;

#### Anomaly A

In this anomalous zone, negative coupling phenomena are seen which is stronger than those of anomaly C. This is considered to be due to the high resistivity rocks in the eastern vicinity and the lower resistivity (several 10  $\Omega$ m) of this anomalous zone itself than that of anomaly C. The average of 3-point decoupling values are  $-25$  to  $-30$  mrad. Although it is difficult to classify the spectrum as the negative coupling is dominated, the spectral type of phase for the frequency less than 1 Hz has a tendency of constant or slight increasing with frequency judging from the results of  $a=100$  m spacing, although negative coupling makes the classification of the spectrum difficult.

Apparent resistivity in this anomalous zone range from 20  $\Omega$ m up to 200  $\Omega$ m and the results of  $a=100$  m spacing suggest that around 20  $\Omega$ m resistivity detected near No.5~No.6 which shows pants-leg shape might reflect the resistivity of graphite schist seen in this area.

#### Anomaly B

In order to detect the detail pattern of Perau ore body around No.14~No.15, the shorter electrode spacing of  $a=100$  m was adopted by changing  $n$  from 1 to 3 and the followings are the discussion on the characteristics of anomaly B and Perau ore deposits. Three point decoupling values which show the strength of IP effect indicate less than  $-30$  mrad at  $n=1\sim 3$  of No.14 dipping west. This suggests the existence of west dipping Perau ore deposit accompanied by pyrite from the surface. Judging from the spectral map of phase at  $a=200$  m, electromagnetic coupling is rarely seen in the lower frequency range of 1 Hz, where discussion of spectral type could be made quantitatively. General trend of the spectrum in the lower frequency less than 1 Hz is almost flat or a little decreasing with the frequency. In case of  $a=200$  m the same spectral type is seen in the area of No.14~No.16 both along the east and west dipping pants-leg shaped anomalies towards depths which are the causative anomalous source of Perau mine.

#### Anomaly C

The characteristic of this anomaly is a negative coupling, which might reflect the non homogeneous structure with partly high conductive layer surrounded by high resistivity zone. In this case apparent resistivity of the causative source is around 100  $\Omega$ m, while



in the eastern vicinity different rocks with very high resistivity seem to distribute in this area to cause this negative coupling in this area. Three point decoupling values are all less than  $-30$  mrad and at the depth of 400 m below No.8 of Line G, the phase shift is  $-40$  mrad, which is the stronger IP effect than anomaly A. Even in the range of lower frequency than 1 Hz, the effect of electromagnetic coupling are seen on the phase spectral map. Considering the effect of the electromagnetic coupling, the spectral type of phase in the range of less than 1 Hz shows a gradually decreasing phase with frequency. Apparent resistivity in the anomalous zone is considered to be around  $100 \Omega\text{m}$  from the resistivity pattern.

#### 4-4 Summary of Spectral IP

As spectral IP was conducted over the same survey lines of Lines K and G and the same anomalies were detected with the conventional IP, the same naming are used for the anomalies.

Characteristics of three anomaly is summarized as follows.

Table II -4-1 Characteristics of Three Spectral IP Anomaly Zones

Anomaly	A	B	C
Apparent resistivity ( $\Omega\text{m}$ )	scores	200–300	$100 \pm$
IP effect	Weak	Middle	Strong
Spectral type in the frequency range less than 1 Hz *1	flat or increasing	flat or decreasing	decreasing
Coupling phenomena *2	Negative	?	Negative

\*1 Qualitative tendency of spectral type vs. frequency

\*2 Anomaly A shows stronger negative coupling than C

Anomaly A detected in the western side of line K is reflecting the graphite schist.

Anomaly B locates in the middle of Line G at Perau mine area indicating the west dipping Perau ore horizon.

Anomaly C seen in the west of Line G has a quite different pattern with that of anomaly B, which would not suggest the causative sulfide mineralization of copper, lead and zinc. Although some anomaly looks like a pattern of anomaly A, IP effect is stronger than A due to graphite schist with stronger pyritization. There is, however, another possibility of different type of mineralization.

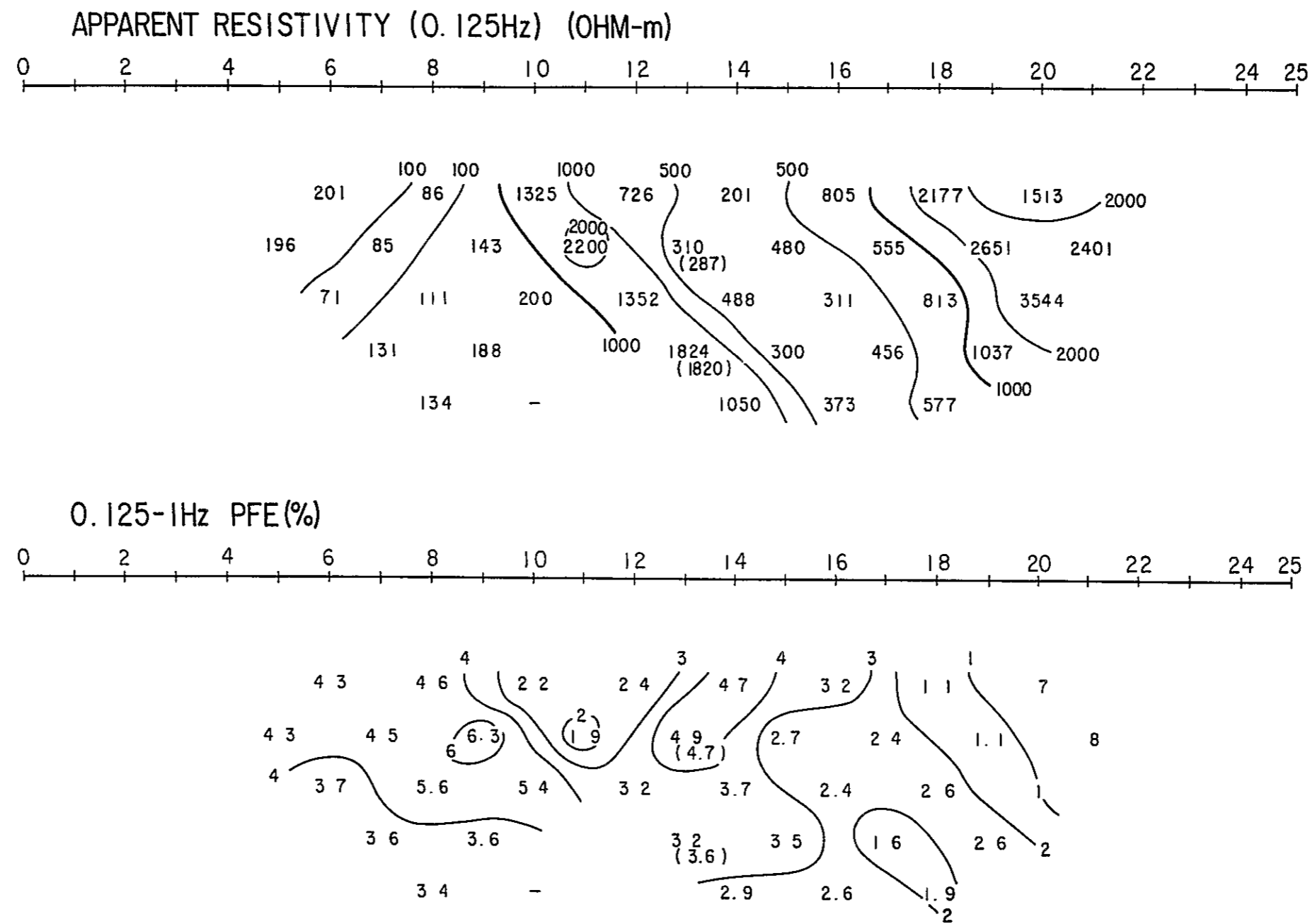


Fig. II-4-9 Spectral IP Pseudo-Section(Line G)

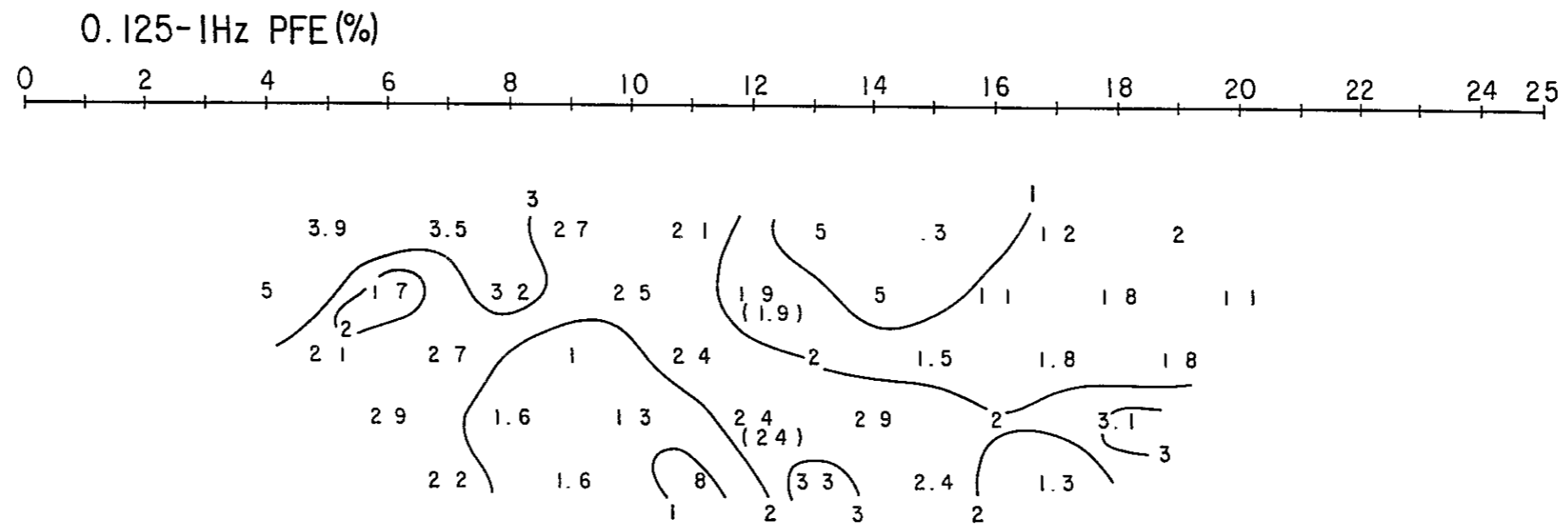
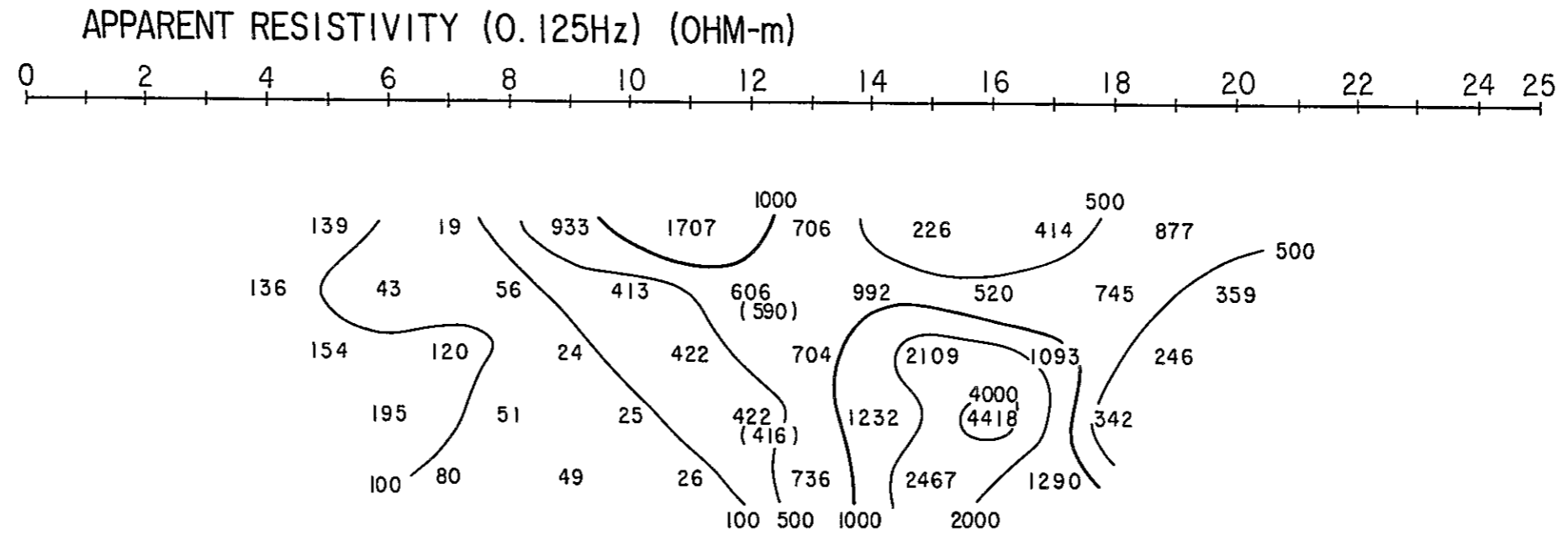
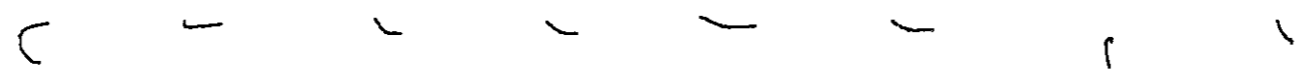


Fig. II-4-10 Spectral IP Pseudo-Section(Line K)

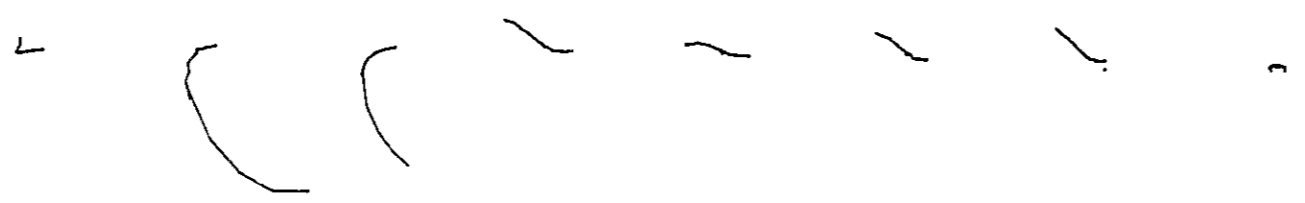
N= 1



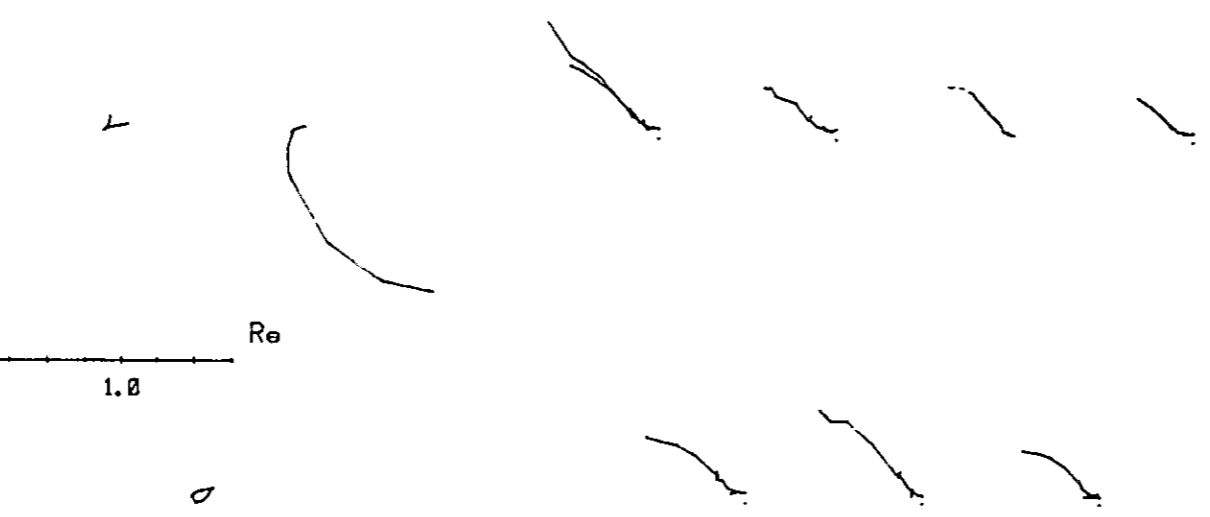
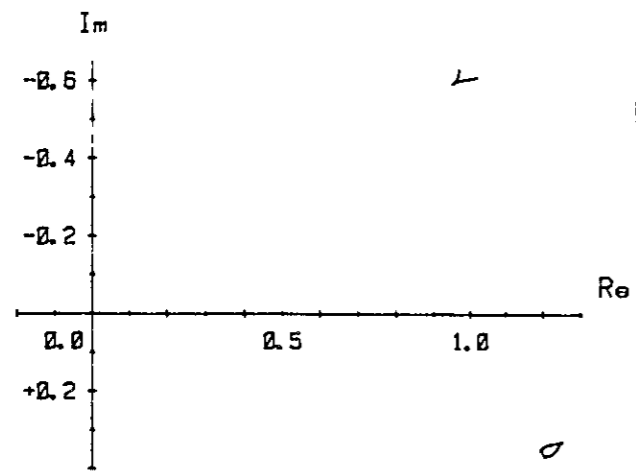
N= 2



N= 3



N= 4



N= 5

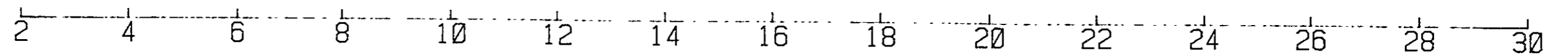


Fig. II-4-11 Cole-Cole Diagram(Line G)

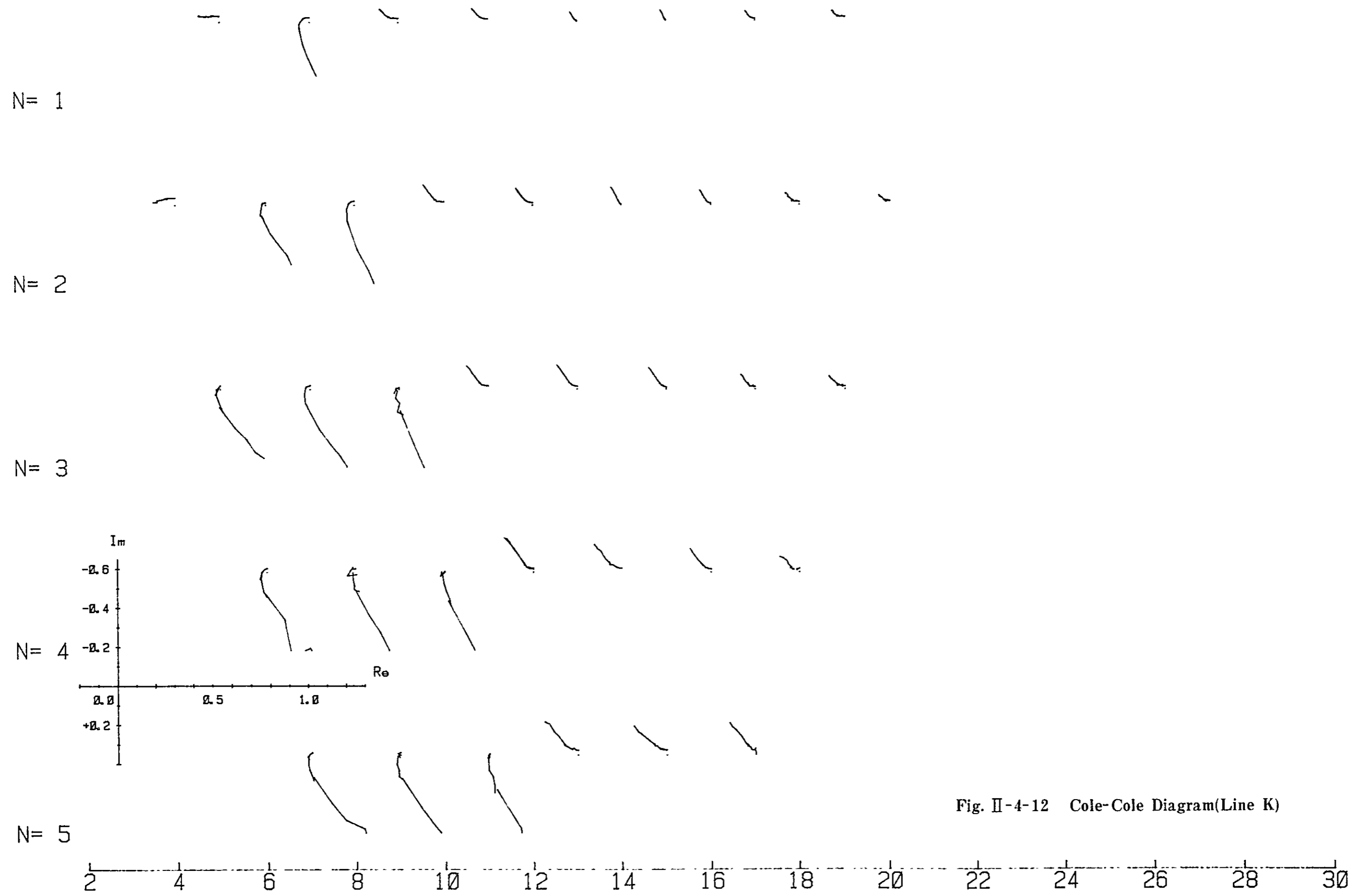


Fig. II-4-12 Cole-Cole Diagram(Line K)



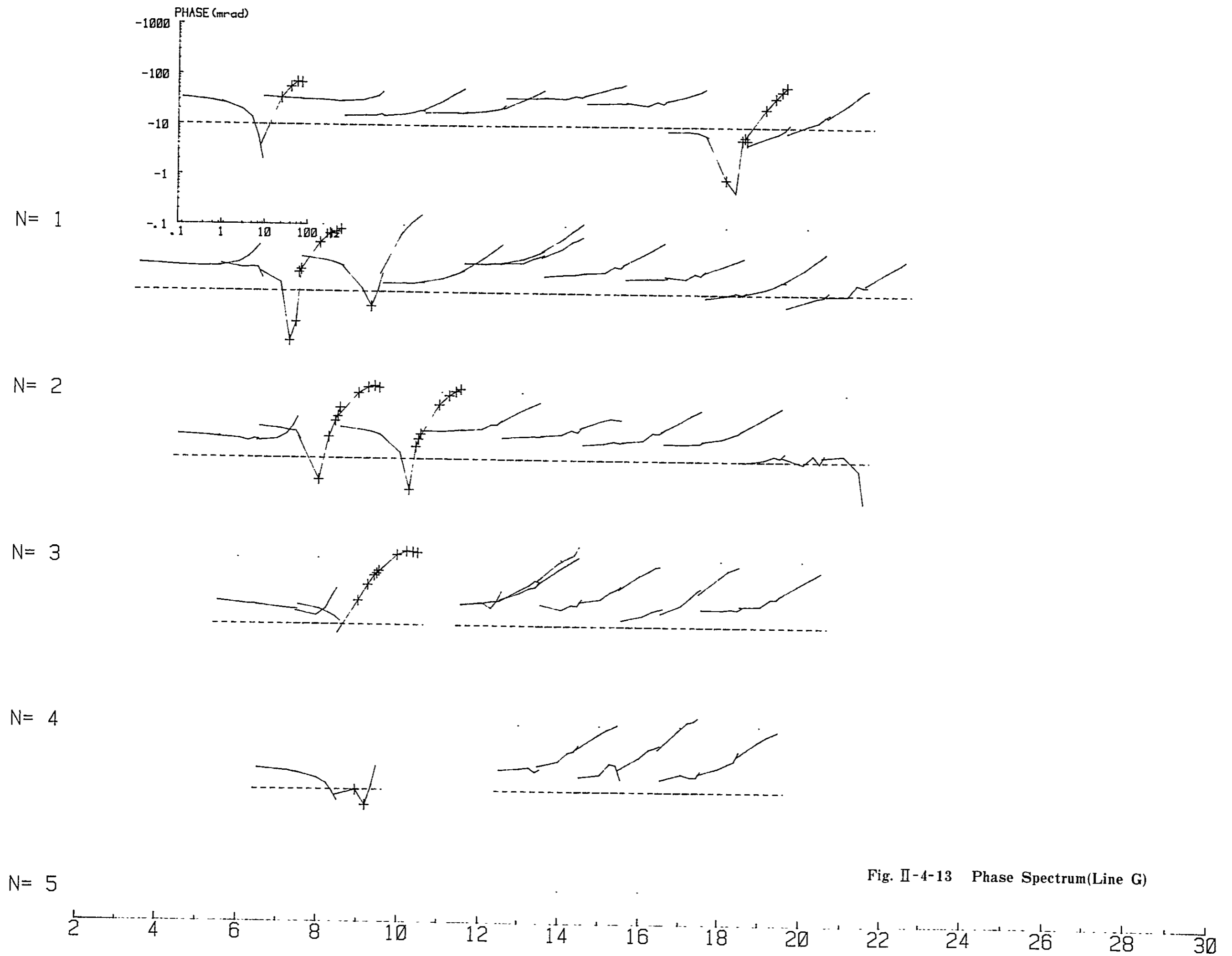
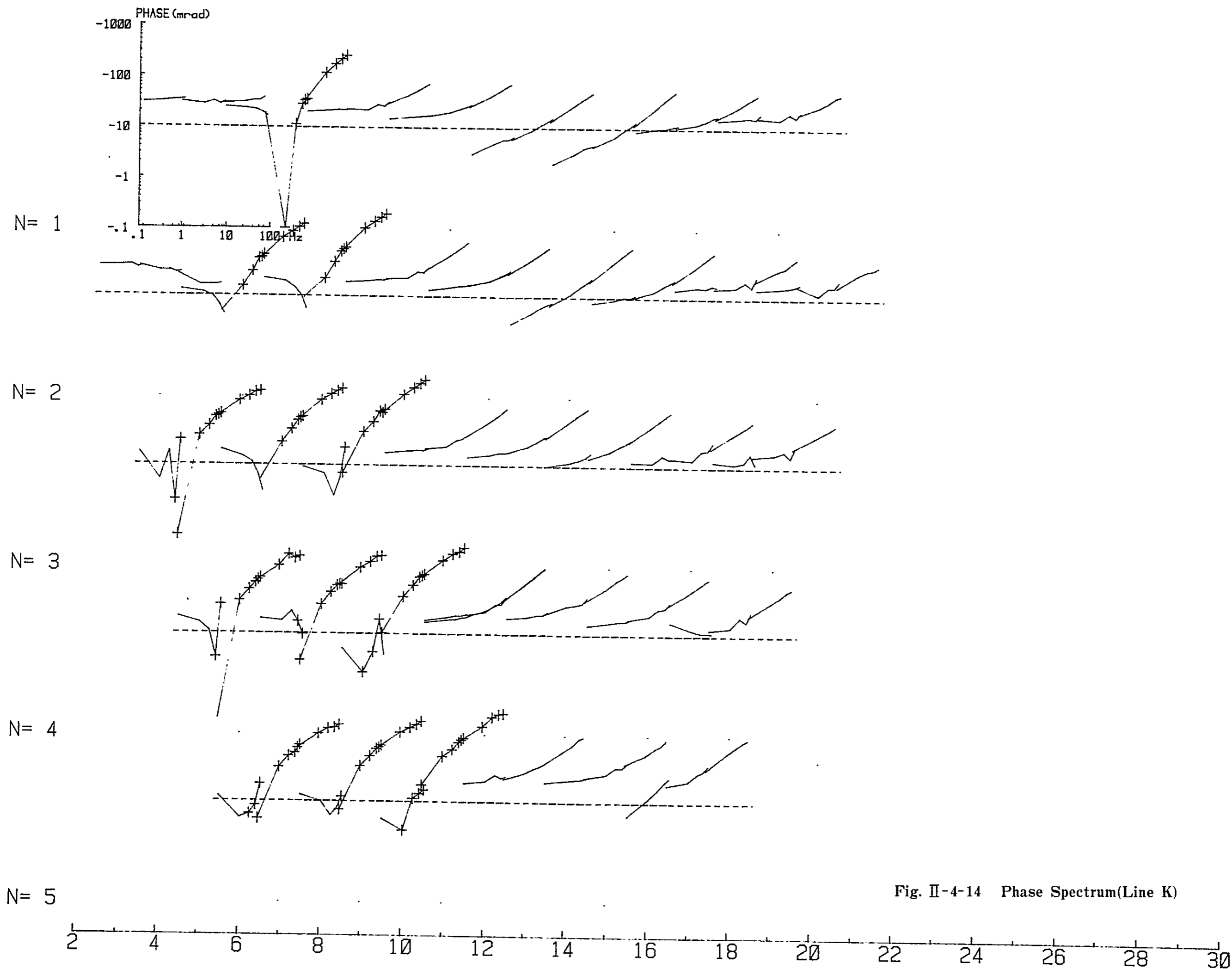


Fig. II-4-13 Phase Spectrum(Line G)



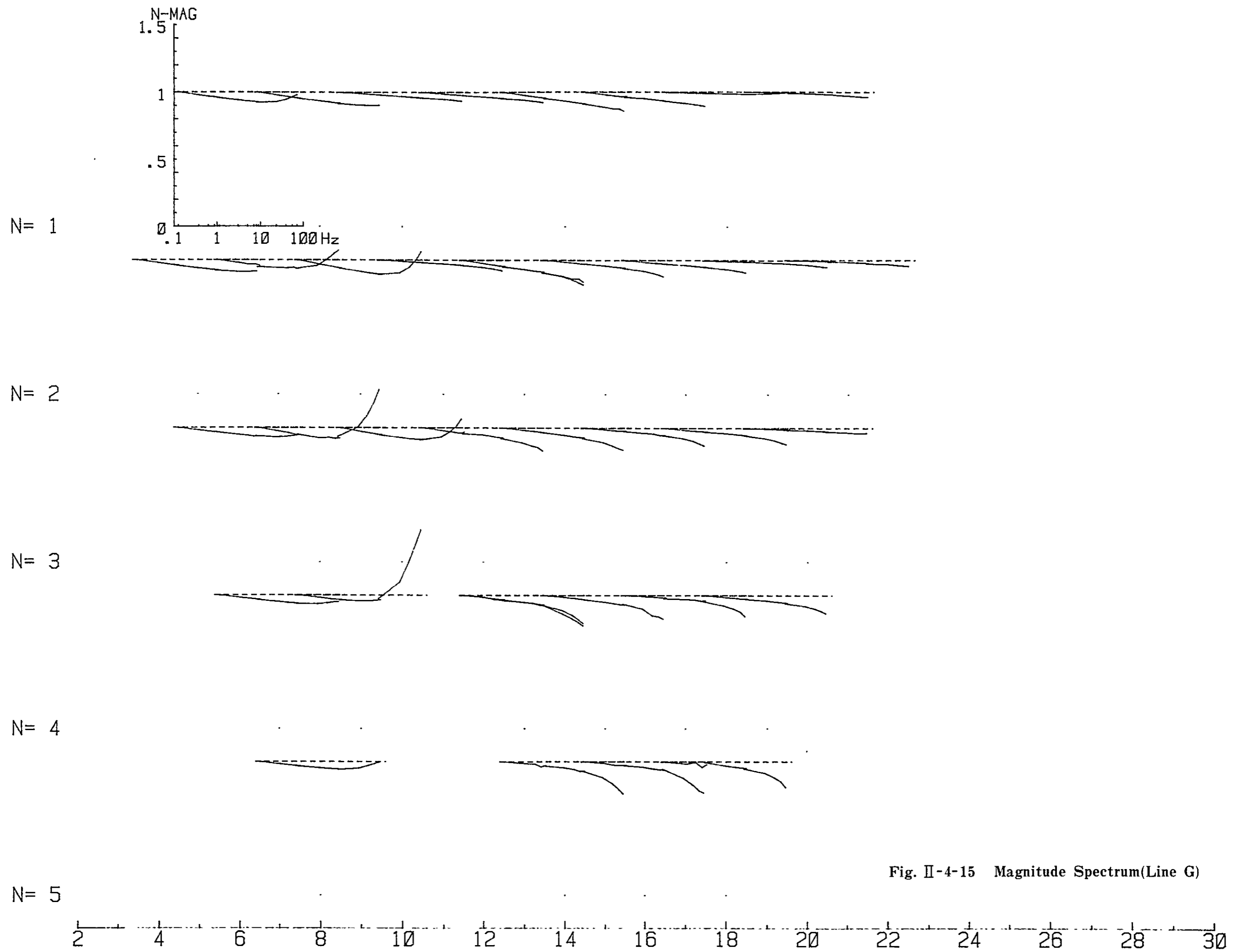


Fig. II-4-15 Magnitude Spectrum(Line G)

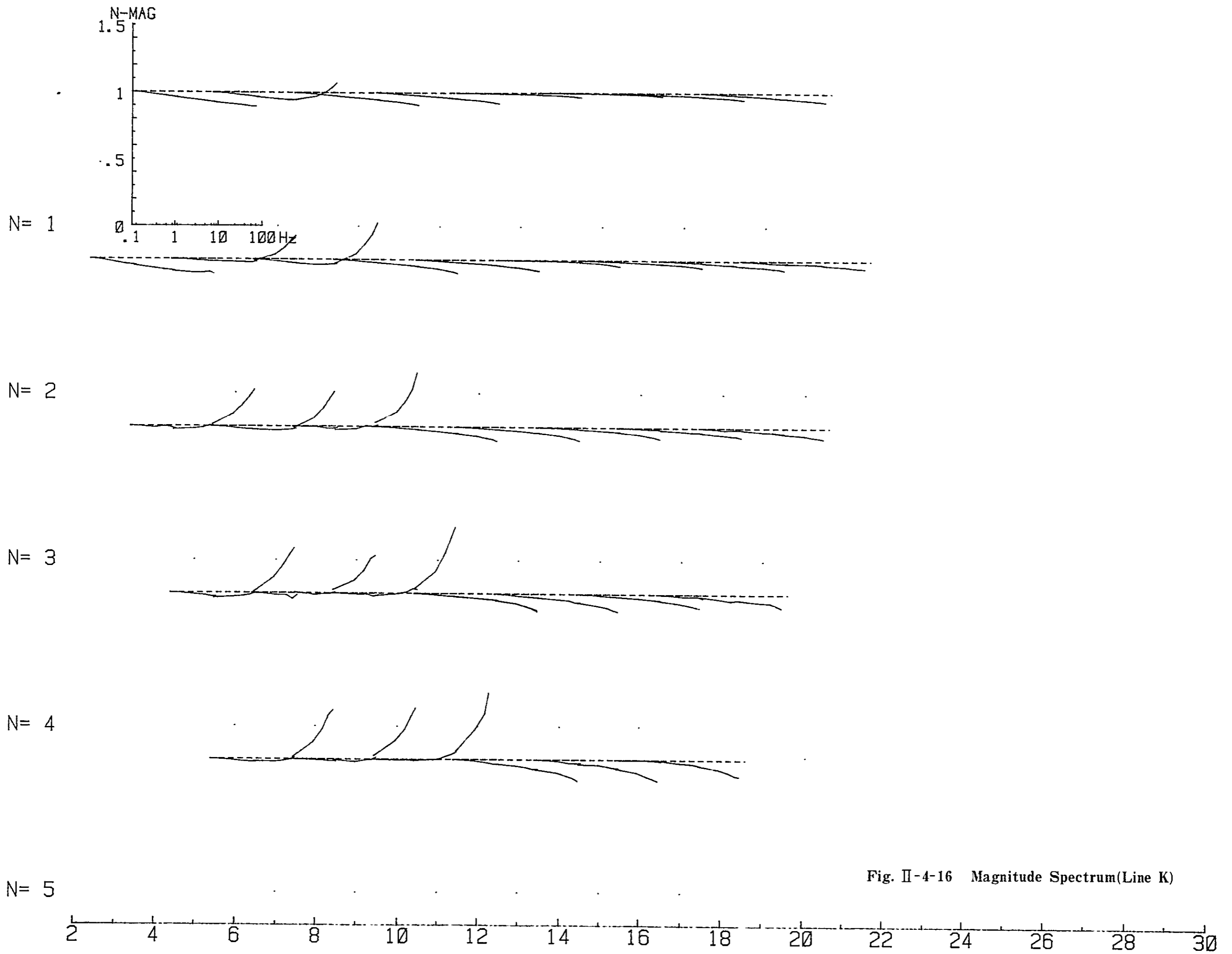


Fig. II-4-16 Magnitude Spectrum(Line K)



## CHAPTER 5 AEROMAGNETIC INTERPRETATION

Aeromagnetic survey analysis was performed for an area of approximately 10,000 km<sup>2</sup> in the Anta Gorda area of Brazil. Analysis work for A-area (southwestern area, 6,750 km<sup>2</sup>) was already done in Phase I. This chapter describes the results of the qualitative and quantitative interpretations for the residual map of the northeastern area (B-area, 3,250 km<sup>2</sup>).

### 5-1 Outline of Aeromagnetic Survey

#### 5-1-1 Survey Area

The analysis work described in this chapter was made from the aeromagnetic data in the area of 10,000 km<sup>2</sup> is located near the boundary between the states of São Paulo and Paraná, Brazil, and forms a polygon whose apexes are as listed below.

	Latitude S	Longitude W
A	24°27'	48°55.6'
B	24°27'	49°15'
C	24°30'	49°15'
D	24°30'	49°30'
E	24°45'	49°30'
F	24°45'	49°45'
G	25°05'	49°45'
H	25°05'	48°52.5'
I	24°52'	48°38.7'
J	24°48.7'	48°40.5'
K	24°45'	48°37.5'
L	24°45'	48°15'
M	24°15'	48°15'
N	24°15'	48°45'

In Phase II, the analysis work was conducted for B-area (A-J-K-L-M-N-A).



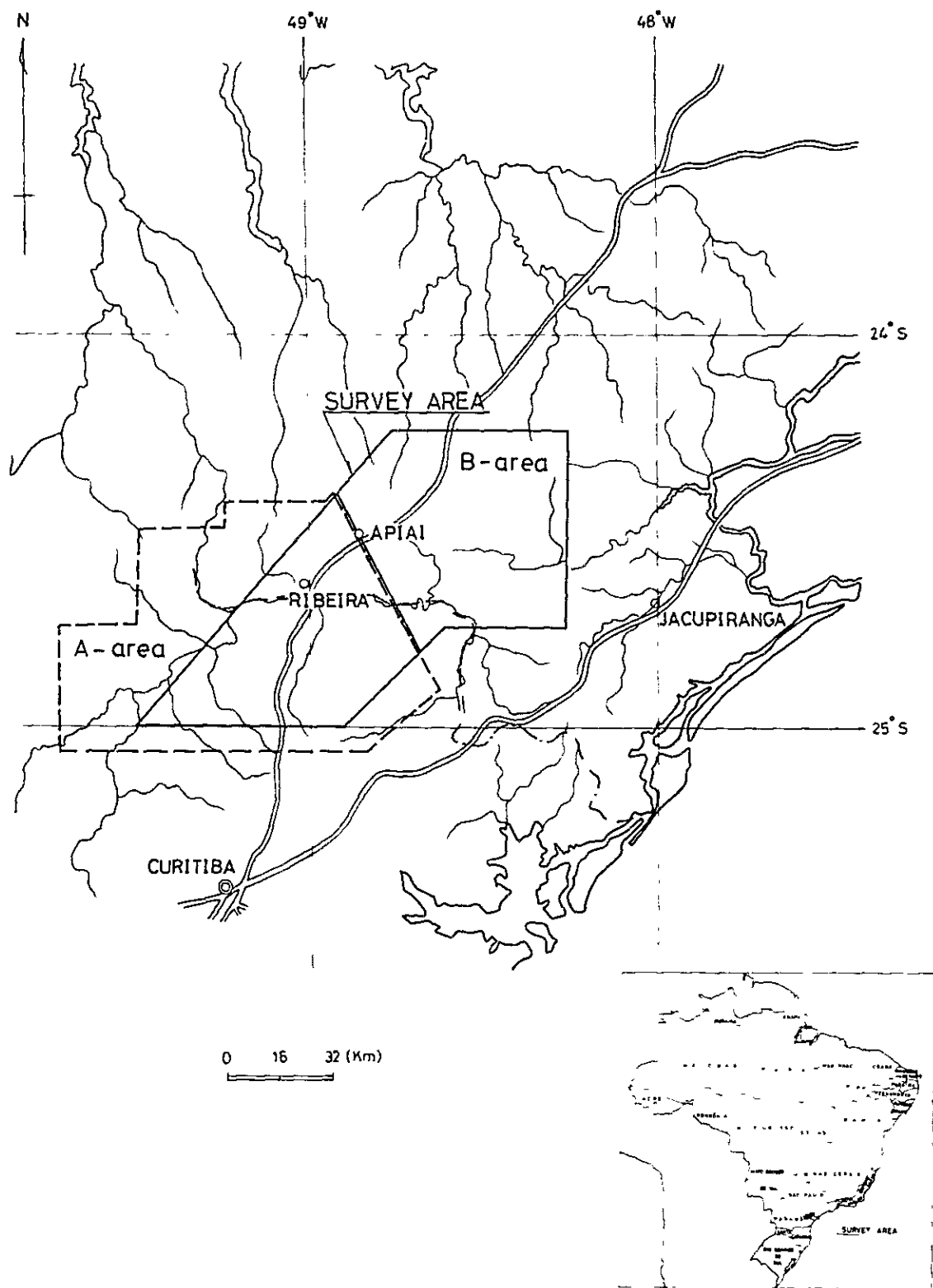


Fig. II-5-1 Location of Aeromagnetic Survey Area





### 5-1-2 Outline of Field Work

The airborne magnetic surveys covering this survey area were conducted by the D.N.P.M. (Departamento Nacional da Produção Mineral) of Ministério das Minas e Energia and CPRM (Companhia de Pesquisa de Recursos Minerais) as a part of the project of the integrated airborne geophysical survey, which also includes aeromagnetic and radiometric surveys. The project names, specifications for both A- and B-areas are as follows.

#### 1) A-area

Project Name : Serra do Mar Sul Project (Data Acquisition) – Airborne magnetic and radiometric survey at the Serra do Mar area, Santa Catarina and Parana.

Survey Period . August, 1975

Total Line Length : about 80,000 km

Flight Elevation 105 ~ 165 m Above Ground Level (A.G.L.)

Separation of Flight Lines . 1 km for the traverse lines and 20 km for the tie lines.

Flight Directions : N30°W and N60°E

Geomagnetic Dip-Angle . 26°S

Geomagnetic declination : N14°W

Total Geomagnetic Intensity . 23,500 gammas

#### 2) B-area

Project Name Airborne geophysical survey at the São Paulo – Rio de Janeiro Area  
(airborne magnetic and radiometric surveys)

Survey Period . June to December, 1975

Total line length about 32,000 km

Flight Elevation 150 m A.G.L.

Separation of Flight Lines 1 km for the traverse lines and 20 km for the tie lines.

Flight Directions . NS and EW

Geomagnetic Dip-Angle : 26°S

Geomagnetic Declination . N14°W

Total Geomagnetic Intensity 23,500 gammas

### 5-2 Method of Analysis

The residual map has been drawn on the basis of the geomagnetic regional variation, which was calculated by subtracting the standard total intensity of the International Geo-



magnetic Reference Field (IGRF) from the aeromagnetic data. The analysis was made to the residual map.

There are two methods of analyzing aeromagnetic data. The first is a qualitative speculation of geological features selectively extracted from geomagnetic residual anomalies by means of some filtering procedures. The filters generally used are given as follows.

- (1) Band-pass filter : which selectively extracts the magnetic anomalies with the optional region of wave length.
- (2) Second vertical derivative filter : which emphasizes the short-wave length magnetic anomaly.
- (3) Upward or downward continuation filter : which attenuates or emphasizes the short wavelength magnetic anomalies by means of calculating the magnetic value on the upper or lower level mathematically.
- (4) Auto-correlation analysis : which delineates the geomagnetic characteristics by detecting similar magnetic anomalies.
- (5) Spectrum analysis This method is to understand the wave length characteristics of the geomagnetic anomalies in the survey area.
- (6) Reduction-to pole filter : which is used to infer the shapes of the magnetized body by means of calculating the magnetic anomaly at the magnetic pole mathematically

The second analysis aims for estimating depths, shapes and magnetic properties of magnetized bodies. The corresponding methods are as follows .

- (1) Specific Point Method
- (2) Curve Matching Method
- (3) Specific curve Method
- (4) Analytical Method

This survey was conducted at the flight level of 150 m A.G.L. in order to effectively detect the magnetic anomalies near the surface, it is suggested that the deep magnetic structure is masked by the shallow one.

In the present anomalies, the energy spectrum analysis by two-dimensional Fourier series was applied to the magnetic data obtained over 56 km x 32 km of the survey area including Rocha and Perau Mines. From the wavelength characteristics, two kinds of band-pass filter maps are obtained from the residual map. Thus three sheets of maps including the residual maps were obtained finally as the bases of qualitative analysis.



Quantitative curve matching analysis, based on the residual map, were also made to the typical anomalies on the residual map.

The methods used in this analytical work are summarized in the following subsection. The flow chart of analyses is shown in Fig. II-5-2.

### 5-2-1 Spectrum Analysis

The wavelength characteristics of magnetic anomalies distributed over the survey area is usefully applied to a magnetic analysis through filtering as well as to an estimate of depth to magnetic basement by using the potential theory.

#### 1) Energy Spectrum

A value  $F(x, y)$  in the rectangular coordinates is expressed in two-dimensional Fourier series as

$$F(x, y) = \sum_{m=0}^{\infty} \sum_{n=0}^{\infty} A_{mn} \exp(-2\pi j (mx/L_1 + ny/L_2))$$

Hence, the Fourier coefficient  $A_{mn}$  is given by

$$A_{mn} = \frac{4}{L_1 L_2} \int_0^{L_1} \int_0^{L_2} F(x, y) \exp(2\pi j (mx/L_1 + ny/L_2)) dx dy$$

The energy spectrum is then obtained as

$$E_{mn} = |A_{mn}|^2$$

#### 2) Estimation of Mean Depth to Magnetic Basement

Assuming that at energy spectrum of magnetic anomalies due to a magnetic layer lying at a depth of  $H$  is white, the potential theory leads the following relation between energy spectrum  $E_{mn}$  of wave numbers  $(m, n)$  and  $H$ . It is

$$E_{mn} \propto \exp(-4\pi H f),$$

Where  $f$  is a quantity called frequency :

$$f = \left(\frac{m}{L_1}\right)^2 + \left(\frac{n}{L_2}\right)^2$$

The energy spectrum is plotted in an  $f$  vs.  $E_{mn}$  graph. A straight line is determined by the least square fitting to the plots.  $H$  is estimated from the tangent of the straight line.



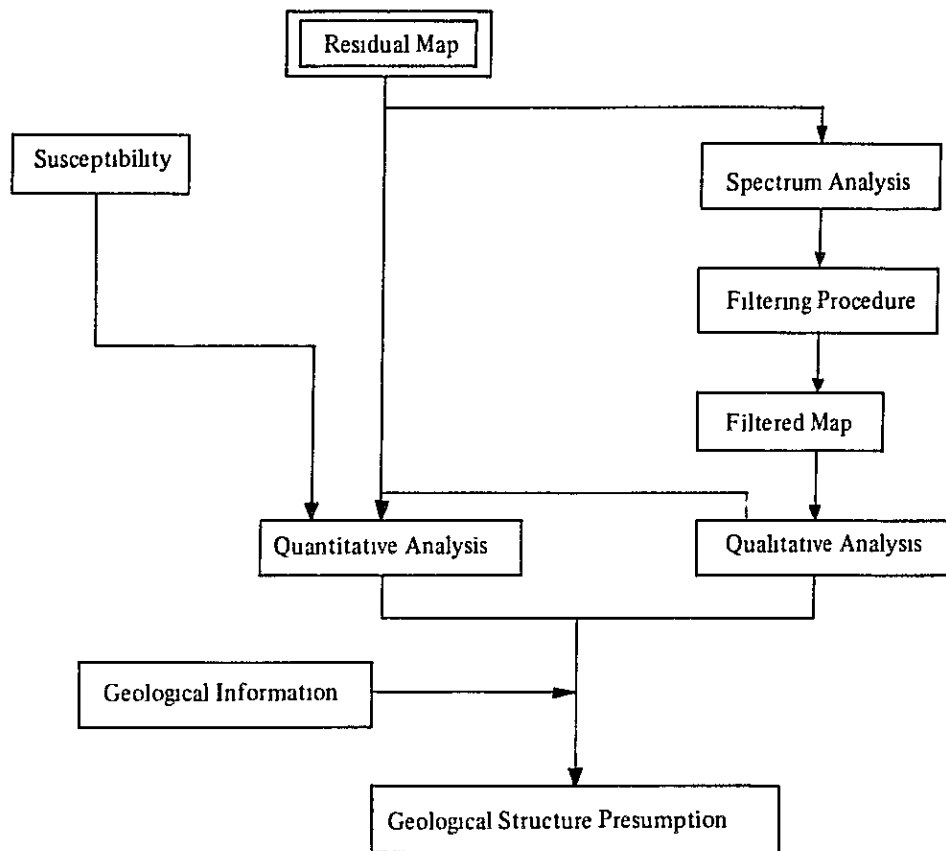


Fig. II-5-2 Flow Chart of Aeromagnetic Analysis





### 5-2-2 Band-pass Filter

The band-pass filter is derived from the deviation of two low pass filters whose cut-off frequencies are different from each other.

Assuming two cut off frequencies as  $\omega_1, \omega_2$  ( $\omega_1 > \omega_2$ ), the coefficients of the band-pass filter is expressed as follows :

$$f_{00} = (\omega_1^2 - \omega_2^2) / \pi^2$$

$$f_{n0} = f_{0n} = (\omega_1 \cdot \sin n\omega_1 s - \omega_2 \sin n\omega_2 s) / (n\pi^2 s)$$

$$f_{mn} = (\sin m\omega_1 s \sin n\omega_1 s - \sin m\omega_2 s \sin n\omega_2 s) / (m \cdot n\pi^2 \cdot s^2)$$

For actual computations, the band-pass filtered values are obtained by the convolution using the discrete magnetic data digitized at 1 km grid and the coefficients given by  $f_{mn}$ .

### 5-2-3 Susceptibility Measurements of Rock Samples

A total of 56 rock samples were collected from outcrops at the location as shown in PL.II-21. Magnetic susceptibility of all the samples were measured by means of a Bison Susceptibility Meter. The results are given in Table II-5-1.

The mean values of magnetic susceptibility amount to

2854 x 10 <sup>-6</sup>	cg s emu/cc	for	1 gabbro sample
1560	"	for	2 diabase samples
1400	"	for	2 syenite samples
467	"	for	6 granite samples
122	"	for	4 amphibolite samples
82	"	for	2 gneiss samples
52	"	for	16 pelitic rocks samples
51	"	for	6 psammitic rocks samples
48	"	for	10 limestone samples

Taking into account the susceptibility values, the rock samples were classified into four classes, class A (strongly magnetic rocks), class B (intermediately magnetic rocks), class C (weakly magnetic rocks) and class D (slightly magnetic rocks). Gabbro, diabase and syenite belong to class A, granite to class B, amphibolite and gneiss to class C, pelitic rocks, psammitic rocks and limestone to class D.

According to the results of magnetic susceptibility measurements, it is expected that in the area where class A magnetic bodies are distributed, magnetic anomalies with a short wave-length and large amplitude are dominant, in the areas where the other classes magnetic



Table II-5-1 Susceptibility of Rock Samples (1)

	Sample No.	Rock Name	Density (gr/cm <sup>3</sup> )		Susceptibility (x10 <sup>-6</sup> cgsemu)	
				Average		Average
Gneiss	F-66	Gneiss	2.61	2.76	65	82
	F-105	Gneiss	2.84		98	
	F-290	Gneiss	2.84		(503)	
Pelitic Rocks	F-2	Phyllite	2.62	2.55 (16)	42	52
	F-5	Mica-schist	(2.83)		(1,877)	
	F-28	Phyllite	2.60		74	
	F-76	Phyllite	2.45		28	
	F-293	Mica-schist	2.52		69	
	F-294	Phyllite	2.57		38	
	F-300	Sericite-schist	2.64		73	
	S-13	Sericite-schist	2.38		54	
	S-20	Sericite-schist	2.55		70	
	S-24	Calcareous-schist	2.73		62	
	T-10	Mica-schist	2.69		50	
	T-13	Mica-schist	2.67		51	
	T-16	Mica-schist	2.65		38	
	T-20	Sericite-schist	2.55		27	
	T-35	Phyllite	2.50		56	
	T-47	Phyllite	2.05		32	
K-252	Sericite-schist	2.59	73			
Psammitic Rocks	F-1	Quartzite	2.64	2.63 (6)	61	51
	F-67	Quartzite	2.62		38	
	T-9	Psammitic-schist (metasandstone)	2.73		71	
	K-195	Psammitic-schist (metasandstone)	2.62		59	
	K-258	Psammitic-schist (metasandstone)	2.53		30	
	K-263	Psammitic-schist (metasandstone)	2.62		49	
Green-schist	T-30	Green-schist	2.92	2.87 (2)	88	85
	K-340	Green-schist	2.81		81	



Table II-5-1 Susceptibility of Rock Samples (2)

	Sample No.	Rock Name	Density (gr/cm <sup>3</sup> )		Susceptibility (x10 <sup>-6</sup> cgsemu)	
				Average		Average
Limestone	F-72	Limestone	2.78	2.77 (10)	24	48
	S-15	Limestone	2.72		30	
	S-86	Limestone	2.77		47	
	S-89	Limestone	2.75		59	
	S-94	Limestone	2.73		61	
	S-128	Limestone	2.71		36	
	S-129	Limestone	2.75		43	
	T-58	Limestone	2.66		46	
	T-85	Limestone	2.72		54	
Amphibolite	F-7	Amphibolite	2.97	2.95	108	122
	F-272	Amphibole -schist	2.92		109	
	S-93	Amphibolite	2.99		117	
	K-176	Amphibole -schist	2.83		(4,115)	
	K-178	Amphibolite	2.99		(1,390)	
	K-182	Amphibolite	3.00		155	
Granite	F-39	Granite	2.61	2.64	225	467
	F-57	Granite	2.62		593	
	F-242	Granite	2.62		154	
	S-49	Granite	2.68		890	
	S-91	Granite	2.64		80	
	K-184	Granite	2.64		860	
Syenite	F-21	Syenite	2.59	2.62	1,272	1,400
	F-87	Syenite	2.65		1,528	
Gabbro	S-33	Gabbro	2.93		2,854	2,854
Diabase	S-17	Diabase	3.02	2.96	2,331	1,560
	S-95	Diabase	2.90		796	
	F-4	Magnetite	3.67		54,970	



bodies are distributed, there are many magnetic anomalies of small amplitude.

### 5-3 Results of Analysis

The flight elevation in the B-area is 150 m above terrain similarly as one in the A-area. Although this flight method is effective one to detect buried small size causative body at shallow depth, it is difficult to recognize characteristics of magnetic pattern so that the shape of causative bodies are partly understood.

In the residual map, the short wavelength magnetic anomalies reflecting shallower magnetic structure are dominant and the long wavelength ones caused by deep or large magnetic structure are masked by those.

#### 5-3-1 Residual map

Judging from the magnetic anomalies shown in the residual map (PL II-14), the magnetic feature of the B-area are summarized as follows:

- 1) The relief of the residual map of B-area is smaller than one of A-area.
- 2) The northeastern part of B-area is occupied by the groups of magnetic anomalies with the amplitude in excess of 100 gammas and half wavelength of 1 to 3 km, of which the direction is almost N60°W. This part is called as Zone F. In this zone, it is presumed that magnetic rocks of class A such as gabbro, diabase and syenite, are extensively distributed.
- 3) In the southern part of B-area, the groups of magnetic anomalies with the half wavelength of 1 to 3 km and the maximum amplitude of less than 300 gammas are distributed at the trend of N60°E. This area is called as Zone G, where magnetic bodies of rank B and C (amphibolite, granite or gneiss) may be distributed.
- 4) In the northwestern corner of B-area, relatively long wavelength magnetic low with the northeast trend. The magnetic feature in this corner are similar with one of Zone B of A-area and this corner is located on the extension of Zone B so that this corner is called as Zone B.
- 5) In the central part of B-area, except for the area where the narrow belt of the magnetic anomalies, trending N75°E, with half wavelength of 1.5 to 4 km and large amplitude, caused by rank A magnetic bodies, are distributed, the relief is very small so that magnetic bodies of rank C or D may be dominated. This area may correspond to the extension of Zone C of A-area so it is called as Zone C.

The triangular area with its apexes at Santo da Serra, at 10 km west of Adrianópolis and





at Barra do Batatal in the central-eastern part of this zone is called especially as Zone E where magnetic anomalies of small relief appear.

As mentioned above, from the point of the magnetic feature B-area is divided into five zones, Zones B, C, E, F and G.

It can be seen that there are the continuities in the arrangement of the magnetic anomalies detected in the residual map within each zone. In zone B, the trend of N60°E is dominant. In Zone C, N60°E-trending and eastward-trending magnetic contours are dominant at the central-northern and at the southern parts respectively. In Zone E, the trends of east and N30°E are dominant. In Zones F and G, the N60°W and N60°E-trending magnetic contours are dominated respectively.

Features such as faults may be manifested magnetically by dislocations or dispersions in magnetic pattern or by persistent changes in pattern over long distances. These features are called as magnetic discontinuity or geotectonic line in this analysis.

Taking the above circumstances and the susceptibility measurement results of rock samples into consideration, a qualitative interpretation is made to the residual map as follows

1) Zone B : The northeast-trending magnetic discontinuity is indicated near the boundary with Zone C, and in Zone B, at the north of this geotectonic line, rank B magnetic bodies (granite) are distributed.

2) Zone C : The direction of major geotectonic lines is northeast, which disappear near the boundary with Zone F. A geotectonic line extending to northeast from Apiai corresponds to Espirito Santo Fault and there is another parallel one at its south side. Rank A magnetic bodies, causing the narrow belt of strong magnetic anomalies, are located between these two geotectonic lines. The northeast-trending geotectonic line, along the boundary with Zone E, may coincide with Figueira Fault and extends from 6 km west of Sitfo da Serra towards Bombas and at Bombas changes its strike to westwards.

In the northern area of Espirito Santo Fault, it is estimated that rank B magnetic bodies (granite) are indicated broadly at the north of Apiai by the pattern of the group of the relatively short wavelength magnetic anomalies.

In other area of Zone C, as relief are very small, rank D magnetic bodies are dominant.

The north-striking geotectonic line from 10 km east of Apiai to 5 km east of Colônia Marque de Adrantes is assumed, which indicates the boundary between rank B of the west



side and rank D magnetic bodies of the east side.

3) Zone E . In the northwestern part, the direction of major geotectonic lines is northeast and rank C magnetic bodies are distributed parallel on this direction. On the other hand, in the southern and eastern parts, major geotectonic lines with the eastward-trend are dominant, and among them, one from Barra do Batatal to 10 km south of Bombas may coincide with Ribeira Linearment.

There are plenty of magnetic anomalies of small relief caused by rank C magnetic bodies.

In the northeastern part, there are the group of magnetic anomalies caused at the margin of large scale magnetic body. This body may correspond to rank B magnetic bodies (granite).

4) Zone F · The group of N60°W-trending strong magnetic anomalies with short wavelength are dominant. These anomalies are caused by dykes of rank A magnetic body (diabase).

5) Zone G : Geotectonic line with the strike of N75°E from Barra do Batatal at the east edge to east of Tunas at the central-south edge, is located on the boundary between Zones C and E, and Zone G, which corresponds to Itapeuna Linearment. Also there is another one with same strike at its south side. Between these two geotectonic lines, there are relatively strong magnetic anomalies with similar trend, which may correspond to rank C magnetic bodies

The remarkable magnetic anomalies are classified with these zone signatures.

### 5-3-2 Band Pass Maps

Fig. II-5-4 shows an energy spectrum analysis result of magnetic anomalies based on the residual map of an area 56 km of N14°W-S14°E by 32 km of N76°E-S76°W including Zones B and C of A-area (Fig. II-5-3) Judging from the energy spectrum distribution, the energy spectrum has a tendency to decrease with wavelength.

The wavelength domain is divided into three sub-domains whose boundary wavelengths are 2 km, 4 km and 16 km. Straight lines are fitted by the least square method in each of the subdomains, i.e. 2-4 km, 4-16 km and larger than 16 km. From the gradients of the straight lines, the depths to the magnetic basement are estimated as -2 km, -6 km and -20 km from the flight level respectively. But as this survey flight method is not conducted



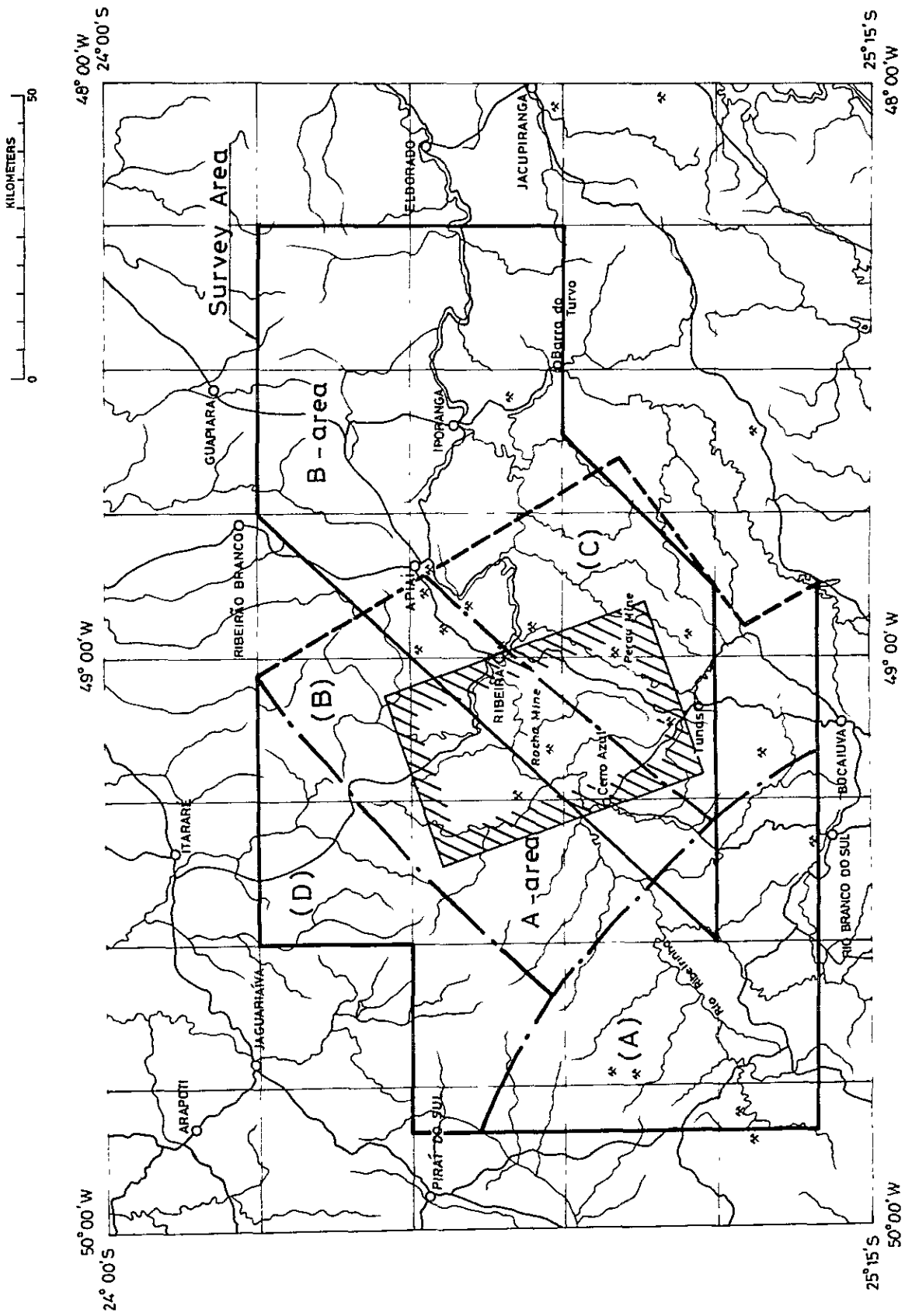


Fig. II-5-3 Index of Analyzed Area



by exactly horizontal flight, these values will be apparent depth for mathematical procedures.

In order to distinguish the distribution of the magnetic bodies from these sizes, the following band- and low-pass filters were designed.

- 1) BP-1 : Band-pass filter for a wavelength domain of 4 to 16 km
- 2) BP-2 : Low-pass filter for a wavelength domain in excess of 16 km

These two filters were applied to the residual map to obtain band-pass map BP-1 and low-pass map BP-2.

(1) Band-Pass Map (BP-1)

On band-pass map (BP-1), magnetic anomalies with the wavelength less than 2 km are eliminated. But the continuities of the arrangement of magnetic anomalies in each zones which can be seen on the residual map, are remained and similar geotectonic lines are indicated on similar location.

(2) Band-Pass Map (BP-2)

This map is characterized by magnetic anomalies with a half-wavelength larger than 10 km. It is considered that this map does not reflect the deep magnetic structure and expresses only the apparent magnetic anomalies as calculated mathematically.

### 5-3-3 Quantitative Analysis

Some profiles are drawn for typical magnetic anomalies on the residual map. Depths to the magnetic source and its apparent susceptibility were estimated from the data by means of the curve matching method using standard curves of the prism, dyke and other models. In proportion to the obtained susceptibilities, the magnetic intensity of the source is classified into four classes A, B, C and D, as stated in 5-2-3.

#### Zone C

The group C-6 of magnetic anomalies near 2 km south of Apiaí is caused by the magnetized rocks with the apparent susceptibility ( $\Delta K$ ) of  $3.4 \times 10^{-6}$  cgsemu, dipping at  $60^\circ$ N. C-7 and C-8 magnetic anomalies northeast of C-6 are induced by magnetized bodies with  $\Delta K = 2.1 \times 10^{-6}$  cgsemu dipping to north at  $60^\circ$ , similarly as C-6. Three magnetized bodies, C-6, 7 and 8 are exposed. Magnetized bodies, C-9, 10 and 12 are near surface and those susceptibility are 1.5, 1.5 and  $7.7 \times 10^{-6}$  cgsemu respectively. Judging from these results, the results of susceptibility measurement of rock samples and geological informations, C-6 corresponds to gabbro and C-7, 8, 9, 10 and 12 to gabbro and amphibolite.





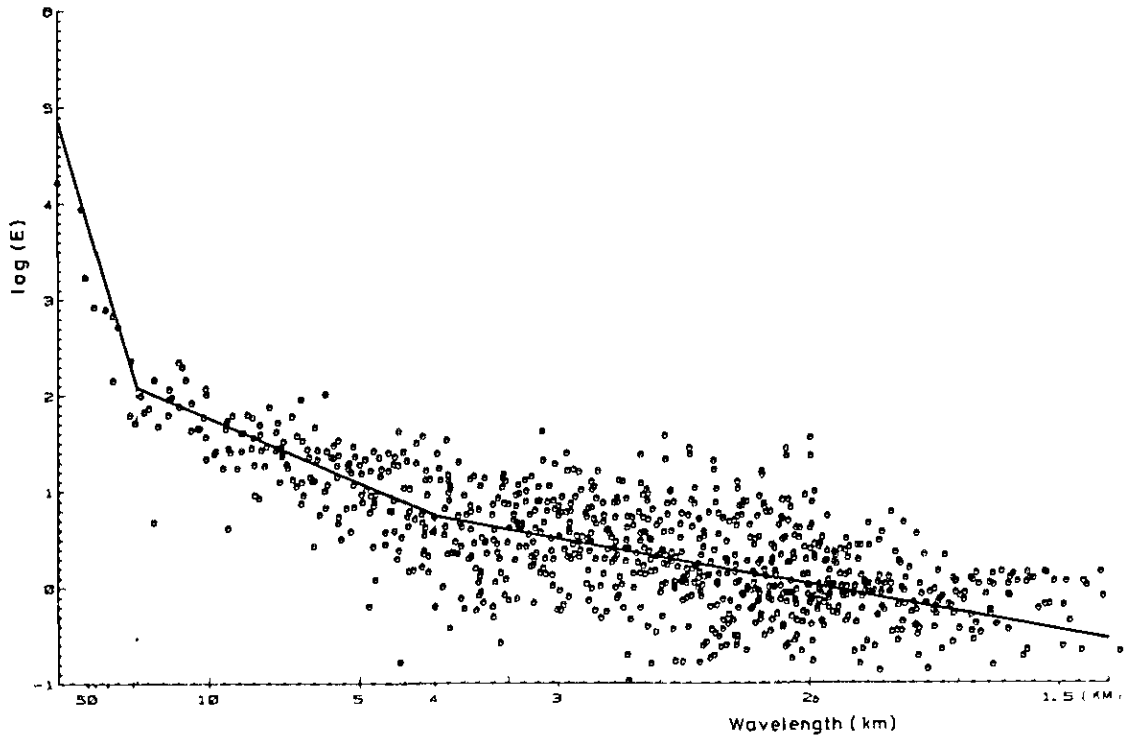


Fig. II-5-4 Frequency Response of Band-pass and Low-pass Filters

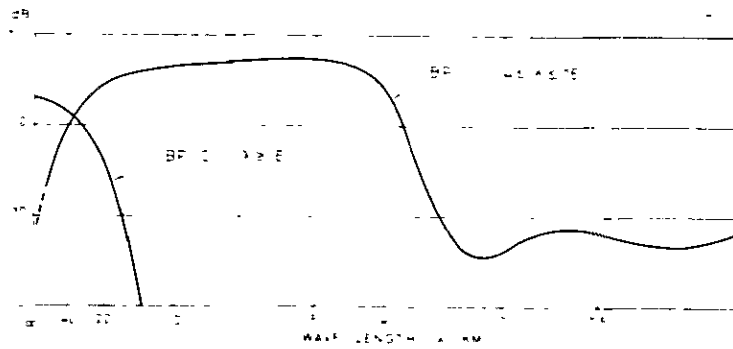


Fig. II-5-5 Energy Spectrum vs. Wavelength



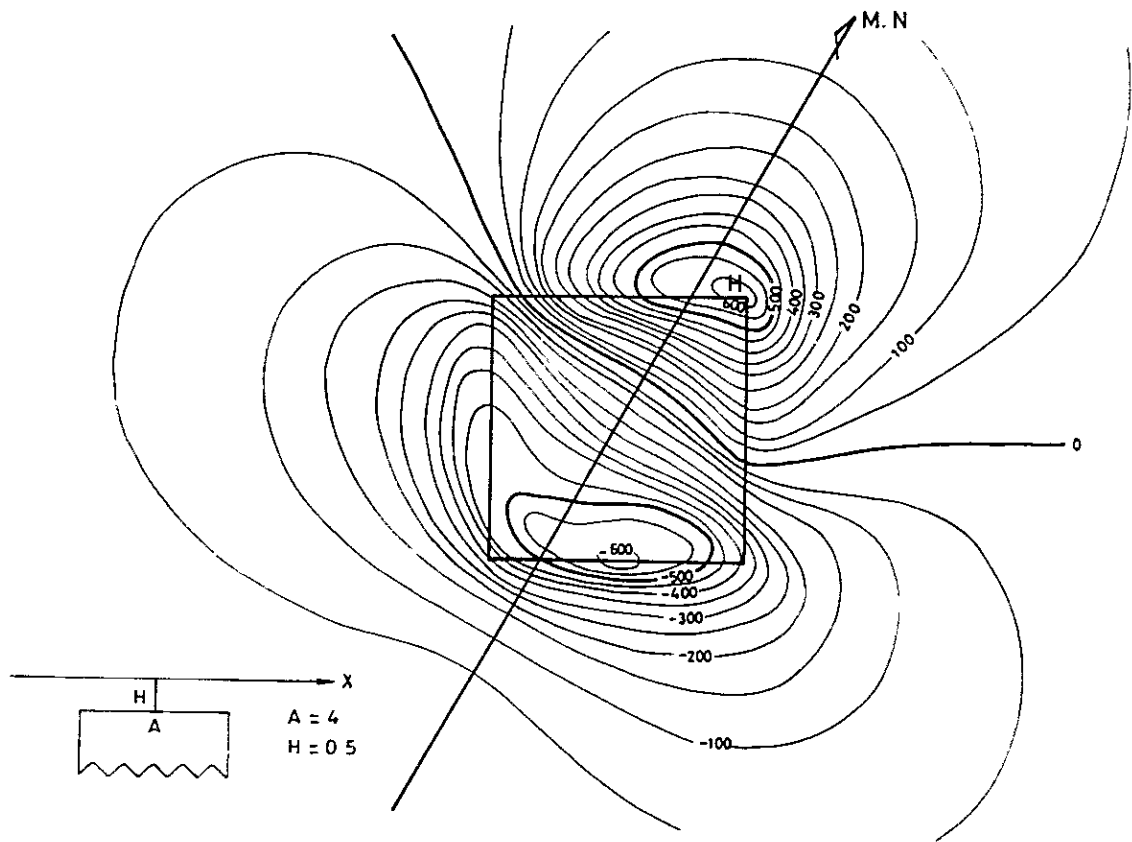


Fig. II-5-6 Magnetic Anomaly due to Prism Model( $26^{\circ}S$ )



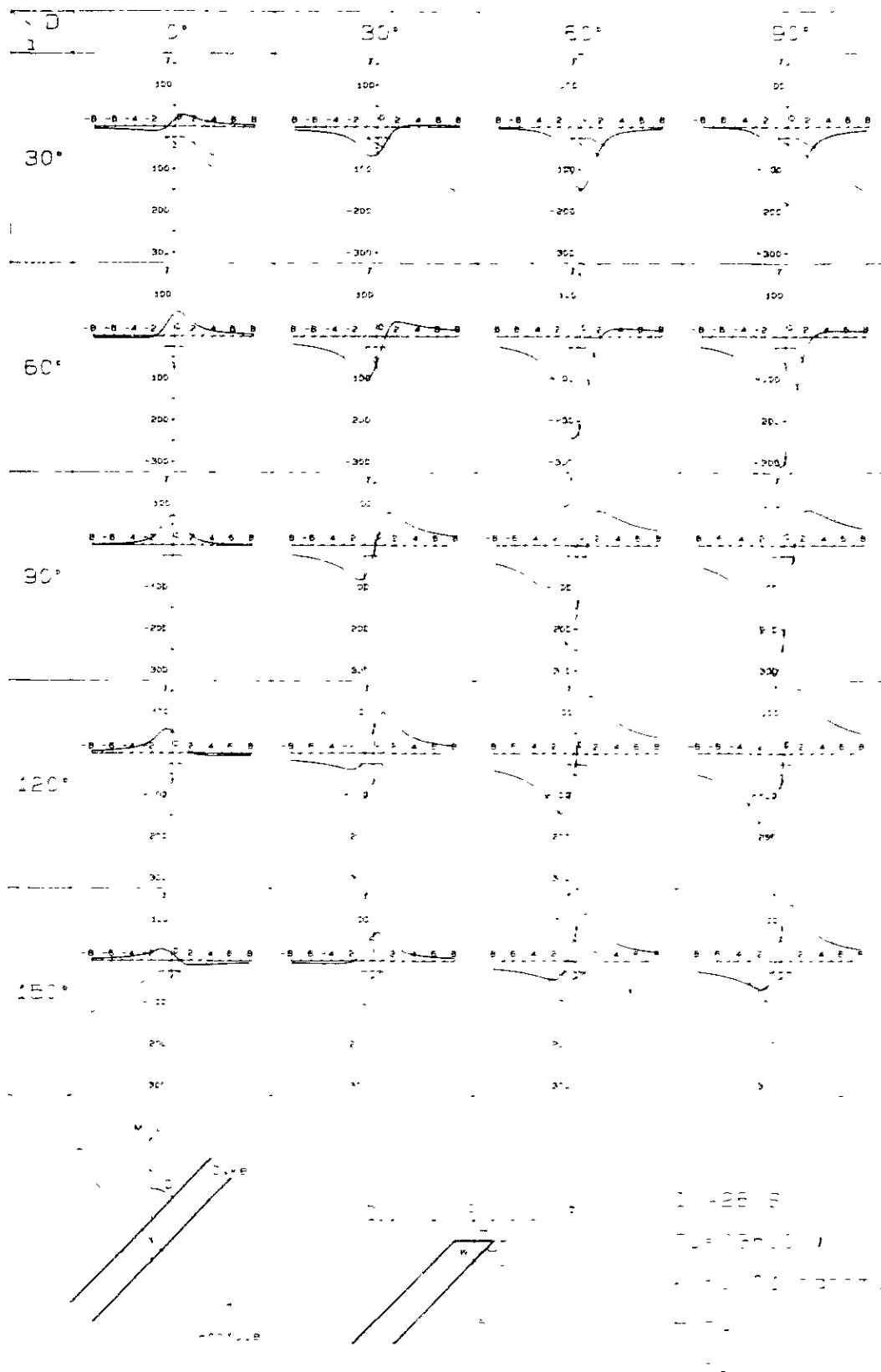


Fig. II-5-7 Magnetic Anomaly due to Dyke Model(26°S)



Magnetic anomaly C-11 is caused by highly magnetized body with  $\Delta K = 3.3 \times 10^{-6}$  cgsemu, exposed. According to the geological map, granite (rank B magnetic body) is distributed at similar location. It is suggested that this granitic rock (C-11) might be different with other granite in the survey area because of its high susceptibility.

From the results of quantitative analysis, Espirito Santo Fault running at the north side of magnetized bodies C-6, 7, 8, 9, 10 and 12, might dip to north at  $60^\circ$ .

PL. II-21 shows the above results synthetically estimated from the quantitative and the qualitative analyses.

#### 5-4 Summary

Magnetic anomalies in the survey area are classified into four classes A, B, C and D, which are induced by the exposed or buried magnetic sources of class A (strongly magnetic), class B (intermediate magnetic), class C (weakly magnetic) and class D (slightly magnetic) respectively.

According to the susceptibility measurement of rock samples, gabbro, diabase and syenite belong to class A, granite to class B, amphibolite and gneiss to class C and pelitic rocks, psammitic rocks and limestone to class D.

And the survey area is divided into seven zones, Zones A to G from the magnetic feature.

The results of the analysis in B-area can be summarized with geological implications as follows.

1) B-area except for the northeastern and northwestern parts are dominated by rank D magnetic bodies and the northeast-trending and east-trending geotectonic lines are dominant at the north and at the south respectively.

At the northern part of Zone C, rank A (gabbro) and C (amphibolite) magnetic bodies are distributed as intrusive rocks, which is controlled by the northeast-trending geotectonic lines. Southern magnetic bodies are exposed but northern ones are concealed.

In the central part (Zone F), rank C (amphibolite) magnetic bodies are distributed as narrow dykes, changing those strikes from northeast to east.

And in the southern part (Zone G), buried rank C magnetic rocks (amphibolite) controlled by two geotectonic lines with the strike of  $N75^\circ E$  are distributed parallel at the same direction.





2) In the northeastern part (Zone E), although granite (rank B) and rank D magnetic rocks are distributed on the geological map, it is impossible to delineate such rocks because of dykes of diabase (rank D magnetic rock).

3) The rank B magnetic rocks (granite) are delineated at the northeastern corner, at the north of Apiaí, at the north of Pedra Santa and at the southeastern corner of B-area from the continuity of magnetic anomalies. But, the one located at 16 km east of Apiaí might be different with other granitic rocks because of its high susceptibility.

Based on above-mentioned considerations, the following conclusions were derived.

The geological lineation runs in a NE–SW direction. This tendency is consistent with the magnetic linearment. Granite, gabbro, diabase and syenite are almost delineated. Mines in the survey area locate within the magnetic body of class D and apparently near the magnetic body of rank A, B and C. The relation between the mines and these rocks is not clear.



## APPENDICES



**Photo A-1 Field Survey**





Location    Ribeirão do Perau  
Setuva Formation  
augen gneiss



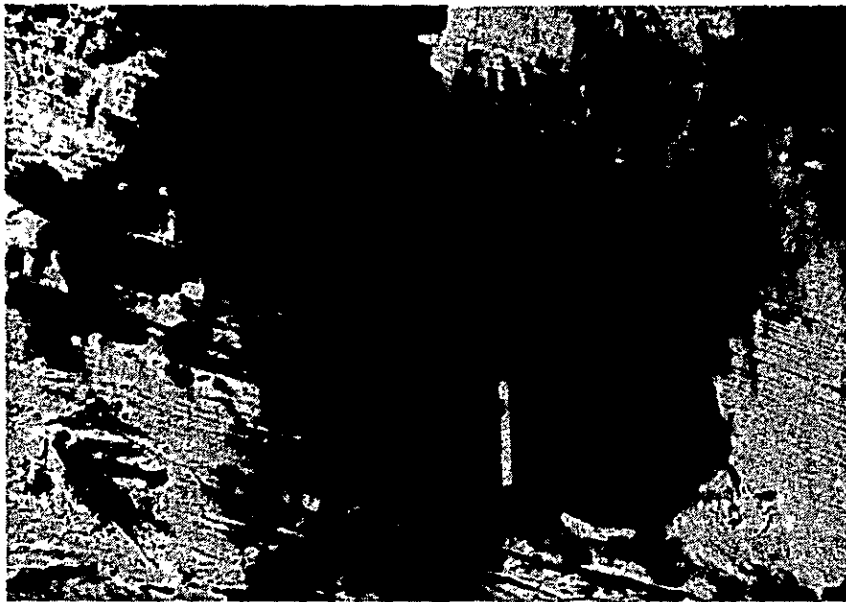
Location    Ribeirão do Perau  
Açungui I Formation  
Quartzite



Location    Ribeirão do Perau  
Açungui I Formation  
Calc-silicate rock



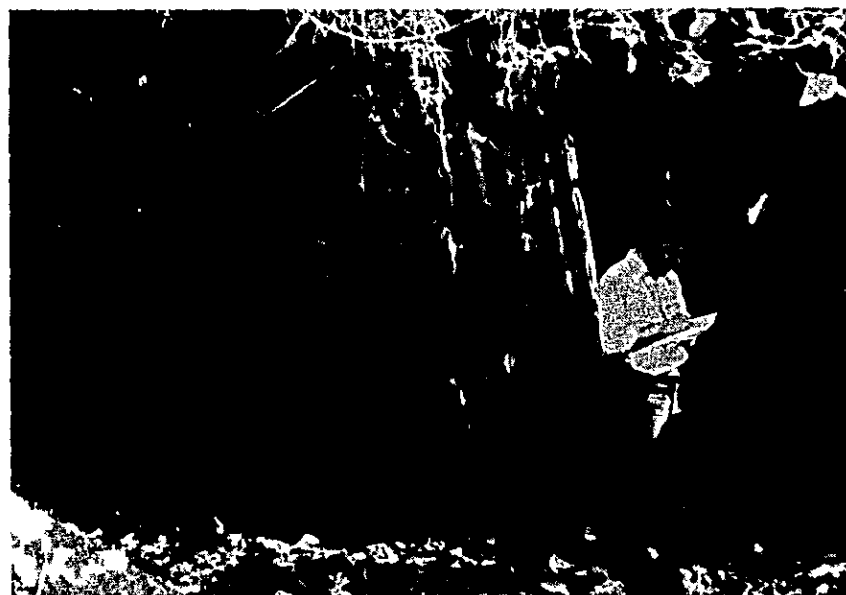




Location · North of Tunas  
Açungui II Formation  
Phyllite and sericite,  
muscovite schist

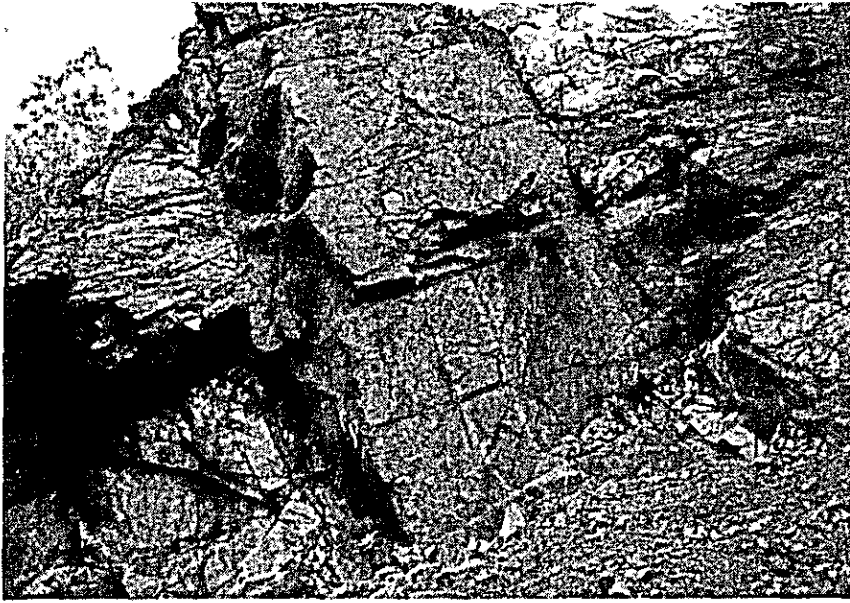


Location · Panelas area  
Açungui III Formation  
banded limestone

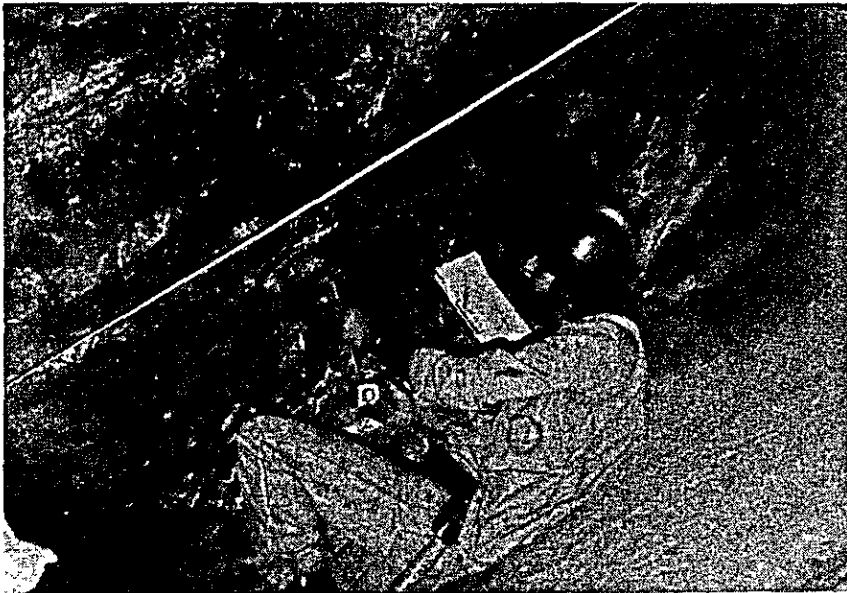


Location · Rio Mato Preto  
Açungui III Formation  
Calc-schist

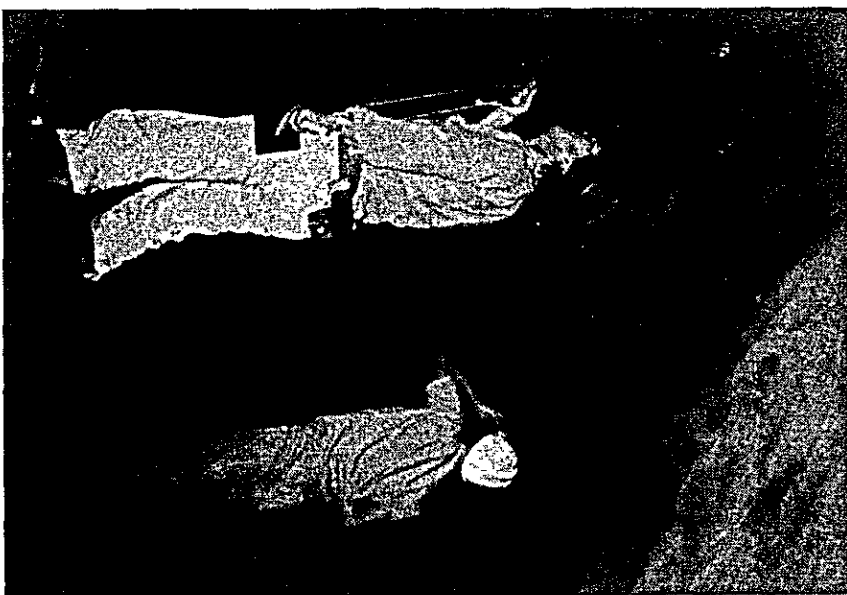




Location Rio Ribeira  
Diabese dyke intruded in  
Metabasite



Location Perau Mine  
Underground sketch  
work in Perau mine



Location Perau Mine  
Underground sketch  
work in Perau Mine

